

1995

Handbook of Conducting Polymers

Second Edition, Revised and Expanded

Edited by

TERJE A. SKOTHEIM
*Moltech Corporation
Tucson, Arizona*

RONALD L. ELSENBAUMER
*The University of Texas at Arlington
Arlington, Texas*

JOHN R. REYNOLDS
*University of Florida
Gainesville, Florida*

DISTRIBUTION STATEMENT A
Approved for Public Release
Distribution Unlimited



MARCEL DEKKER, INC.

NEW YORK • BASEL • HONG KONG

20030225 115

Metal–Insulator Transition in Doped Conducting Polymers

Reghu Menon, C. O. Yoon, D. Moses, and A. J. Heeger

Institute for Polymers and Organic Solids, University of California at Santa Barbara, Santa Barbara, California

I. INTRODUCTION

The initial impetus for the plethora of work on conducting polymers was generated by the discovery in 1977 [1–3] of the increase, by nearly 10 orders of magnitude, in the electrical conductivity (σ) of polyacetylene when it was doped with iodine or other acceptors. The subsequent demonstration of the important role of nonlinear excitations, solitons, polarons, and bipolarons upon chemical doping or photoexcitation in the semiconducting regime provided a conceptual framework for understanding the electronic structure of these novel polymer semiconductors at low doping levels [4–13]. Although there has been impressive progress toward the goal of improving conductivity and achieving truly metallic polymers [14–17], parallel progress toward understanding the transport in the “metallic” state has been limited by the quality of the disordered polymer materials.

The existence of a Pauli spin susceptibility [18], a quasilinear temperature dependence of the thermopower [19], and a linear term in the specific heat [20] provided early evidence of a continuous density of states with a well-defined Fermi energy. However, the real “fingerprints” of metallic behavior were not observed—for example, finite dc conductivity as $T \rightarrow 0$, a positive temperature coefficient of the logarithmic derivative of the conductivity, $W = [\Delta \ln \sigma / \Delta \ln T]$, and metallic (Drude-like) reflectivity in the infrared. In recent years, improved homogeneity and a reduction in the degree of disorder resulting from improved synthesis and processing of conducting polymers have provided a new opportunity for investigating the nature of the “metallic” state through transport and optical measurements [21–32]. The improvement in the quality of the new generation of materials has enabled the observation of these typical metallic features in specific systems [33–35] and has resulted in a deeper understanding of the role of

disorder as the limiting factor in transport and as the origin of the metal–insulator (M–I) transition in doped conducting polymers.

In first-generation conducting polymers, the electrical conductivities were limited; the maximum value observed in iodine-doped Shirakawa polyacetylene, $(CH)_x$, was on the order of 10^3 S/cm [1–3], whereas in doped polypyrrole (PPy) [36,37] and polythiophene (PT) [38–40], the best values were below 200 S/cm. Moreover, $\sigma(T)$ decreased rapidly upon lowering the temperature; i.e., the logarithmic derivative, $W = \Delta \ln \sigma / \Delta \ln T$, had a negative temperature coefficient indicative of transport on the insulating side of the metal–insulator transition. With the exception of doped $(CH)_x$ [41], a finite dc conductivity as $T \rightarrow 0$ was not observed. Although the thermopower was quasilinear with temperature, typical of that expected for metallic systems [19], the temperature dependence of the magnetic susceptibility showed a relatively large Curie contribution, observable even at room temperature and the dominant contribution at low temperatures [18,27–30]. Thus, in early measurements on conducting polymers, the presence of strong disorder masked the metallic behavior; the features observed were typical of those expected for highly disordered and inhomogeneous media.

The high electrical conductivities of doped polyacetylene reported by Naarmann et al. [14–16] in 1987 signaled the onset of a new generation of conducting polymers. Conductivities on the order of 10^4 S/cm, comparable to those of traditional metals like lead, were reported. By continuing to improve the material, Tsukamoto increased the conductivity by another order of magnitude, to 10^5 S/cm, in 1990 [17]. Correspondingly, the temperature dependence of conductivity, $\sigma(T)$, in doped $(CH)_x$ consistently became weaker as the conductivity increased.

Although values of σ on the order of 10^4 S/cm were

observed for doped oriented PPV in 1990, no rigorous transport measurements were carried out [22–24]. In 1991, the low temperature electrochemical polymerization of PF_6 -doped PPy, subsequently stretch oriented, yielded $\sigma \sim 10^3 \text{ S/cm}$ [25,26]. In this material, for the first time in doped conducting polymers, a significant positive temperature coefficient of resistivity (TCR) was observed at temperatures below 20 K.

In 1991, the development of the counterion-induced processibility of polyaniline (PANI) enhanced the conductivity of PANI to 300–400 S/cm [27–30]. These samples showed substantially weaker temperature dependence of $\sigma(T)$ than previous generation PANI [34,35]. Moreover, for the first time, a doped conducting polymer showed a significant positive TCR in the temperature range 160–300 K [34,35].

In 1992, the synthesis of regioregular polyalkylthiophenes (PAT) resulted in materials with substantially enhanced conductivity with values on the order of 10^3 S/cm [31,32].

This brief summary of the significant developments that have occurred within the last few years in the preparation and processing of doped conducting polymers indicates substantial progress; further progress is necessary, however, to reduce the microscopic and macroscopic disorder and thereby bring out the intrinsic metallic features. The systematic improvement in material quality needs to be characterized by rigorous transport measurements in order to quantify the various parameters involved in the disorder-induced localization that leads to the M–I transition. The conclusions inferred from such experimental studies will provide a deeper understanding of the microscopic parameters involved in charge transport in these metallic polymers and consequently a deeper understanding of the requirements for further improvement in the quality of the materials.

The objective of this review is to summarize the results of recent transport measurements near the M–I transition in the doped conducting polymers, $(\text{CH})_x$, PANI, PPy, and PAT, including dc conductivity, thermoelectric power, and magnetoresistance, all as a function of temperature, pressure, and magnetic field. The results are compared with theoretical models of the M–I transition [42–45] in order to understand the microscopic transport mechanisms, especially as a function of disorder and as a function of the strength of the interchain transfer interaction.

A comparison of the conductivities of doped conducting polymers with those of conventional conductors is shown in Fig. 2.1. Although conductivities on the order of 10^5 S/cm have been observed for stretch-oriented $(\text{CH})_x$ (along the chain direction), the absence of a positive TCR, typical of a metal, indicates that the bottleneck responsible for the “nonmetallic” temperature dependence of $\sigma(T)$ is the transport perpendicular to the chain axis. Typical conductivity values perpendicular to

the chain axis for highly oriented $(\text{CH})_x$ are on the order of 10^2 S/cm , i.e., comparable to or less than Mott’s minimum metallic conductivity. Although orientation of the polymer chains by tensile drawing can enhance the spatial extent of the localized states to a few hundred angstroms, interchain electron transfer is required for delocalization into three dimensions [46].

II. EXPERIMENTAL

A brief description of the relevant experimental techniques that are used in the study of electrical transport in doped conducting polymers (in particular, in the transport laboratory at the Institute for Polymers and Organic Solids at UCSB) is presented in this section. The preparation of $(\text{CH})_x$, PPy- PF_6 , PANI-CSA, and regioregular PAT samples is described in detail in Refs. 21, 25 and 26, 27–30, and 31 and 32, respectively. Four-terminal dc resistivity, magnetoresistance, and thermopower measurements were carried out using a computer-controlled automated measuring system. Electrical contacts were made with conducting carbon paint; in cases where the paint contact adversely affects the measurements, pressure contacts were used. The linearity was checked by measuring voltage versus current, and the resistivity was obtained from the slope of the straight line [34,35].

High pressure conductivity measurements were carried out in a self-clamped beryllium-copper pressure cell [47]. After pressurizing, the cell was clamped at room temperature and then cooled to 1.2 K in a cryostat containing a superconducting magnet (0–10 T). Fluorinert was used as the hydrostatic pressure-transmitting medium. Temperature was measured with a calibrated platinum resistor (300 to 40 K), a calibrated carbon-glass resistor (40 to 1.2 K), and a calibrated cernox resistor (300 to 1.2 K). To avoid sample heating at low temperatures, the current source was adjusted at each temperature so that the power dissipated into the sample was less than $1 \mu\text{W}$. Moreover, to avoid any sample heating, the samples were always immersed directly in liquid helium during measurements below 4.2 K.

Thermopower measurements used the differential technique [48,49] two isolated copper blocks were alternately heated with the sample mounted between the copper blocks with pressure contacts. The heating current was accurately controlled by computer. The temperature difference between the two copper blocks was measured by a chromel-constantan thermocouple and did not exceed 0.5 K for each thermal cycle. The voltage difference across the sample was averaged for one complete cycle. Any temperature difference between sample and thermocouple was less than 10% of the temperature gradient across the sample; the thermometry was carefully calibrated for the entire temperature range (5 K $< T < 300$ K). The absolute thermopower of the sample was obtained from the absolute scale for lead [48,49].

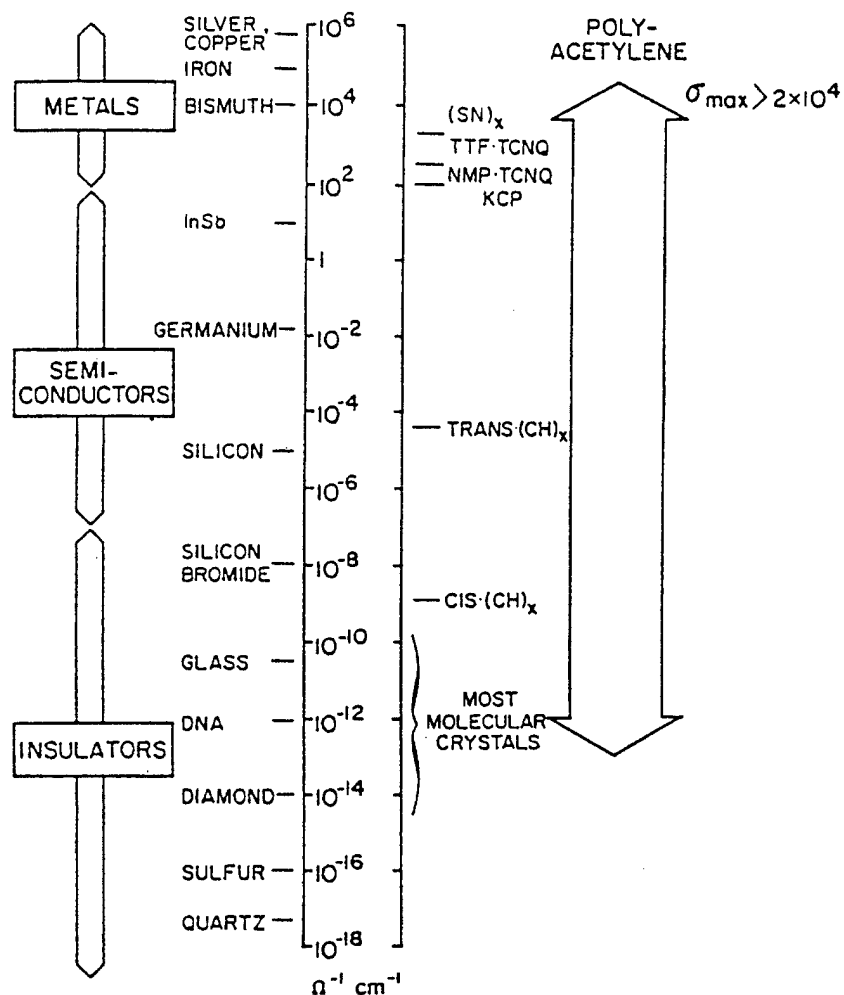


Fig. 2.1 Comparison of the conductivities of doped conducting polymers with those of conventional conductors.

III. RESULTS AND DISCUSSION

A. Disorder-Induced Metal-Insulator Transition

In 1958 Anderson [50] showed that localization of electronic wave functions can occur if the random component of disorder potential is large enough compared to the bandwidth, as sketched in Fig. 2.2. The mean free path (λ) in such a system is given by

$$1/\lambda = 0.7 (1/a) (V_0/B)^2 \quad (1)$$

where a is the interatomic distance, V_0 is the random potential, and B is the bandwidth. The associated broadening of the density of states (vs. energy) due to the random potential is shown in Fig. 2.3. According to Anderson, states will become localized throughout the band for a critical value of V_0/B that is estimated to be of order unity in three dimensions. The wave functions of the

localized states are of the form $e^{-r/\xi} \text{Re}[\psi_0]$, where $\psi_0 = \sum c_n \exp(i\phi_n) \psi_n$; (c_n are the real coefficients, ϕ_n are random phases), and ξ is the localization length, which tends to infinity as V_0/B tends to the critical value [42,43].

In 1966, Mott [42,43] pointed out that the states in the band tails are more susceptible to localization. Consequently, there exists a critical energy separating the localized states from the nonlocalized states, called the mobility edge (E_c). The mobility edge can be expected to play an important role in cases of significant disorder, even when V_0/B is below the critical value.

In 1970, Anderson [51] proposed that a degenerate electron gas in a random disorder potential tends to localize if the magnitude of the disorder potential is large compared with the bandwidth. In such a case all the states become localized, and the system is a "Fermi glass": an insulator with a continuous density of local-

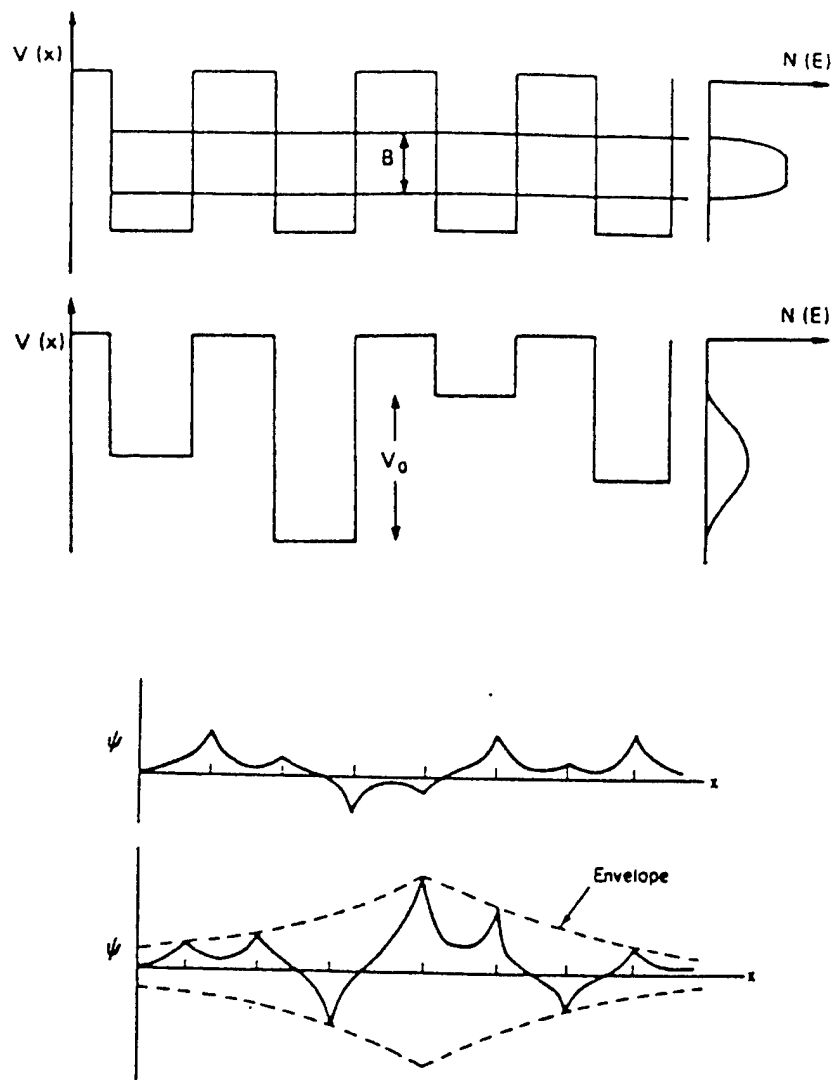


Fig. 2.2 Anderson localization: random potentials versus bandwidth.

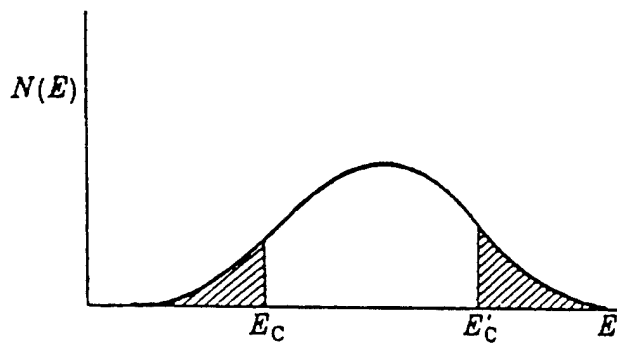


Fig. 2.3 Density of states versus random potential.

ized states (no energy gap) occupied according to Fermi statistics. When the extent of disorder is sufficiently large to induce the Fermi energy (E_F) to cross E_c (in other words, to place the Fermi energy in the region of localized states), there is a transition from the metallic state (finite value of the conductivity as $T \rightarrow 0$) to a nonmetallic state (the conductivity goes to zero as $T \rightarrow 0$). Mott called this disorder-induced M-I transition the "Anderson transition" [42,43]. The localization length increases as the Fermi energy approaches E_c , $\xi \sim a[E_0 / (E_c - E)]^\nu$, where $\nu \approx 1$ and E_0 is a constant.

Based upon the Ioffe-Regel criterion that the lower limit of mean free path is the interatomic spacing [52], Mott proposed [42,43] in 1973 that the M-I transition

that occurs as $E_F \rightarrow E_c$ (from the metallic side) is discontinuous and introduced the concept of the "minimum metallic conductivity," $\sigma_{\min} = 0.03 e^2/3\hbar a$ in three dimensions. In 1979, the scaling theory of localization of Abrahams and coworkers [44,53] demonstrated, however, that the M-I transition is continuous in three dimensions. The conductivity of a metal goes smoothly to zero as $E_F \rightarrow E_c$, so that in general σ_{\min} does not exist. This important progress stimulated extensive theoretical and experimental work, which has been thoroughly reviewed [42-45]. Möbius [54] pointed out, however, that the scaling theory does not completely disprove the existence of σ_{\min} , since the low temperature conductivity data near the M-I transition can be explained alternatively by a combination of σ_{\min} on the metallic side and the Coulomb interaction contribution on the insulating side. The concept of σ_{\min} survives as a qualitative measure of the importance of localization phenomena; systems with $\sigma \sim \sigma_{\min}$ should be considered as near the M-I transition; systems with $\sigma < \sigma_{\min}$ should be viewed as on the insulating side of the M-I transition.

An important parameter for characterizing the disorder is the product of the Fermi wavevector (k_F) and the mean free path (λ), which is the order parameter for the disorder-induced M-I transition; for $k_F\lambda \sim 1$, $\sigma \sim \sigma_{\min}$. In the Fermi glass regime, $k_F\lambda \ll 1$. Recent progress has resulted in conducting polymers on the metallic side of the M-I transition with $k_F\lambda \geq 1$ and $\sigma \geq \sigma_{\min}$. In this situation, the lifetime broadening of the electronic states is less than the Fermi energy ($\epsilon_{F\Gamma} > \hbar$), so a band model can be used as a starting point [42,43,46].

In the strict one-dimensional limit, all wave functions are localized in the presence of disorder. Interchain electron transfer suppresses this extreme tendency toward localization. For a given level of disorder, the strength of the interchain coupling needed to suppress the localization depends on the coherence length along the quasi-one-dimensional chains; an electron must be able to hop to an adjacent chain prior to the resonant backscattering, which inevitably leads to localization in one dimension. Thus, although conducting polymers are correctly referred to as quasi-one-dimensional electronic systems, the interchain coupling can be sufficiently large to enable the formation of three-dimensional metals [46,55]. When such a material is oriented (e.g., by tensile drawing), the properties are those of an anisotropic three-dimensional metal. Without macroscopic orientation, the macroscopic properties of conducting polymers are isotropic, even though on a microscopic level the electronic structure (*intrachain* vs. *interchain*) is highly anisotropic.

The transport properties of disordered systems are sensitive to the presence of both extended and localized states [42-44]. The extent of disorder determines the relative importance of the roles played by localization and by electron-electron (e-e) interactions; the extent of disorder determines the screening length and scattering processes involved in the charge transport. Among

various length scales, the correlation length on the metallic side, the localization length on the insulating side, the e-e interaction length, the thermal diffusion length, and the inelastic scattering length determine the dominant mechanism(s) involved in the transport.

Recent improvements in the quality of doped conducting polymers have presented the opportunity to investigate the disorder-induced M-I transition in these materials. Disorder is an inherent feature of polymers, which often exhibit complex morphology; such systems are often partially crystalline and partially amorphous in nature [56-64]. Since disorder leads to qualitatively different charge transport mechanisms in the homogeneous and inhomogeneous limits, it is important to try to quantify these two limits. The critical parameter is the localization length, L_c ; if L_c is greater than the structural coherence length (which characterizes the length scale of the crystalline regions and thus the length scale for inhomogeneity), the disorder can be viewed as "homogeneous"; the system sees an average. On the other hand, when there are large-scale inhomogeneities, as in a granular metal, the disorder must be viewed as "inhomogeneous."

In the previous generation of conducting polymers, inhomogeneities often dominated the transport properties, and "metallic islands" models were constructed to handle such larger scale granularity [65-70].

The extent of disorder in conducting polymers can be controlled to some degree by the details of sample preparation and processing. Moreover, order can be enhanced by tensile drawing to achieve chain extension, chain orientation, and interchain order. Even in such cases, however, the disorder introduced during the doping process can be substantial. In this review, the transport properties of various doped conducting polymers having a wide range of disorder, on both sides of the M-I transition, are covered.

In the classical definition, a metal should have a positive TCR and $k_F\lambda > 1$, where

$$k_F\lambda = [\hbar(3\pi^2)^{2/3}] / (e^2\rho n^{1/3}), \quad (2)$$

ρ is the resistivity, and n is the number of charge carriers [42,43]. However, the more precise experimental definition of a metal requires that there be a finite conductivity as $T \rightarrow 0$ and that the logarithmic derivative of the temperature dependence of conductivity, $W = \Delta \ln \sigma / \Delta \ln T$, show a positive temperature coefficient [71,72]. In conducting polymers of the previous generation, these metallic features were not prominently observed (with the exception of doped polyacetylene [41,73,74]). However, in the new generation conducting polymers there are examples that exhibit a positive temperature coefficient for W and even exhibit a positive temperature coefficient for the resistivity (TCR) at temperatures above 150 K [33-35]. Even on the metallic side of the M-I transition, however, $\sigma(T)$ is dominated by the interplay

between the important contributions from localization and e-e interactions at low temperatures.

On the insulating side of the M-I transition, $\sigma \rightarrow 0$ as $T \rightarrow 0$, and W shows a negative temperature coefficient [42,43,71,72]. The exponential temperature dependence, $\ln \sigma(T) \propto T^{-x}$ with $x < 1$, on the insulating side of the M-I transition is typical of hopping transport. The exponent x is determined by the extent of disorder, by the dimensionality of the system, and by the morphology, granularity, and microstructure (homogeneous or inhomogeneous). Most of the transport measurements in previous generation conducting polymers were obtained from materials in the insulating regime [65-69,75].

As noted above, in Fermi glass insulators, the Fermi level lies in an energy interval in which all states are localized [42,43,51]. The M-I transition occurs when the disorder is sufficiently weak that the mobility edges move away from the center of the band toward the band tails such that E_F lies in a region of extended states.

The new generation of conducting polymers has made possible detailed studies of the critical regime of the M-I transition, previously unexplored in doped conducting polymers. When the extent of disorder is near the critical disorder for the Anderson transition, the temperature dependence of conductivity follows a power law over a substantial range of temperatures, $\sigma_{\text{crit}} \propto T^{-\beta}$, and W is temperature-independent [76,77]; $W = \beta$. This power law behavior is universal near the critical regime of the M-I transition and does not depend on the details of the system. Thus, the power law temperature dependence plays a key role in defining the critical regime.

“Tuning” through the critical regime by varying the extent of disorder, by varying the interchain interaction through application of high external pressure, and by shifting the mobility edge through application of high magnetic fields has provided insight into the general features of the transport near the M-I transition [78]. Because of the ability to tune through the critical regime, doped conducting polymers have recently become particularly interesting systems for investigation of the transport properties near the M-I transition.

B. Models for the M-I Transition and Transport in Doped Conducting Polymers

The electrical conductivity parallel to the chain axis of a quasi-one-dimensional metallic polymer is given by [46,79]

$$\sigma_{\parallel} = \frac{e^2 n a}{\pi \hbar} v_F \tau = \left(\frac{e^2 n a^2}{\pi \hbar} \right) \left(\frac{\lambda}{a} \right) \quad (3)$$

where n is the conduction electron density per unit volume, a is the carbon-carbon distance along the chain direction, $v_F = 2t_0 a/\hbar$ is the Fermi velocity, $t_0 \approx 1-3$ eV is the π -electron hopping matrix element, and τ is the backscattering lifetime.

The strong interconnection between the electronic

system and the lattice in one-dimensional metals leads to the Peierls transition from metal to insulator and to the formation of a gap at E_F [80]; a corresponding structural distortion also occurs (which is the source of the gap). For light doping levels in such Peierls insulators, the electron-phonon coupling leads to the formation of localized quasiparticles, solitons, polarons, and bipolarons. The stability of these excitations depends on the extent of disorder, dopant-charge carrier interactions, and interchain interactions.

Kivelson and Heeger [81] proposed a first-order transition from soliton lattice to polaronic metal at a critical doping level ($\approx 8\%$) for doped polyacetylene, $(\text{CH})_x$. Recent calculations by various groups indicate, however, that all doping levels the “metallic state” is a soliton lattice [82-86]. This dilemma can be resolved by interchain interactions that lead to true metallic behavior in three dimensions [46]. Theoretical work by Harigaya and coworkers [82,83] has shown that the energy gap can vanish at a certain doping level (e.g., near 8% for doped $(\text{CH})_x$) even when the bond alternation pattern persist (perhaps enhanced by order among the dopant ions). The disappearance of the energy gap can explain the observed M-I transition as a function of dopant concentration as characterized by the onset of the metallic Pauli susceptibility. Calculations by Jeckelmann and Baeriswyl [87] on the one-dimensional Peierls-Hubbard model indicate that quantum fluctuations and interchain coupling tend to reduce the Peierls gap.

According to Stafstrom [85], in the lightly doped regime the dopant potentials stabilize the soliton states and increase the gap between the occupied soliton band and the conduction band. In the heavily doped regime, the dopant potential effect favors a low-band-gap system. Moreover, lattice fluctuations and disorder are not expected to completely destroy the soliton lattice.

In the metallic state of a conjugated polymer, the charged dopant ions adjacent to the chain induce Friedel-type oscillations that can enhance the local infrared-active vibrational (IRAV) modes [87]. Thus, strong IRAV modes cannot be interpreted as evidence of a Peierls gap. Salkola and Kivelson [88] proposed that the arrangement of counterions has a strong influence on the nature of the ground state. They proposed that a semimetallic phase intervenes between the nonmetallic (Peierls) and the metallic (Fermi liquid) phases. Park and coworkers [89-92] proposed a soliton-antisoliton condensation model for doped polyacetylene.

Many models have been proposed, but none are broadly accepted. Thus, although the nature of the M-I transition as a function of dopant concentration in conducting polymers has been heavily studied, the understanding remains incomplete and controversial.

We therefore adopt the point of view that the metallic state exists (quite likely because of the interchain coupling) and that there is a continuous density of states as a function of energy with a well-defined Fermi energy.

In other words, the fundamental electronic structure of heavily doped conducting polymers is that of a metal. Since, however, polymeric systems are inherently disordered, states at the band tails are always localized and there exists a mobility edge that separates the region of the extended states in the interior of the band from the region of localized states. Whether the doped system is a metal or an insulator, then, is determined by the relative position of the Fermi energy with respect to the mobility edge.

Kivelson and Heeger [46] have shown that due to the relatively large π -electron bandwidth (e.g., $4t_0 \approx 10$ eV in polyacetylene) and the relatively small number of thermally excited $2k_F$ phonons in quasi-one-dimensional conducting polymers, the intrinsic conductivity is quite large (only the $2k_F$ phonons can cause the electron back-scattering that limits the conductivity); see Eq. (3). Since even relatively weak interchain coupling ($t_{\perp} \sim 0.1$ eV) is sufficient for three-dimensional delocalization of charge carriers, one can hope to have this quasi-one-dimensional advantage even in the limit of an anisotropic three-dimensional metal. Moreover, since the phonon frequencies are higher than in conventional metals, the intrinsic conductivity is predicted to be very high at room temperature and to increase exponentially as the temperature is lowered. For any t_{\perp} the coherent interchain quantum diffusion of carriers becomes three-dimensional as long as the mean separation between chain breaks is sufficiently great that the chain break concentration (x) is much less than t_{\perp}/t_0 , i.e., $x \ll t_{\perp}/t_0$. Conversely, if $x \ll (t_{\perp}/t_0)^2$, incoherent interchain hopping due to one-dimensional localization will limit the transport [46].

Prigodin and Efetov [93,94] proposed that the M-I transition and the critical behavior in an irregular structure of coupled metallic chains depends on the disorder, the interchain coupling, the localization length, and the number of interchain crossings. In their theory, the following parameters govern $\sigma(T)$: (1) the mean relaxation time (τ), (2) the charge carrier velocity in the direction of the chain (v_F) or the density of states $N(0) = 1/\pi v_F a^2$, and (3) the value of the interchain hopping integral. In quasi-one-dimensional systems, localization takes place if $t_{\perp}\tau < 0.3$, and a transition to the metallic state is observed for $t_{\perp}\tau > 0.3$. For quasi-one-dimensional systems with weak disorder, a crossover from one-dimensional hopping transport at high temperatures to three-dimensional transport at low temperatures was predicted.

Stafstrom [95-97] proposed that an increase in interchain interactions with increasing dopant concentration can induce three-dimensional delocalization of the electronic states; he used the multichannel Buttiker-Landauer formalism [98] to estimate the conductance and localization in a system of coupled conjugated polymer chains and found that both are strongly dependent on the interchain hopping strength.

Among the previous generation conducting polymers, metallic behavior with finite conductivity at millikelvin (mK) temperatures was observed only in doped polyacetylene. Gould et al. [41] and Thummel et al. [73,74] carried out temperature and magnetic field dependence studies of the conductivity in doped $(CH)_x$ down to millikelvin temperatures. Contributions from both weak localization and e-e interactions were observed in the disordered metallic regime. In doped PPV samples, Madsen et al. [99] also observed the e-e interaction contribution to conductivity ($\sigma \propto T^{1/2}$) in metallic samples.

The typical dependence observed for $\sigma(T)$ in previous generation conducting polymers was the exponential behavior characteristic of hopping transport [75],

$$\rho = \rho_0 \exp[T_0/T]^{1/n}$$

Various values of exponent, e.g., $\ln \rho \sim T^{-1/4}$, $T^{-1/3}$, $T^{-1/2}$, T^{-1} , have been reported, and different models have been used to interpret the data, ranging from variable range hopping in different dimensionalities d (with $n = 2$ for 1d, $n = 3$ for 2d, and $n = 4$ for 3d) to a distribution of conjugation lengths.

Sheng's fluctuation-induced tunneling (FIT) model has also been widely used [100,101]. Although this model was originally developed for granular metals (metallic particles in an insulating matrix, such as carbon black particles in insulating polymers), the FIT model has been applied even in the case of highly conducting $(CH)_x$. Voit and Buttner [102] showed that the fitting parameters in the Sheng FIT model are not consistent with the physical properties of conducting polymers. Kaiser and Graham [103] extended the FIT model for heterogeneous systems by introducing geometric factors to the insulating barriers. A different extension of the FIT model was proposed by Paasch [104]. In general, however, the multiple-parameter fitting procedure in FIT models has not been able to provide a satisfactory physical understanding of the transport in doped conducting polymers.

Conwell and Mizes argued [105] that the conduction mechanism is not due to FIT; on the contrary, in their model the conductivity is limited primarily by conjugation defects and chain breaks within the metallic regions. The increase in conductivity with temperature is due to thermal activation (the charge carriers absorb phonons and are thereby activated over the barriers).

Baughman and Shacklette [106,107] proposed that the exponential temperature dependence of the conductivity results from the effect of finite conjugation lengths. They treat the nearest-neighbor interchain hopping in terms of a random resistor network model with a wide distribution of activation energies. A similar correlation between the conjugation length, conductivity, and the exponential temperature dependence of $\sigma(T)$ was put forward by Roth [75].

Recently, Movagh and Roth [108] proposed that the transport properties of doped conducting polymers could be explained by a percolation-type model for inho-

mogeneously disordered systems, a point of view that is very different from Anderson localization in a homogeneously disordered system. Andrade et al. [109] reported computer simulations in a random resistor network model; initial results indicated some correlations between microstructure and transport properties. These models assume that the conductivity decreases exponentially upon lowering the temperature, an assumption that is not true for high quality materials of the new generation of conducting polymers. For example, Ishiguro et al. [110] observed a logarithmic temperature dependence for the resistivity and attributed this weak temperature dependence to low energy excitations associated with relaxation of the molecular conformation at low temperatures.

The "metallic islands" model (a composite model consisting of high conductivity crystalline regions surrounded by insulating amorphous regions) has been used to interpret the transport properties of polyaniline (PANI) protonated by common acids (e.g., HCl, H₂SO₄) [65–69,111,112]. However, analysis of the data according to this model yields a mean free path on the order of 1–100 μm and $k_F\lambda \sim 10^5$, both of which are far too large to be reasonable for a disordered system near the M–I transition. In the "metallic islands" model, both the FIT and the charge energy limited tunneling (CELT) mechanisms [65–69,113,114] were used in attempts to understand the conductivity and thermopower data.

Phillips and Wu [115] and Dunlap et al. [116] proposed a random dimer model that has a set of delocalized conducting states (even in one dimension!) that ultimately allow a particle to move through the lattice almost ballistically. They suggested that this interesting absence of localization in one dimension, despite the disorder, might be applicable to doped conducting polymers.

Recently Zuppiroli and coworkers [117–119] proposed a polaron/bipolaron model involving correlated hopping and multiphonon processes as an explanation for the exponential temperature dependence of conductivity.

To summarize, studies of the temperature dependence of the electrical conductivity of previous generation conducting polymers [65–69,75] have resulted in a somewhat confusing situation. In particular, the strongly activated temperature dependence that was typically observed is more characteristic of an insulator than a metal; the metallic nature anticipated for these doped materials has not emerged.

As described in detail in the following sections, the best way to analyze the temperature dependence of conductivity (or resistivity, ρ) is to plot the logarithmic derivative, $W = -(\Delta \ln \rho / \Delta \ln T)$ against T [71,72]. This plot facilitates the identification of the various regimes of transport. In early publications in the field, the data analysis was not focused on the precise identification of metallic, critical, and insulating regimes. As a result, a comprehensive model for charge transport in conducting

polymers developed slowly. Only recently has the improvement in sample quality sufficiently reduced the dominant role of disorder-induced localization (although it certainly remains important even in the best materials) that genuine metallic properties can begin to be observed in transport property measurements. Studies carried out on materials with a wide range of disorder have shown that the transport properties in the metallic regime, in the critical regime, and in the insulating regime of the disorder-induced M–I transition are distinct and recognizable and that the results obtained in these regimes can be understood in terms of the well-developed theory of the M–I transition.

C. Quantification of Disorder and Identification of the Metallic, Critical, and Insulating Regimes

1. Introduction

Measurements of the resistivity, $\rho(T)$, over a wide range of temperatures (e.g., 1.4–300 K) is the simplest method to begin to identify the various regimes. Since the room temperature conductivities of heavily doped conducting polymers are often comparable to Mott's minimum metallic conductivity [42,43], disorder is the dominant factor in determining the temperature dependence and the classification of the various transport regimes. As emphasized above, since conducting polymers are quasi-one-dimensional, the interchain transfer integral is a parameter of particular importance near the M–I transition; the role of interchain hopping can be explored through application of high pressure (sufficiently high to increase the interchain transfer interaction).

The resistivity ratio,

$$\rho_r = \rho(1.4 \text{ K})/\rho(300 \text{ K})$$

is a useful empirical parameter for quantifying the extent of disorder and for sorting out the various regimes. In general, as the disorder increases, the materials become more insulating, and the conductivity decreases more rapidly upon lowering the temperature; i.e., ρ_r increases.

To explicitly describe the characteristic behavior of $\rho(T)$, we define the reduced activation energy W as the logarithmic derivative of $\rho(T)$ [71,72],

$$W = -T \left(\frac{d \ln \rho(T)}{dT} \right) = -\frac{d \ln \rho}{d \ln T} \quad (4)$$

For best results, sets of data with 50–100 data points should be extracted from the raw data, with the interval of $\ln T = 0.5–1.0$, and successive differences taken to calculate the logarithmic derivatives.

The temperature dependence of W in various regimes is as follows:

1. In the insulating regime, W has a negative temperature coefficient.

2. In the critical regime, W is temperature-independent for a wide range of temperatures.
3. In the metallic regime, W has a positive temperature coefficient.

Although the interaction-localization contributions in the metallic regime and the hopping contribution in the insulating regime were well studied in earlier work on the M-I transition [42–45], the critical regime has only recently been studied in detail.

In the insulating regime, when the resistivity follows the activated temperature dependence characteristic of variable range hopping (VRH), $\ln \rho \propto (T_0/T)^x$, the reduced activation energy becomes

$$\log_{10} W(T) = A - x \log_{10} T \quad (5)$$

where $A = x \log_{10} T_0 + \log_{10} x$. Using Eq. (5), one can determine x from the slope in the plot of $\log_{10} W$ vs. $\log_{10} T$.

For a three-dimensional system in the critical regime of the M-I transition, the correlation length is large and has a power-law dependence on $\delta = |(E_F - E_c)/E_F| < 1$ with critical exponent ν , $L_c = a\delta^{-1/\nu}$, where a is a microscopic length, E_F is the Fermi energy, and E_c is the mobility edge [42–45]. In this critical region [76], the resistivity is not activated but rather follows a power law dependence on the temperature as shown by Larkin and Khmelnitskii [77]:

$$\rho(T) \approx \frac{e^2 p_F}{\hbar^2} \left(\frac{k_B T}{E_F} \right)^{-1/\eta} = T^{-\beta} \quad (6)$$

where p_F is the Fermi momentum and e is the electron charge. The predicted range of validity includes $1 < \eta < 3$, which is consistent with the observed values $0.3 < \beta = 1/\eta < 1$ (see Section III.C on the critical regime for details).

This power law is universal and requires only that the disordered system be in the critical regime where $\delta \ll 1$. A value of $\eta > 3$ indicates that the system is just on the metallic side of the M-I transition. Although $\eta > 3$ is above the theoretical limit for the power law dependence, values for η as large as 4.5 have been reported for *n*-doped germanium near the critical regime [71,72]. At millikelvin temperatures, however, the system becomes either a metal or an insulator depending on the extent of disorder; extension of the power law dependence to $T = 0$ requires that the system be precisely at the critical point. Conducting polymers are particularly interesting for investigations of the critical behavior near the M-I transition because a wide range of parameters that play a significant role can be controlled (e.g., carrier concentration, interchain interaction, and extent of disorder).

Electron-electron interactions also play an important role. According to McMillan's scaling theory [76], the energy scale (correlation gap) as the system crosses over

from the critical regime to the conducting or insulating regime is $\Delta_c = (\hbar D_a/a^2)(a/L_c)^\eta$, where D_a is the diffusion constant. The correlation gap is related to the characteristic crossover temperature (T_{corr}) from the power law dependence of the resistivity at high temperatures to the exponential dependence of the resistivity at low temperature (insulating regime) or to the $T^{1/2}$ dependence of the conductivity with finite $\sigma(T = 0)$ (metallic regime).

For doped conducting polymers, the approximate values of ρ_r in the critical regime of the M-I transition are the following [120]:

1. For nonoriented I-(CH)_x with $\sigma(300 \text{ K}) \approx 800\text{--}1500 \text{ S/cm}$, $\rho_r \approx 50\text{--}100$.
2. For oriented I-(CH)_x with $\sigma(300 \text{ K}) \approx 5000\text{--}8000 \text{ S/cm}$, $\rho_r \approx 8\text{--}16$.
3. For oriented K-(CH)_x with $\sigma(300 \text{ K}) \approx 4000 \text{ S/cm}$, $\rho_r \approx 15\text{--}30$.
4. For nonoriented PPy-PF₆ with $\sigma(300 \text{ K}) \approx 200\text{--}400 \text{ S/cm}$, $\rho_r \approx 4\text{--}8$.
5. For nonoriented PANI-CSA with $\sigma(300 \text{ K}) \approx 150\text{--}300 \text{ S/cm}$, $\rho_r \approx 3\text{--}5$.
6. For nonoriented I-P3HT with $\sigma(300 \text{ K}) \approx 1000\text{--}1500 \text{ S/cm}$, $\rho_r < 45$.

Plots of W vs. T for various doped conducting polymers near the critical regime, at ambient pressure and at various magnetic fields, are shown in Fig. 2.4. The temperature-independent W (characteristic of the critical regime) is clearly observed over a significant range of temperature for these different materials and conditions.

The pressure-induced transition from the critical to the metallic regime results from enhancement of the interchain transfer interaction; high pressure is expected to decrease the interchain, van der Waals, spacing while leaving the intrachain, covalent, atomic spacing essentially unchanged. Under pressure, the increased overlap of the π -electron wave functions centered on different chains increases the conductivity both parallel and perpendicular to the chain axis. The pressure-induced crossover from the critical to the metallic regime demonstrates that charge transport perpendicular to the chain axis is an important factor in the M-I transition in quasi-one-dimensional conducting polymers, in agreement with the theoretical predictions [46].

Since an ideal one-dimensional system would not be sensitive to the magnetic field, the magnetic field induced transition from the critical regime to the insulating regime provides unambiguous evidence of the importance of interchain transport. Khmelnitskii and Larkin [121] have presented a scaling argument that indicates that the mobility edge can be shifted with respect to the Fermi energy by a magnetic field. There is, however, no detailed microscopic theory for describing the effect of a magnetic field on the M-I transition, particularly in a highly anisotropic (quasi-one-dimensional) system. The overlap of the wave functions in a quasi-one-dimen-

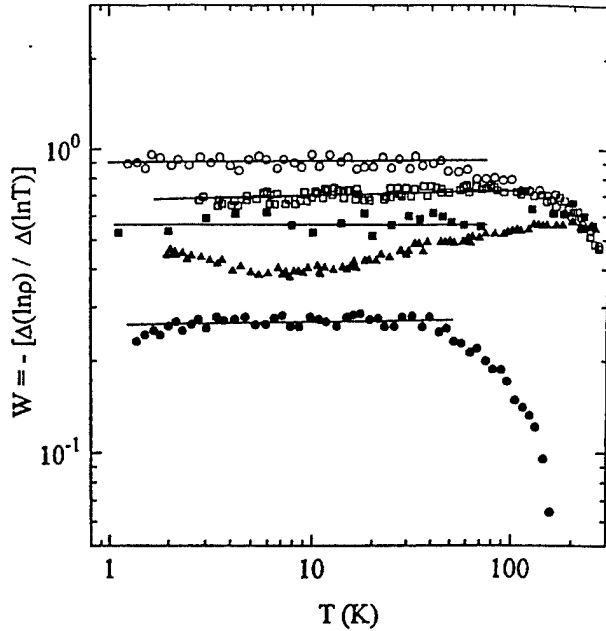


Fig. 2.4 Log-log plot of W vs. T for unoriented I-(CH)_x (○); oriented I-(CH)_x (□); oriented K-(CH)_x (■); PPy-PF6 (▲); PANI-CSA (●). The straight lines are drawn to guide the eye.

sional metal is rather sensitive to magnetic field, since the field tends to shrink the wave functions [122,123]. The field-induced crossover from the critical regime to variable range hopping (VRH) among localized states is consistent with a field-induced shift of the mobility edge with respect to the Fermi level. The crossover occurs when the localization length and magnetic length $[(\hbar c/eH)^{1/2}]$ become comparable.

2. PANI-CSA

For PANI-CSA samples in the critical regime, ρ_r falls in the range 2.5–3.5 [34,35,120]. The sample-to-sample variation of the critical exponent (η) in the power law temperature dependence correlates with ρ_r ; samples with smaller ρ_r give smaller values of η , and those with larger ρ_r give larger values of η . The temperature range over which the dependence is a power law is wider for samples with smaller values of η . A log-log plot of W vs. T for PANI-CSA (nonoriented, cast from solution) is shown in Fig. 2.5. For the data in Fig. 2.5, $\rho_r = 3$ and $\eta = 3.8$. The power law regime extends from 1.4 to 40 K as shown by the temperature independence of $W(T)$, at ambient pressure, in Fig. 2.5.

Two examples are shown in Fig. 2.6, $\rho(T) \propto T^{-0.26}$, where $\eta = 3.8$, and $\rho(T) \propto T^{-0.36}$, where $\eta = 2.8$. The linearity on the log-log plot from 1.4 to 40 K demonstrates that

$$\rho(T,0) = \rho_{0m}(T/T_{0m})^{-\beta}$$

where ρ_{0m} and T_{0m} are constants.

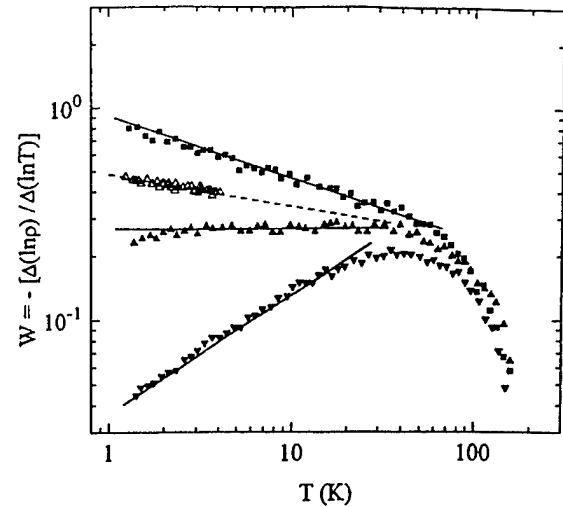


Fig. 2.5 Log-log plots of W vs. T for PANI-CSA in the metallic regime (▼); the critical regime at ambient pressure and $H = 0$ (▲) and at ambient pressure and $H = 8$ T (△); and the insulating regime (■). The lines are drawn to guide the eye.

Assuming that the resistivity in zero magnetic field follows Eq. (6) with $\eta \approx (0.36)^{-1} = 2.77$, one can compare the prefactor with that obtained from the measurements [34,35]. Using $p_F = \hbar k_F$ and $k_F \approx \pi/2c$, the prefactor is given by $\rho_{0m} \approx e^2 p_F / \hbar^2 \approx 2 \times 10^{-4} \Omega \cdot \text{cm}$. From the data in Fig. 2.6 [with $E_F \approx 1$ eV in Eq. (2)], we obtain $\rho_{0m} \approx 6 \times 10^{-4} \Omega \cdot \text{cm}$, in approximate agreement with the Khmelnitskii–Larkin theoretical value.

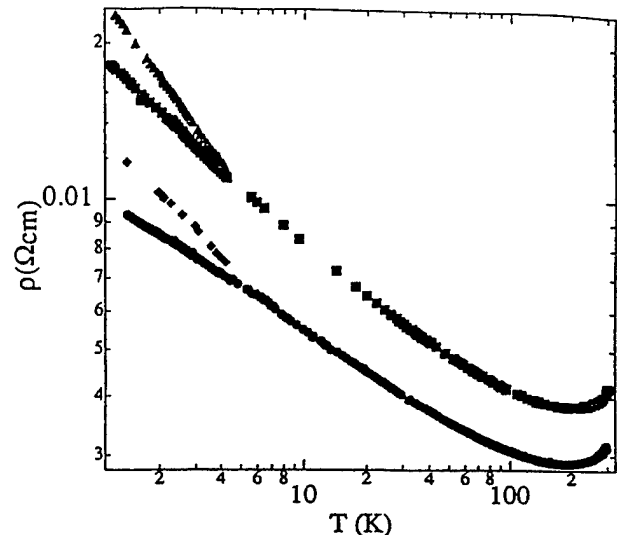


Fig. 2.6 Log-log plot of the $\rho(T)$ vs. T for two PANI-CSA samples in the critical regime: $H = 0$ T (●) and $H = 10$ T (◆) for sample with $\rho(T) \propto T^{-0.26}$, $H = 0$ T (■) and $H = 8$ T (▲) for sample with $\rho(T) \propto T^{-0.36}$.

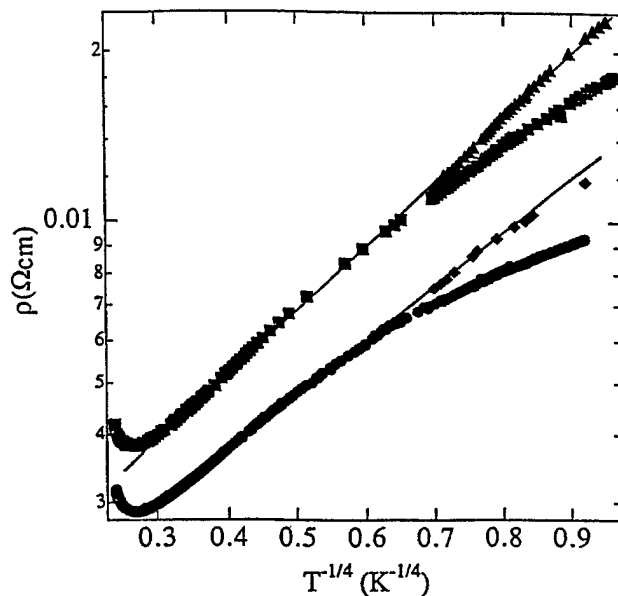


Fig. 2.7 Field-induced crossover from critical regime to VRH. $\rho(T)$ vs. $T^{-1/4}$ for PANI-CSA samples in the critical regime: $H = 0$ T (●) and $H = 10$ T (◆) for sample with $\rho(T) \propto T^{-0.26}$, and $H = 0$ T (■) and $H = 8$ T (▲) for sample with $\rho(T) \propto T^{-0.36}$

Application of a high magnetic field increases the resistivity; for $H = 8$ T, the temperature dependence is stronger than that of a power law, as shown in Fig. 2.6 [34,35]. The $\ln \rho(T, H)$ vs. $T^{-1/4}$ plots for two samples with $\eta = 3.8$ and 2.8 are compared in Fig. 2.7. In both cases, high magnetic fields induce the crossover from power law behavior to VRH. To our knowledge, this crossover as observed in PANI-CSA was not previously observed in any system. The data yield a characteristic VRH hopping temperature; $T_0(H = 10$ T) = 27 K for the sample with $\eta = 3.8$, and $T_0(H = 8$ T) = 56 K for the sample with $\eta = 2.8$. The $T^{-1/4}$ dependence of $\ln \rho(T)$ with such low values of T_0 indicates that the magnetic field truly fine-tunes the system from the critical regime into the VRH hopping regime with very small hopping energies.

Measurements of $\rho(T)$ for a sample close to the critical point were extended down to 20 mK in order to identify the transition from the critical regime to either the insulating or metallic regime (depending upon the extent of disorder in the sample). As shown in Fig. 2.8, the power law dependence persists down to 0.4 K, below which a resistivity increase toward insulating behavior is observed.

The pressure dependence of $\sigma(T)$ of PANI-CSA is more complicated than that of doped $(CH)_x$ and PPy- PF_6 [120]. In PANI-CSA, the magnitude of the conductivity *decreases* above 2 kbar, with an associated stronger temperature dependence at high pressures, both of which might be associated with pressure-induced mor-

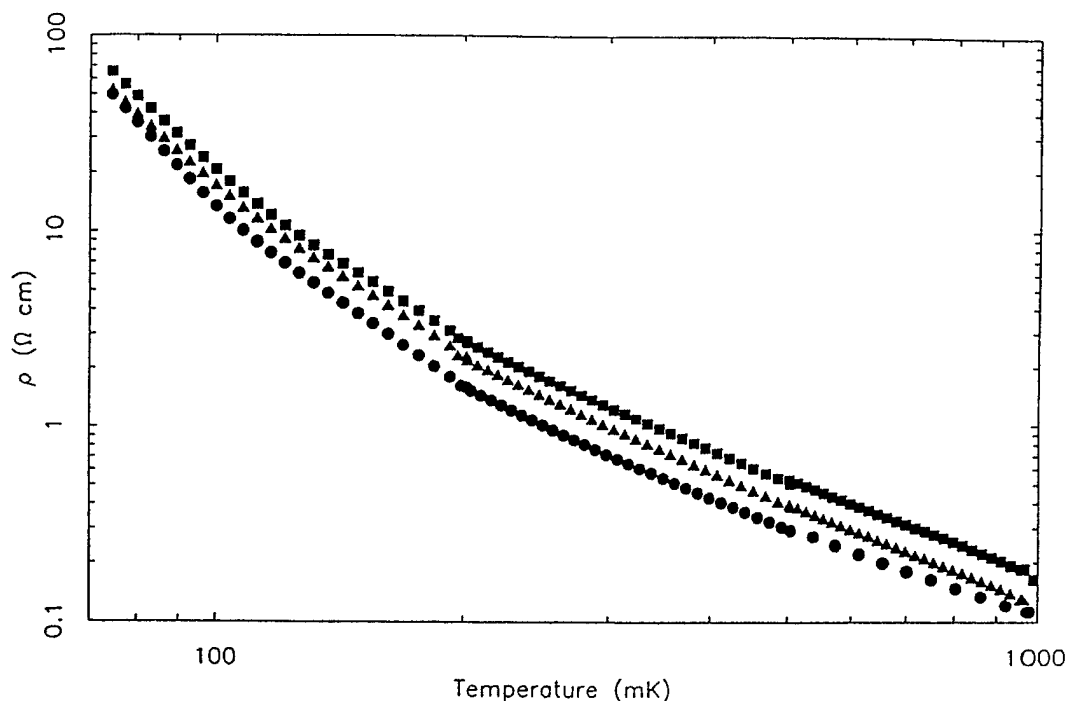


Fig. 2.8 Plot of $\rho(T)$ vs. T for the PANI-CSA sample in the critical regime at $H = 0$ (●), 2 T (▲), and 8 T (■) at millikelvin temperatures.

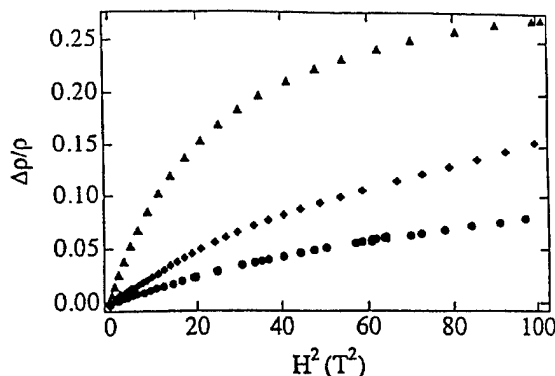


Fig. 2.9 Plot of $\Delta\rho/\rho$ vs. H^2 for PANI-CSA in the critical regime [$\rho(T) \propto T^{-0.2}$]: 4.2 K (●), 2.5 K (◆), and 1.4 K (▲).

ophysical changes. Thus, tuning the critical regime near the M-I transition by pressure for PANI-CSA has not proven to be as interesting as in other conducting polymers.

The magnetoresistance (MR) for PANI-CSA in the critical regime is shown in Fig. 2.9 [34,35]. The MR is positive and larger than in the metallic regime but smaller than in the insulating regime. At 4.2 K, the MR is linear in H^2 up 8 T; for lower temperatures, the initial linear dependence is followed by saturation at higher fields. The qualitative features of the MR are identical in the critical and insulating regimes, although the magnitude of the MR increases dramatically as the system moves into the insulating regime [34,35].

3. K-(CH)_x and I-(CH)_x

Polyacetylene has charge conjugation symmetry and therefore can be *n*-type doped (reduced by electron donors such as potassium, K) or *p*-type doped (oxidized by electron acceptors such as iodine, I) into the metallic regime. The room temperature conductivities (σ_{RT}) of oriented I-(CH)_x and K-(CH)_x samples (in the direction parallel to the chain axis) shown in Figs. 2.10–2.12 are $\sigma_{RT} \approx 12,000$ and 4000 S/cm, respectively [120,124]. In both K-(CH)_x and I-(CH)_x, the conductivity parallel to the chain axis is much higher than that typically found for systems near the M-I transition. However, since the anisotropy of the conductivity (parallel versus perpendicular to the draw axis, $\sigma_{||}/\sigma_{\perp}$) is approximately 100, the conductivity perpendicular to the draw axis is comparable to Mott's minimum metallic conductivity and comparable to that of other known systems near the M-I transition [45].

The room temperature conductivities of the K-(CH)_x sample at ambient pressure and 10 kbar are $\sigma_{RT} \approx 4000$ and 8000 S/cm, respectively [124]. The resistivity ratios for K-(CH)_x are $\rho_r \approx 25$ at ambient pressure and $\rho_r \approx 9$ at 10 kbar. The critical regime can be identified from a log-log plot of W vs. T ; Fig. 2.10 includes data obtained at ambient pressure and at 10 kbar (both at $H = 0$) and data obtained at $H = 8$ T with the sample at ambient pressure. The pressure dependence of the conductivity is shown in the inset of Fig. 2.10.

At ambient pressure (and $H = 0$), W is essentially constant from 300 to 1.2 K, implying that these oriented K-(CH)_x samples are in the critical regime. At 10 kbar,

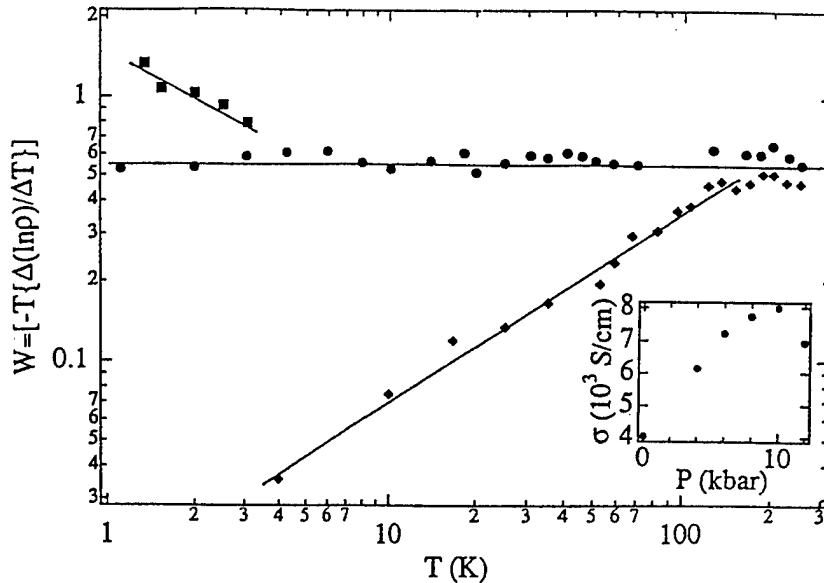


Fig. 2.10 Log-log plot of W vs. T for K-(CH)_x: (●) at ambient pressure and $H = 0$; (◆) at 10 kbar and $H = 0$; (■) at ambient pressure and $H = 8$ T. The inset shows the pressure dependence of conductivity. The lines are drawn to guide the eye.

the positive temperature coefficient of $W(T)$ indicates that the system has crossed over into the metallic regime, qualitatively consistent with expectations based on increased interchain transfer at high pressures.

The negative temperature coefficient of $W(T)$ at $H = 8$ tesla (see Fig. 2.10) implies a magnetic field induced crossover from the critical regime to the insulating regime (the large positive MR in $K-(CH)_x$ is consistent with the presence of strong disorder [124]). The magnetic field induced transition from power law to VRH hopping temperature dependence ($\ln \rho \propto T^{-1/4}$) is shown in Fig. 2.11; the results are similar to those obtained for PANI-CSA in the critical regime [34,35].

Log-log plots of W vs. T for $I-(CH)_x$ (current parallel to the chain axis) are shown in Fig. 2.12. The pressure dependence of the conductivity is shown in the inset of Fig. 2.12; for this sample, the room temperature conductivities parallel to the chain axis are $\sigma_{RT} \approx 11,000$ S/cm at ambient pressure and $\sigma_{RT} \approx 9300$ S/cm at 8 kbar [120,125,126]. Note that $\sigma(P)$ goes through a maximum at approximately 4 kbar. Although the conductivity at 8 kbar is lower than that at ambient pressure, the temperature dependence of conductivity is weaker (more nearly “metallic”) at the highest pressures, an interesting result that is not understood. The values of ρ_r for $I-(CH)_x$ are $\rho_r \approx 3$ at ambient pressure and $\rho_r \approx 2$ at 8 kbar. The conductivity in the direction perpendicular to the chain axis is lower by two orders of magnitude. At 8 kbar, the

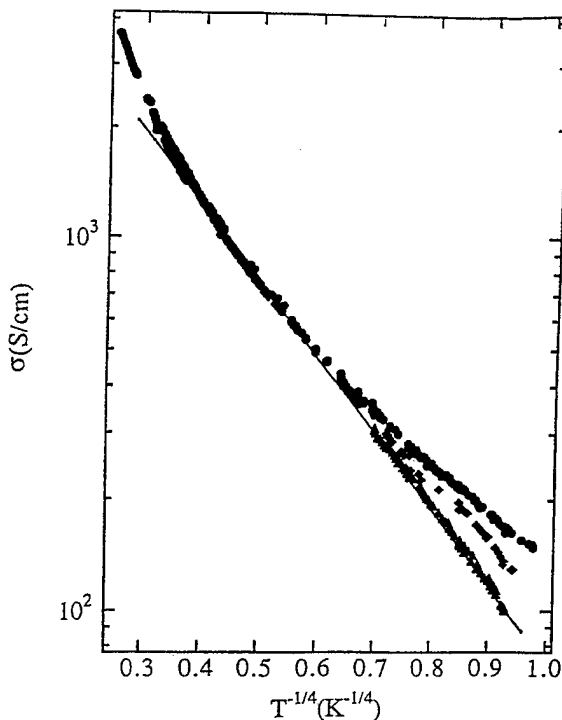


Fig. 2.11 Plot of $\ln \sigma(T)$ vs. $T^{-1/4}$ for $K-(CH)_x$ at $H = 0$ (●), 4 T (◆), and 8 T (▲) (at ambient pressure).

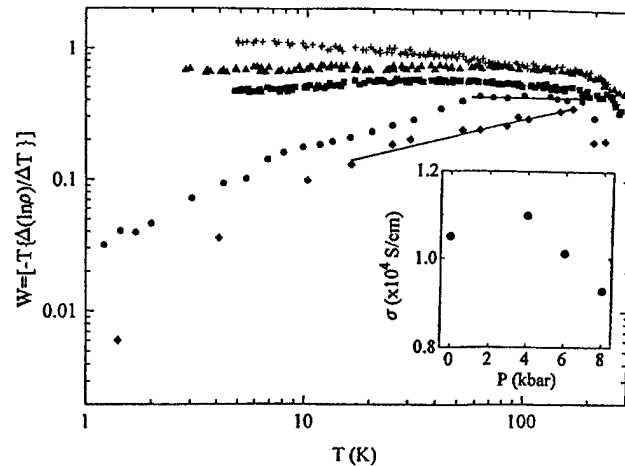


Fig. 2.12 Log-log plot of W vs. T for $I-(CH)_x$: at ambient pressure and $H = 0$, $\rho_r \approx 3$ and $\sigma_{RT} \approx 11,000$ S/cm (●); at 8 kbar and $H = 0$, $\rho_r \approx 2$ and $\sigma_{RT} \approx 9500$ S/cm (◆); at ambient pressure and $H = 0$, $\rho_r \approx 9$ and $\sigma_{RT} \approx 7000$ S/cm (■); at ambient pressure and $H = 0$, $\rho_r \approx 17$ and $\sigma_{RT} \approx 3500$ S/cm (▲); and at ambient pressure and $H = 0$, $\rho_r \approx 32$ and $\sigma_{RT} \approx 2450$ S/cm (+). The inset shows the pressure dependence of conductivity for sample (●). The lines are drawn to guide the eye.

enhanced interchain transport reduces the anisotropy by a factor of about 1.6 (e.g., from $\sigma_{||}/\sigma_{\perp} \approx 105$ at 1 bar to $\sigma_{||}/\sigma_{\perp} \approx 66$ at 8 kbar).

For the sample with $\sigma_{RT} \approx 11,000$ S/cm and $\rho_r \approx 3$, $W(T)$ is temperature-independent at ambient pressure over the limited temperature range from 180 to 60 K. As ρ_r gradually increases, this critical behavior crosses over to a negative temperature coefficient for $W(T)$ (insulating regime), as shown in Fig. 2.12. For $T < 60$ K, $W(T)$ shows a weak positive temperature coefficient for the samples having $\rho_r \approx 3$, indicating that the system is close to the metallic “boundary.” However, at 8 kbar for samples having $\rho_r \approx 3$, $W(T)$ exhibits a strong positive temperature coefficient in the temperature range (from 1.3 to 180 K). Thus, by improving the interchain transport, it is possible to cross over into the metallic regime.

The magnetic field dependence of the conductivity in $I-(CH)_x$ is more complex than in $K-(CH)_x$ due to the interplay of weak localization, electron-electron interactions, and anisotropic diffusion coefficient contributions to the magnetoconductance as described below [125–128].

4. PPy-PF₆

Log-log plots of W vs. T for PPy-PF₆ are shown in Fig. 2.13. The room temperature conductivity of PPy-PF₆ samples in the critical regime is typically $\sigma_{RT} \approx 200$ –300 S/cm [121] with $\rho_r \sim 3$ –6. For the data in Fig. 2.13, the

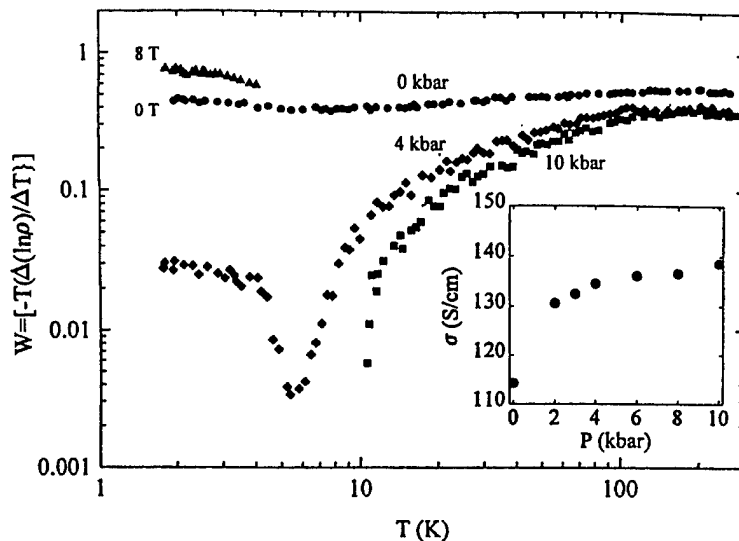


Fig. 2.13 Log-log plot of W vs. T for PPy-PF₆: at ambient pressure and $H = 0$ (●); at 4 kbar and $H = 0$ (◆); at 10 kbar and $H = 0$ (■); and at ambient pressure and 8 T (▲). The inset shows the pressure dependence of conductivity.

values of ρ_r are approximately 11, 2.6, and 2 at ambient pressure, 4 kbar, and 10 kbar, respectively.

The pressure dependence of the conductivity at room temperature is shown in the inset of Fig. 2.13. Although the positive temperature coefficient of $W(T)$ at 4 kbar indicates a crossover from the critical regime to the metallic regime, the temperature-independent $W(T)$ below 4 K shows that it is only marginally metallic. Thus, again, the interplay of the critical and metallic regimes can be fine-tuned by pressure. At 10 kbar, however, the temperature coefficient of $W(T)$ remains positive to 10 K, whereas below 10 K the slope changes from positive to negative, typical of that of a metal. The negative temperature coefficient of $W(T)$ at 8 T (at ambient pressure), similar to that observed in the case of K-(CH)_x, indicates the crossover from the critical to the insulating regime. This complex scenario of the M-I transition on both sides of the critical regime, depending upon the disorder, the pressure, and the magnetic field, indicates once again that heavily doped conducting polymers are in general in (or close to) the critical regime of the M-I transition.

Although the room temperature conductivity and ρ_r for PPy-PF₆ and PANI-CSA are nearly identical, the conductivity is not the same in the different temperature regimes [34,35,121,129]. The conductivity of PANI-CSA is more strongly temperature-dependent at low temperatures than that of PPy-PF₆. At high temperatures, the converse is true. The localization length for both PANI-CSA and PPy-PF₆ near the critical regime is 100–200 Å, i.e., comparable to the magnetic length at $H = 4$ T (128 Å).

5. Summary

The disorder-induced critical regime of the M-I transition has been observed in K-(CH)_x, I-(CH)_x, PPy-PF₆, and PANI-CSA. The critical regime can be precisely identified from log-log plots of W vs. T ; $W(T)$ is temperature-independent in the critical regime, $W = \beta$, and $\sigma(T) = cT^\beta$. For all four heavily doped conducting polymer systems, the positive temperature coefficient of $W(T)$ observed at high pressures indicates the crossover to the metallic regime. For K-(CH)_x, PPy-PF₆, and PANI-CSA, at 8 T, the negative temperature coefficient of $W(T)$ indicates the crossover from the critical region into the insulating regime. Thus, in heavily doped conducting polymers, the transport can be fine-tuned from the critical regime into the metallic or insulating regimes by pressure and magnetic field, respectively.

D. Transport in the Metallic Regime Near the M-I Transition

1. Introduction

The approximate values of ρ_r for the metallic regime in doped conducting polymers are the following [120]:

1. For nonoriented I-(CH)_x with $\sigma(300\text{ K}) > 1000\text{ S/cm}$, $\rho_r < 20$.
2. For oriented I-(CH)_x with $\sigma(300\text{ K}) > 10,000\text{ S/cm}$, $\rho_r < 3$.
3. For oriented K-(CH)_x with $\sigma(300\text{ K}) > 4000\text{ S/cm}$, $\rho_r < 10$.

4. For nonoriented PPy-PF₆ with $\sigma(300\text{ K}) > 200\text{ S/cm}$, $\rho_r < 3$.
5. For nonoriented PANI-CSA with $\sigma(300\text{ K}) > 200\text{ S/cm}$, $\rho_r < 2$.

In general, the temperature dependence of the conductivity in the metallic regime is relatively weak compared to that in either the critical or insulating regimes. Positive (metallic) TCR has been observed only for PANI-CSA [34,35] and FeCl₃-doped oriented (CH)_x [33,130] above 160 and 220 K, respectively. In other conducting polymers, the magnitude of the negative TCR depends strongly on the extent of disorder.

Log-log plots of W vs. T precisely identify the metallic regime. If the temperature coefficient of W is positive, then the conductivity in the disordered metallic regime at low temperatures is expressed by [42–44]

$$\sigma(T) = \sigma(0) + mT^{1/2} + BT^{p/2} \quad (7)$$

where the term $T^{1/2}$ results from thermally induced electron diffusion through states near the Fermi energy (reduced by electron–electron scattering) and the third term on the right is the correction to the zero-temperature “metallic” conductivity, $\sigma(0)$, due to disorder. The value of p is determined by the temperature dependence of the scattering rate [$\tau^1 \propto T^p$] of the dominant dephasing mechanism. For electron–phonon scattering, $p = 3$; for inelastic electron–electron scattering, $p = 2$ in the clean limit or $p = 3/2$ in the dirty limits. The calculation by Belitz and Wysokinski [132] gives $p = 1$ very near the M–I transition. In the disordered metallic regime, the conductivity depends on three length scales [42–44]: the correlation length L_c describing the M–I transition, the interaction length $L_T = (\hbar D/k_B T)^{1/2}$, and the inelastic diffusion length $L_{in} = (D\tau_{in})^{1/2}$ (where D is the diffusion coefficient and τ_{in} is the inelastic scattering time). In practice, however, it is difficult to distinguish these contributions using only the temperature dependence of the conductivity; finer details of the various contributions can be determined from magnetoconductance (MC) measurements.

Since the magnetoconductance is sensitive to the extent of disorder, it serves as an especially useful probe (compared to other transport measurements) for identifying the microscopic transport mechanisms and scattering processes. The MC in the metallic regime is determined by contributions from weak localization (positive MC for weak spin–orbit coupling, negative for strong spin–orbit coupling), and e–e interaction contributions (negative MC) [45,133,134]. In addition, there is a negative MC contribution from strongly localized states due to wave function shrinkage in a magnetic field [122], the latter being critically dependent on the extent of disorder in the system. Because doped conducting polymers are made up of light atoms with small spin–orbit coupling,

one does not expect the contribution arising from spin–orbit coupling to be important. A small additional contribution to the negative MC could arise from residual hopping transport in highly disordered mesoscopic regions (this contribution is smaller than in the critical and insulating regimes). Three-dimensional calculations of the band structures of heavily doped conducting polymers are necessary for a deeper understanding (for example, scattering processes in multivalley band structures are known to yield an additional negative contribution to the MC).

In disordered metals, electron–electron interactions play an important role in the low temperature transport; $\sigma_I(T)$ can be expressed as [42–44,134]

$$\sigma_I(T) = \sigma(0) + mT^{1/2} \quad (8a)$$

where

$$m = \alpha (4/3 - 3\gamma F_\sigma/2) \quad (8b)$$

$$\alpha = (e^2/\hbar)(1.3/4\pi^2)(k_B/2\hbar D)^{1/2} \quad (8c)$$

$$F_\sigma = 32[(1 + F/2)^{3/2} - (1 + 3F/4)]/3F \quad (8d)$$

The finite temperature correction term due to electron–electron interactions in Eq. (8a) consists of exchange and Hartree contributions [44,45]. The sign of this correction depends on the relative size of the exchange and Hartree terms, which depend on the screening length. In doped semiconductors the sign of the finite temperature correction is related to various parameters such as the degeneracy of the conduction band minima in k space (valleys), intervalley scattering, and mass anisotropy. The Hartree factor (F) is the screened interaction averaged over the Fermi surface; α is a parameter that depends on the diffusion coefficient (D), and γF_σ is the interaction parameter. The value of γ depends on the band structure [135,136]. The coefficient was found to change sign as a function of disorder [44], a change that can be interpreted as being due to a sign change in the term $4/3 - 3\gamma F_\sigma/2$. Usually, the sign of m is negative when $\gamma F_\sigma > 8/9$.

Equations (8a)–(8d) are valid in zero magnetic field; at fields sufficiently high that $g\mu_B H \gg k_B T$, both the zero temperature conductivity and the coefficient of the $T^{1/2}$ term are altered:

$$\sigma_I(H, T) = \sigma(H, 0) + m'T^{1/2} \quad (9a)$$

where

$$m' = \alpha[4/3 - \gamma(F_\sigma/2)] \quad (9b)$$

Using Eqs. (8b) and (9b),

$$\gamma F_\sigma = \left(\frac{3}{8}\right) \frac{m' - m}{3m' - m} \quad (9c)$$

assuming that α , γ , and F_σ are not dependent on the

magnetic field [86]. Thus, the parameters α and γF_σ can be estimated from the values of m and $m' = m(H)$ obtained at $H = 0$ and at $H = 8$ T by using Eqs. (8) and (9), respectively.

The MC at high fields arises mainly from the interaction contribution (weak localization contribution is less important in strong fields) [45]. In the free electron model, using the Thomas-Fermi approximation,

$$F_\sigma = x^{-1} \ln(1 + x) \quad (10)$$

where $x = (2k_F A_s)^2$, and A_s is the Thomas-Fermi screening length. Equations (8d) and (10) yield $0 < F_\sigma < 0.93$ and $0 < F_\sigma < 1$ (note that $F_\sigma \approx 1$ for short-range interactions and $F_\sigma \ll 1$ for long-range interactions). Decreasing γF_σ leads to a change in the sign of m , corresponding to the divergence of screening length near the M-I transition, consistent with McMillan's prediction [76]. Kaveh and Mott [135] argued, however, that the inelastic electron-electron scattering should dominate near the M-I transition.

The magnetic field dependence of the contribution to the MC from electron-electron interactions can be written as $\Delta \Sigma(H, T) = \sigma(H, T) - \sigma(0, T)$ [42-44, 133]

$$\Delta \Sigma_l(H, T) = -0.041 \alpha (g\mu_B/k_B)^2 \gamma F_\sigma T^{-3/2} H^2 \quad (11a)$$

$(g\mu_B H \ll k_B T)$

and

$$\Delta \Sigma_l(H, T) = \alpha \gamma F_\sigma T^{1/2} - 0.77 \alpha (g\mu_B/k_B)^{1/2} \gamma F_\sigma H^{1/2} \quad (11b)$$

$(g\mu_B H \gg k_B T)$

Thus at low and high fields, $\Delta \Sigma_l(H, T)$ is proportional to H^2 and $H^{1/2}$, respectively.

For the low magnetic field regime, we follow Rosenbaum et al. [137, 138] and assume that the contributions to $\Delta \Sigma(H, T)$ that arise from electron-electron interactions and weak localization are additive. Thus, the total low-field magnetoconductance is given by the following.

For weak spin-orbit coupling (positive contribution to MC),

$$\Delta \Sigma(H, T) = -0.041 \alpha (g\mu_B/k_B)^2 \gamma F_\sigma T^{-3/2} H^2 \quad (12)$$

$$+ (1/12\pi^2) (e/c\hbar)^2 G_0 (l_{in})^3 H^2$$

For strong spin-orbit coupling (negative contribution to MC),

$$\Delta \Sigma(H, T) = -0.041 \alpha (g\mu_B/k_B)^2 \gamma F_\sigma T^{-3/2} H^2 \quad (13)$$

$$- (1/48\pi^2) (e/c\hbar)^2 G_0 (l_{in})^3 H^2$$

where $G_0 = e^2/\hbar$ and l_{in} is the inelastic scattering length. The first term on the right-hand side of Eqs. (12) and (13) is the contribution from e-e interactions (negative MC), and the second term on the right-hand side is the contribution from weak localization. The first term can be estimated by using Eqs. (8) and (9). Then, using the slope of $\Delta \Sigma(H, T)$ vs. H^2 in the low-field region, the

second term can be estimated. In this way, the value of the inelastic scattering length can be calculated at each temperature.

2. Iodine-Doped Oriented Polyacetylene

Iodine-doped oriented polyacetylene has been studied extensively by several groups [17, 125-128, 130, 131]. The maximum room temperature conductivity parallel to the chain axis for the best quality oriented I-(CH)_x is on the order of 10^5 S/cm, and the anisotropy is greater than 100.

Recently Mizoguchi et al. [139, 140] showed that the main difference between Shirakawa and Naarmann polyacetylenes is the higher density and higher degree of chain orientation in the latter; the basic features of the spin dynamics are identical in the two kinds of samples. The structural and physical properties of highly conducting polyacetylene have been thoroughly reviewed by Tsukamoto [17]. The crystalline coherence lengths parallel and perpendicular to the chain axis are 120 and 50 Å, respectively. The number of charge carriers in heavily doped samples is on the order of 10^{22} cm⁻³, and the mean free path is approximately 500 Å. The density of states at the Fermi level is approximately 0.3 state per electronvolt per coulomb.

Although resistivities as low as 10^{-5} Ω·cm have been reported for iodine-doped oriented polyacetylene parallel to the draw direction (chain axis), a positive temperature coefficient of the resistivity, typical of a metal, has not been observed.¹ This indicates that defects or transport perpendicular to the chain axis limit the conductivity. We conclude, therefore, that the 500 Å mean free path is not limited by phonon scattering. This implies that significantly higher room temperature conductivities will be achieved as the quality of the material is improved. The absence of any positive temperature coefficient implies that values at least an order of magnitude higher are to be expected; i.e., the intrinsic conductivity at room temperature is greater than 10^6 S/cm.

Comprehensive studies of the dc conductivity and MC in directions both parallel and perpendicular to the chain axis indicate that interchain transport is significant [125, 126]. Transport measurements on oriented iodine-doped (CH)_x have shown that $\rho(T)$, ρ_r , and the MC depend on the extent of disorder [120, 125-128, 130]. For iodine-doped oriented (CH)_x samples having a room temperature resistivity of $\sim 10^{-5}$ Ω·cm, $\rho_r \approx 3$. Although disorder can be reduced by tensile drawing and thereby by orienting the (CH)_x chains, the subsequent doping process introduces disorder [58]. The degree of anisotropy in oriented (CH)_x plays a significant role in the transport properties, especially in the MC. The transport measurements were carried out on oriented samples with a maximum draw ratio of $l/l_0 \approx 5-10$ (where l is final length and l_0 is initial length) [17]. Thus, the absence

of prominent anisotropic features in MC measurements and the rather low values of anisotropy in conductivity (25–50) are due to misaligned chains. Recent work on samples stretch-oriented to draw ratios of 15 showed strong anisotropy in the MC [125,126].

At room temperature, the anisotropy of the conductivity is $\sigma_{\parallel}/\sigma_{\perp} > 100$. The temperature dependences of the conductivity are nearly identical for directions parallel and perpendicular to the chain axis. The anisotropic features in the MC have been interpreted in terms of anisotropy in the diffusion coefficient [141], the electron–electron interactions, and weak localization [125,126].

As noted in Section III.D.1, the combination of disorder and anisotropy can lead to a wide range of behavior in the transport properties of disordered anisotropic metals, where both electron–electron interactions and disorder-induced localization near the M–I transition are important. The field-induced crossover from positive to negative MC results from the subtle interplay of weak localization and electron–electron interaction contributions to the MC. From the MC data it is possible to estimate the inelastic scattering length as a function of temperature; inelastic electron–electron scattering in disordered metals dominates the transport at low temperatures in $I-(CH)_x$ [125,126].

a. Pressure Dependence of Conductivity

The conductivity increases for pressures up to 4 kbar, then gradually decreases, as shown in Fig. 2.14 [125,126]. The data are consistent for both collinear four-probe and Montgomery methods. The increase in conductivity up to 4 kbar is reversible with pressure, whereas the decrease at higher pressures is not reversible. The pressure dependence of conductivity in potassium-doped oriented $(CH)_x$ [124] is nearly identical to that obtained from iodine-doped material [125,126]. The inset in Fig. 2.14 shows the pressure dependence of the conductivity perpendicular to the chain axis. The initial increase in $\sigma(P)$ is attributed to enhanced interchain transport, whereas the decrease above 4 kbar is not understood. At 8 kbar, the anisotropy has decreased by a factor of 1.6, from 110 to 67, at room temperature. The pressure dependences parallel and perpendicular to the chain axis are identical, implying that the macroscopic conductivity in both directions is limited by interchain charge transport.

b. Temperature Dependence of Conductivity

Ishiguro and coworkers have reported extensive measurements of $\sigma(T)$ for iodine-doped [127,128] and $FeCl_3$ -doped [130] $(CH)_x$ down to millikelvin temperatures. Although the room temperature conductivity of $FeCl_3$ - $(CH)_x$ is nearly an order of magnitude lower than that

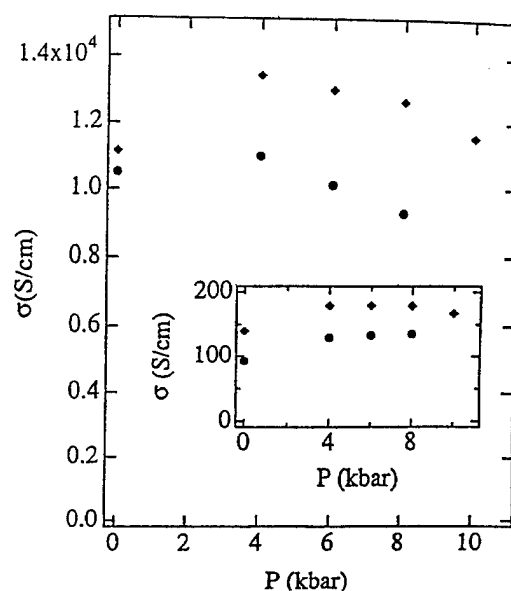


Fig. 2.14 Conductivity parallel to the chain axis versus pressure for $I-(CH)_x$ (inset shows conductivity perpendicular): (●) samples cut parallel (inset perpendicular) to the chain axis for collinear four-probe technique; and (◆) rectangular samples for Montgomery technique.

of $I-(CH)_x$, ρ_r values for $FeCl_3-(CH)_x$ and $I-(CH)_x$ are similar, 1.3 and 2.8, respectively, as shown in Figs. 2.15a and 2.15b. Moreover, the positive TCR for $FeCl_3-(CH)_x$ above 200 K implies that probably the doping is more homogeneous and that the dopant-induced interchain interaction is higher in this system than in $I-(CH)_x$. In the metallic regime, the low temperature conductivity can be explained by the localization–interaction model appropriate to disordered metallic systems. Details on the temperature dependence of the anisotropy for various samples are summarized in Table 2.1. Since doped $(CH)_x$ samples are highly susceptible to oxidative degradation, ρ_r increases with time due to defect formation, reduction in conjugation length, dedoping, etc.

As noted above, the fluctuation-induced tunneling model [100] was widely used to explain the weak temperature dependence of $\sigma(T)$ of doped polyacetylene [142]. Recent results have shown, however, that this model is not satisfactory for highly conducting polyacetylene [127,128,143]. A $\log T$ dependence of $\rho(T)$ was found for samples having $\rho_r \approx 14$ [110]. For highly conducting samples with $\rho_r < 10$, a considerable deviation from the $\log T$ dependence occurs at low temperatures. Plots of ρ versus $\log T$ and $\log \rho$ versus $\log T$ for $I-(CH)_x$ samples having $\rho_r \approx 3$ are shown in Figs. 2.16a and 2.16b. In both cases, the $\log T$ fit deviates below 20 K. Similar results were obtained for $FeCl_3-(CH)_x$ [130]. Thus, the $\log T$ dependence of ρ is observed only in the case of

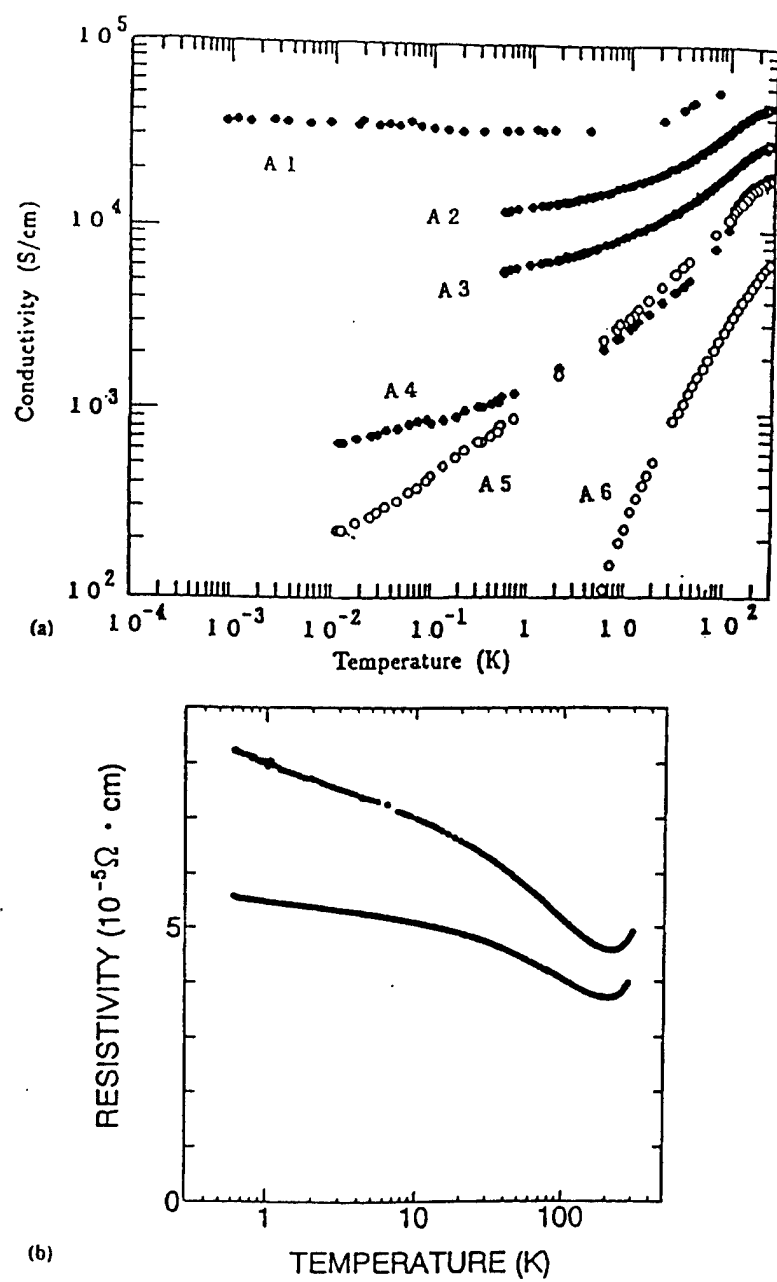


Fig. 2.15 Log-log plot of resistivity $\rho(T)$ or conductivity $\sigma(T)$ vs. T of doped $(CH)_x$ samples. (a) I- $(CH)_x$ samples (data from Ref. 110). (b) $FeCl_3$ - $(CH)_x$ samples (data from Ref. 130).

Table 2.1 Conductivity and Anisotropy of Conductivity of I- $(CH)_x$ at 250 K and 1.2 K, at Ambient Pressure and 8 kbar, for Current Parallel and Perpendicular to the Chain Axis

	Pressure (kbar)	Temperature	
		250 K	1.2 K
Conductivity σ (S/cm)			
Parallel to chain axis ($\sigma_{ }$)	0	11050	3670
Perpendicular to chain axis (σ_{\perp})	0	105	34.2
Parallel to chain axis ($\sigma_{ }$)	8	8460	3880
Perpendicular to chain axis (σ_{\perp})	8	127	45
Anisotropy of conductivity ($\sigma_{ }/\sigma_{\perp}$)	0	105.2	107.3
	8	66.6	86.3

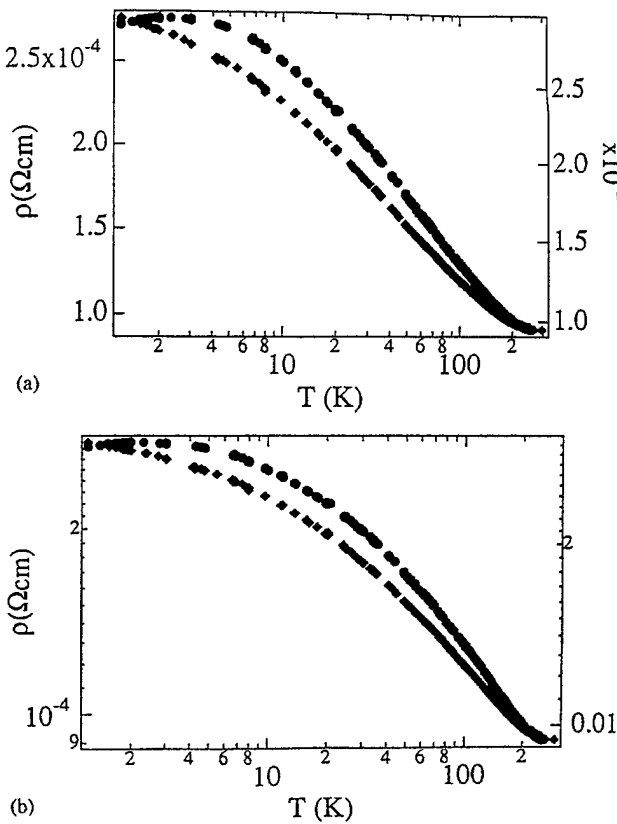


Fig. 2.16 (a) $\rho(T)$ vs. $\log T$ for I-(CH)_x samples with $\rho_r < 3$ (●) parallel to the chain axis (left-hand axis) and (◆) perpendicular to the chain axis (right-hand axis). (b) Log-log plot of resistivity for I-(CH)_x samples with $\rho_r < 3$ (●) parallel to the chain axis and (◆) perpendicular to the chain axis.

(CH)_x samples with intermediate disorder and not for the best materials having $\rho_r < 4$. For these low values of ρ_r , the materials are in the critical regime where $\rho(T) \propto T^{-\beta}$ [120]. As emphasized above, the various regimes are most easily identified from plots of $W(T)$ vs. T .

The $W(T)$ vs. T plots for transport parallel and perpendicular to the chain axis for samples with $\rho_r \approx 3$ are shown in Fig. 2.17 [120,125,126]. Although the anisotropy is nearly 100, $W(T)$ is identical in the two directions. Moreover, for both directions, W is nearly temperature-independent from 180 to 60 K; below 60 K at ambient pressure, the positive temperature coefficient of $W(T)$ indicates that the transport is just on the metallic side of the critical regime. Note that the conductivity parallel to the chain axis is much higher than Mott's minimum metallic value; however, the conductivity perpendicular to the chain axis is on the order of 10^2 S/cm, i.e., close to the Mott value.

At high pressures, both ρ_r and the anisotropy decrease because of the enhanced interchain transport. At 8 kbar, W vs. T exhibits metallic behavior, as shown in Fig. 2.17. When ρ_r gradually increases above 3, the regime where $W(T)$ is temperature-independent extends to lower temperatures, whereas at rather high values of ρ_r (e.g., $\rho_r > 20$), the slope of $W(T)$ vs. T becomes negative as shown in Fig. 2.12. Similar behavior has been observed in highly doped inorganic semiconductors [71,72] as well as in PANI-CSA and PPY-PF₆ [120].

The $T^{1/2}$ and $T^{3/4}$ fits (below 60 K), parallel and perpendicular to the chain axis, are shown in Figs. 2.18a and 2.18b [125,126]. Although the anisotropy is nearly 100, these fits are identical for the two directions, indicating that an anisotropic three-dimensional model is appropriate for highly conducting (CH)_x. The linearity of the $T^{3/4}$ fits is better than that of the $T^{1/2}$ fits, implying

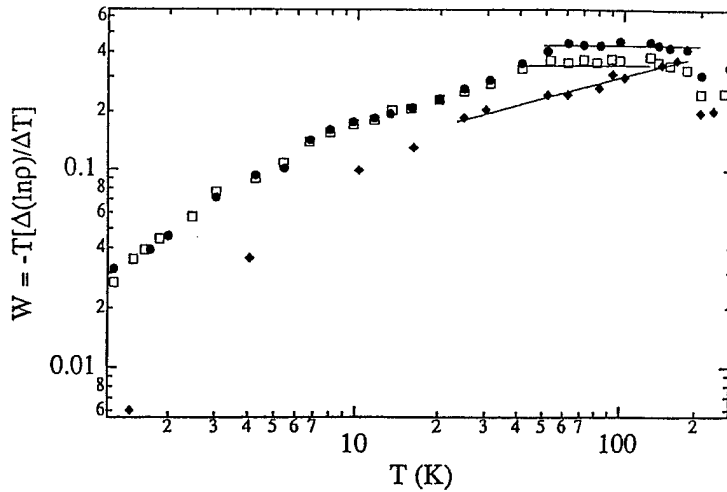


Fig. 2.17 Log-log plot of $W(T)$ vs. T for I-(CH)_x (●) parallel to the chain axis at ambient pressure; (□) perpendicular to the chain axis at ambient pressure; and (◆) parallel to the chain axis at 8 kbar. The lines are drawn to guide the eye.

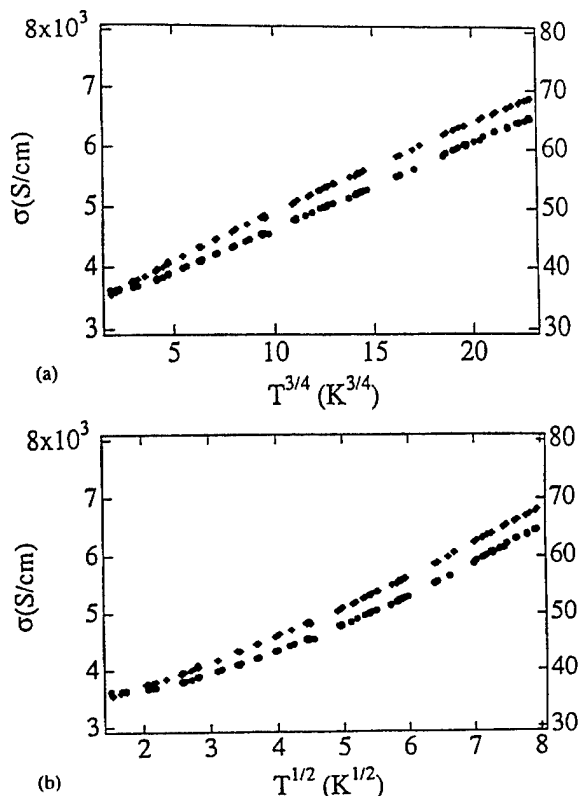


Fig. 2.18 (a) $\sigma(T)$ vs. $T^{3/4}$ for $I-(CH)_x$ and (b) conductivity vs. $T^{1/2}$ for $I-(CH)_x$ (●) parallel to the chain axis; (◆) perpendicular to the chain axis.

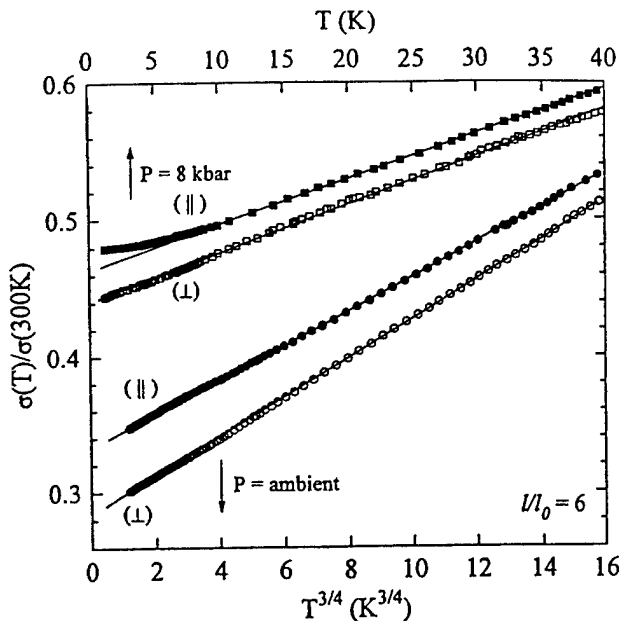


Fig. 2.19 Plots of $\sigma(T)$ vs. $T^{3/4}$ and $\sigma(T)$ vs. T at ambient pressure and at 8 kbar for $I-(CH)_x$ parallel direction to chain axis: $T < 40$ K and $\rho_r < 3$.

that the contribution from localization is dominant at higher temperatures. For temperatures where $\sigma \propto T^{3/4}$, inelastic electron-phonon scattering ($p = 3/2$) is the dominant scattering mechanism. However, when $\sigma \propto T^{1/2}$ ($T < 3$ K), e-e interactions are more important. A pressure-induced crossover from $T^{3/4}$ to $T^{1/2}$ is observed at low temperatures, as shown in Fig. 2.19. Thus, although the localization and interaction effects dominate at high and low temperatures, respectively, the two can be fine-tuned by varying the interchain interactions with pressure, orientation, etc. This has been confirmed from MC measurements as described below.

The temperature dependences of the conductivity at 8 kbar, parallel and perpendicular to the chain axis, are shown in Fig. 2.20 [125, 126]. Although the room temperature conductivity decreases above 4 kbar, the temperature dependence at 8 kbar is substantially reduced. The values of ρ_r , at ambient pressure and at 8 kbar, parallel to the chain axis, are 3 and 2.2 respectively, and those perpendicular to the axis are 3 and 2.8, respectively, demonstrating substantial enhancement of the interchain transport at high pressure. Nevertheless, a positive temperature coefficient of the resistivity has not been observed. Thus, even at high pressure, the combination of weak interchain transport and disorder limit the three-dimensional mean free path in this metallic quasi-one-dimensional conducting polymer.

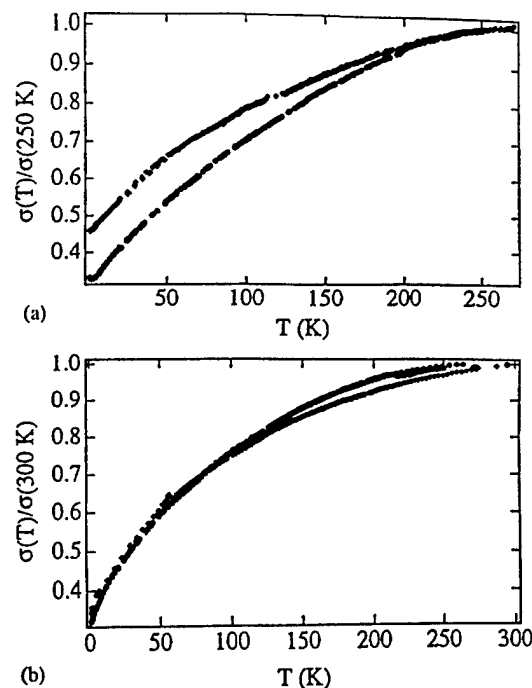


Fig. 2.20 Normalized conductivity [$\sigma(T)/\sigma(250$ K)] vs. T for $I-(CH)_x$ (a) parallel to the chain axis; (b) perpendicular to the chain axis; (●) at ambient pressure; (◆) at 8 kbar.

c. Magnetoresistance

Ishiguro and coworkers reported a detailed study of the magnetoconductance in $I-(CH)_x$ [127,128] and $FeCl_3-(CH)_x$ [130]; the MC features are rather different in the two cases, as shown in Figs. 2.21a and 2.21b. The MC measurements in oriented $I-(CH)_x$ ($l/l_0 \approx 5-10$, $\sigma_{\parallel}/\sigma_{\perp} \approx 25-50$) display a wide range of behavior, including both positive and negative MC [127,128,144]. When ρ_r decreases, the sign of the MC shifts from negative to positive. For samples with intermediate disorder ($\rho_r \approx 3-6$), the sign of the MC was positive when the field was perpendicular to the chain axis, and negative when the field was parallel to the chain axis, at temperatures above 2 K. In both cases (H parallel or perpendicular to the chain axis), the magnitude of the positive MC decreased gradually as the temperature decreased from 10 to 1 K. This indicates that the weak localization contribution (positive MC) dominates at higher temperatures and that the contribution from e-e interactions (negative MC) becomes increasingly important at lower temperatures.

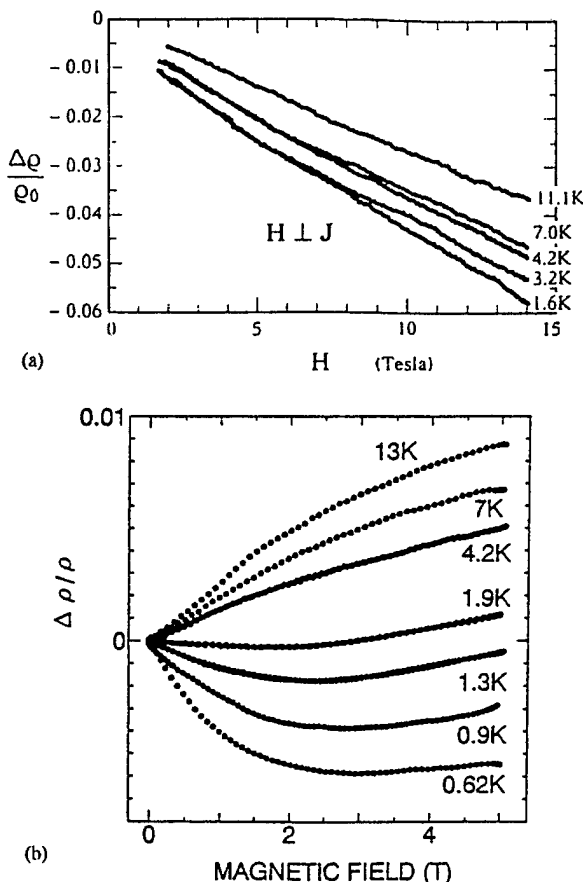


Fig. 2.21 Magnetoconductance [$\Delta\sigma = \sigma(H) - \sigma(0)$] vs. H (a) for $I-(CH)_x$ ($\rho_r < 3$) in the transverse field (data from Refs. 125 and 126) and (b) for $FeCl_3-(CH)_x$ ($\rho_r < 1.5$) in the longitudinal field (data from Ref. 130).

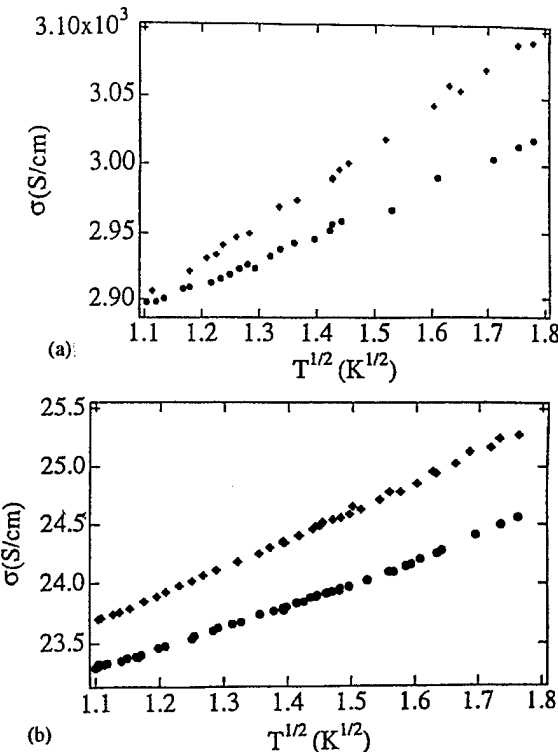


Fig. 2.22 Conductivity versus $T^{1/2}$ for $I-(CH)_x$ (a) parallel to the chain axis and (b) perpendicular to the chain axis (●) at $H = 0$ and (◆) at $H = 8$ T.

When the disorder is weaker ($\rho_r \leq 3$), the weak localization contribution dominates to lower temperatures ($T \leq 2$ K). Thus, the anisotropy in both conductivity and MC is related to the extent of misaligned chains (anisotropy on the molecular scale) and to the anisotropy in the diffusion coefficient.

The $T^{1/2}$ dependence of $\sigma(T)$ is shown in Fig. 2.22 for temperatures below 3 K [125,126]. Although the temperature range of the $T^{1/2}$ fit is rather narrow, this contribution is evident at very low temperatures from the enhanced negative contribution to the MC. The existence of a $T^{1/2}$ term indicates that at very low temperatures the contribution from e-e interactions in disordered metals plays a dominant role.

The values of m , $m(H)$, and γF_{σ} [Eqs. (8) and (9)] are summarized in Table 2.2. The values of $\sigma(0)$, extrapolated to $T \rightarrow 0$, are $\sigma_{\parallel}(0) \approx 3600$ S/cm, $\sigma_{\perp}(0) \approx 30$ S/cm at ambient pressure and $\sigma_{\parallel}(0) \approx 3800$ S/cm, $\sigma_{\perp}(0) \approx 40$ S/cm at 8 kbar. Although $\sigma_{\parallel}(0)$ exceeds values typical of systems near the M-I transition, values of $\sigma(0)$ as large as 4135 S/cm have been reported for Y_xSi_{1-x} [145]. Since the conductivity parallel to the chain axis (on the order of 10^3 S/cm) exceeds that typical of systems near the M-I transition, the values of m and m' are unusually large; correspondingly, the values of m , m' , and σ perpendicular to the chain axis are typical of systems near

Table 2.2 Values of the Parameters m , $m(8\text{ T})$, α , and γF_σ , and Temperature Dependence of the Inelastic Scattering Length (Current Parallel and Perpendicular to the Chain Axis and Field Perpendicular to the Current and Chain Axis) for I-(CH)_x

Field (H) vs. current (I) vs. chain axis (ν)	m^a	$m(8\text{ T})^a$	α	γF_σ	Inelastic scattering length (Å)		
					4.2 K	2 K	1.2 K
$H \perp \nu; I \parallel \nu; H \perp I$	195	316	283	0.43	644	902	1163
$H \perp \nu; I \perp \nu; H \perp I$	1.67	2.3	1.93	0.31	134	170	209

^a In S/(cm·K^{1/2}).

the M-I transition. Thus the localization–interaction model is appropriate for the analysis of MC data in the direction perpendicular to the chain axis.

The MC for current parallel to the chain axis is shown in Figs. 2.23a–2.23c [125,126]. When the field is perpendicular (the current is parallel) to the chain direction, the MC is positive; however, the magnitude of positive

contribution decreases at low temperatures, as shown in Fig. 2.23a, due to the interplay of weak localization and electron–electron interaction contributions. When the field and current are parallel to the chain direction, the sign of MC is always negative, and its magnitude increases at low temperatures, as shown in Fig. 2.23b. This anisotropy is attributed to the anisotropic diffusion coefficient. This is proven by MC measurements under high pressure. At 4.2 K, the conductivity anisotropy is 98 at ambient pressure and 77 at 8 kbar. The enhancement of the interchain interaction at high pressure reduces the anisotropy (both conductivity and diffusion coefficient). The MC at 8 kbar with field and current parallel to the chain axis is shown in Fig. 2.23c. For $H < 4$ T, the sign of the MC has reversed from negative to positive at 4.2 K and 8 kbar; at higher fields, the sign remains negative due to the dominant contribution from electron–electron interactions, as shown in Fig. 2.23c. Finally, the magnitude of negative MC is reduced under pressure at temperatures below 4.2 K, showing that the sign and magnitude of the MC depend on the anisotropic diffusion coefficient in oriented (CH)_x [141].

The MC for current perpendicular to the chain axis is shown in Fig. 2.24. At 4.2 K, the MC is positive when the field and current are perpendicular to the chain direction as shown in Figs. 2.24a and 2.24b. This is due to the dominant contribution from weak localization. Since the contribution from e–e interactions increases at lower temperatures and higher magnetic fields, the sign of the MC reverses from positive to negative at 1.2 K and $H = 4$ T. For the case of current perpendicular and field parallel to the chain axis, the MC is shown in Fig. 2.24c. The sign is negative, similar to when current and field are parallel to the chain direction, as shown in Fig. 2.24b. These data show that the anisotropic MC is not caused by the direction of current with respect to the chain axis; the anisotropic MC is due to the anisotropic diffusion coefficient, which in turn is a function of the angle between the field direction and the chain axis.

Similar anisotropy in the MC has been observed by Ishiguro and coworkers [127,128] (between 4.2 and 1.6 K) for samples having $\rho_r \approx 3–5$, as shown in Figs. 2.25a and 2.25b. Although the sign did not change for samples having $\rho_r \approx 3$, the positive MC is nearly three times as large when the field is perpendicular to the chain axis

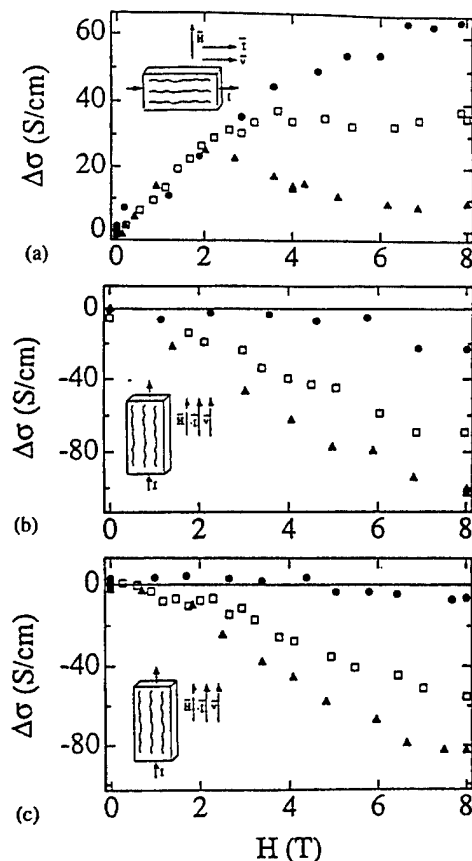


Fig. 2.23 Magnetoconductance versus H for I-(CH)_x at 4.2 K (●), 2 K (□), and 1.2 K (▲). The current is parallel to the chain axis. (a) The field is perpendicular (perpendicular) to the chain axis (current); (b) the field is parallel (parallel) to the chain axis (current) at ambient pressure; (c) the field is parallel (parallel) to the chain axis (current) at 8 kbar.

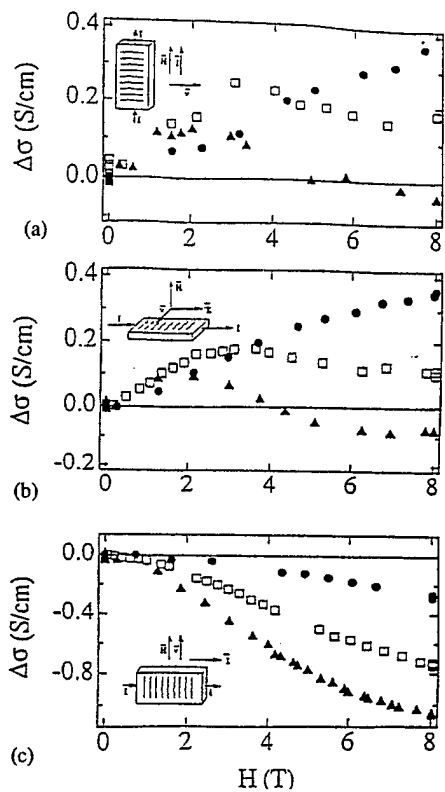


Fig. 2.24 Magnetoconductance versus H for I-(CH)_x at 4.2 K (●), 2 K (□), and 1.2 K (▲). The current is perpendicular to the chain axis (n). (a) The field is perpendicular to the chain axis (parallel to the current); (b) the field is perpendicular to the chain axis and current; (c) the field is parallel to the chain axis (perpendicular to the current).

as when it is parallel to the chain axis, indicating that the interaction contribution to the MC is larger in the latter case due to the anisotropic diffusion coefficient. The field-induced crossover from positive to negative MC shown in Figs. 2.24a and 2.24b results from the interplay of weak localization and e-e interaction contributions.

The inelastic scattering length at different temperatures can be estimated from $l_{in} = (D\tau_{in})^{1/2}$ for directions parallel and perpendicular to the chain axis. At 1.2 K, the inelastic scattering length in the directions parallel and perpendicular to the chain axis are 1163 and 210 Å, respectively. The temperature dependence of the inelastic scattering length is shown in Fig. 2.26. The $T^{-3/4}$ dependence of τ_{in} , in directions parallel and perpendicular to the chain axis, is typical of inelastic electron-electron scattering in disordered metals [42, 43, 125, 126]. This is in agreement with the $T^{3/4}$ dependence of conductivity shown earlier in Fig. 2.18a. Thus, both the conductivity and the MC are consistent with the localization-interaction model of transport in anisotropic disordered metals.

d. Summary

The room temperature conductivity increases up to 4 kbar and then gradually decreases at higher pressures. At 8 kbar, the temperature dependence of σ_{\parallel} and σ_{\perp} have decreased by factors of 1.4 and 1.6, respectively, indicating that interchain transport is enhanced by pressure. $W(T)$ is temperature-independent from 180 to 60 K in directions both parallel and perpendicular to the chain axis, indicating that at ambient pressure I-(CH)_x is on the metallic side of the critical regime. At 8 kbar, the system exhibits more metallic behavior due to enhanced interchain transport. The $\sigma(T) \propto T^{3/4}$ dependence (4–50 K) indicates that inelastic e-e scattering in disordered metals is the dominant scattering process.

The sign and magnitude of the MC are determined by the extent of disorder, the temperature, the degree of chain orientation, and the angle between the magnetic field and the chain axis. In samples with fewer misaligned chains (e.g., $\sigma_{\parallel}/\sigma_{\perp} > 100$) and less disorder ($\rho < 3$), the sign of MC is positive when the field is perpendicular to the chain axis and negative when the field is parallel to the chain axis. Whether the field is parallel or perpendicular to the chain axis, the e-e interaction contribution (negative MC) dominates over the weak localization contribution (positive MC) at high magnetic fields and low temperatures. The anisotropic MC arises mainly from the anisotropic diffusion coefficient, as confirmed by the crossover from negative MC to positive MC and the decrease in the magnitude of the negative MC at 8 kbar. The inelastic scattering length for transport parallel and perpendicular to the chain axis is 1160 and 200 Å, respectively. The $T^{-3/4}$ dependence of inelastic scattering length is consistent with the $T^{3/4}$ dependence of conductivity at low temperatures, indicating that the inelastic electron-electron scattering in disordered metals is the dominant scattering mechanism in I-(CH)_x.

3. Potassium-Doped Oriented Polyacetylene

As noted in Section III.C.3, K-(CH)_x is metallic at high pressures. The positive temperature coefficient of W at higher pressures, as shown in Fig. 2.10, indicates the crossover from the critical regime to metallic behavior [120, 124]. Although the large negative MC is reduced by a factor of 2 at 10 kbar with respect to that at ambient pressure, the extent of disorder is sufficiently important that the dominant contribution to the negative MC is from hopping transport.

Recently Bernier and coworkers [146, 147; D. Bornmann and P. Bernier, private communication] observed rather weak temperature dependence ($\rho_r < 2$) with a positive TCR below 7 K at various doping levels in K-(CH)_x. The correlation between the staging-induced structural transitions and the electronic properties in K-(CH)_x are in the preliminary stages of investigation [Bor-

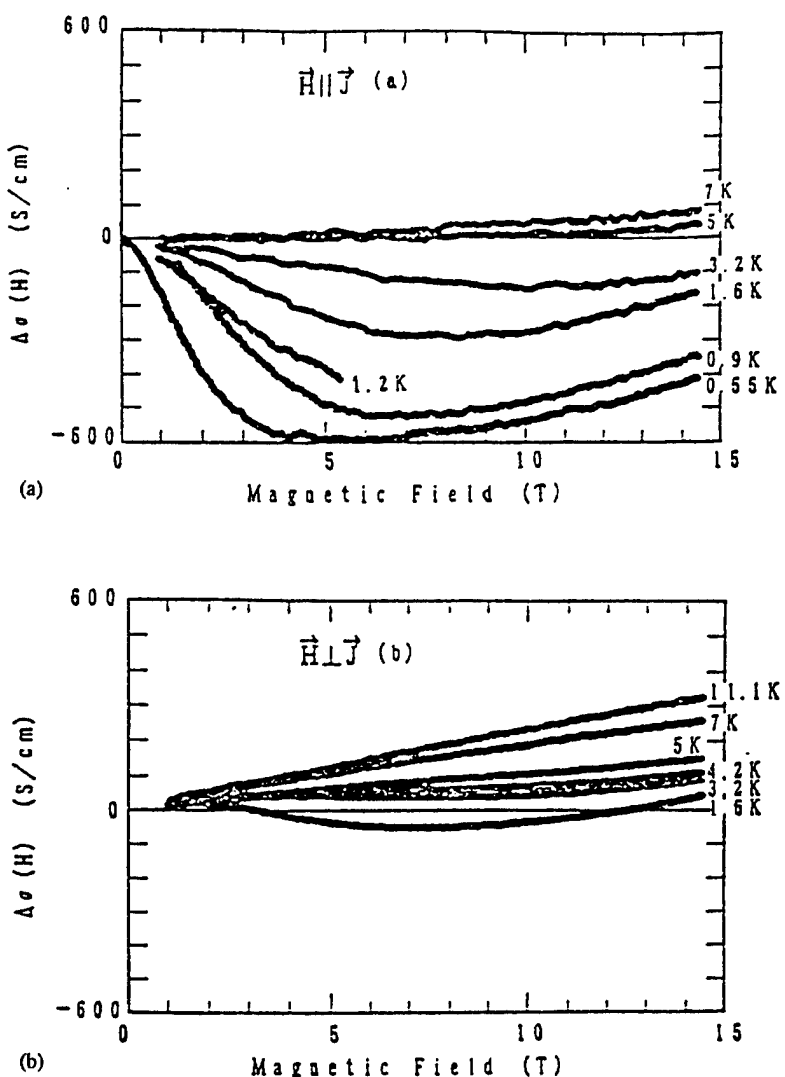


Fig. 2.25 Magnetoconductance versus H of $\text{I}-(\text{CH})_x$ ($\rho_r \approx 3.7$) (a) for longitudinal field; (b) for transverse field. (From Ref. 127.)

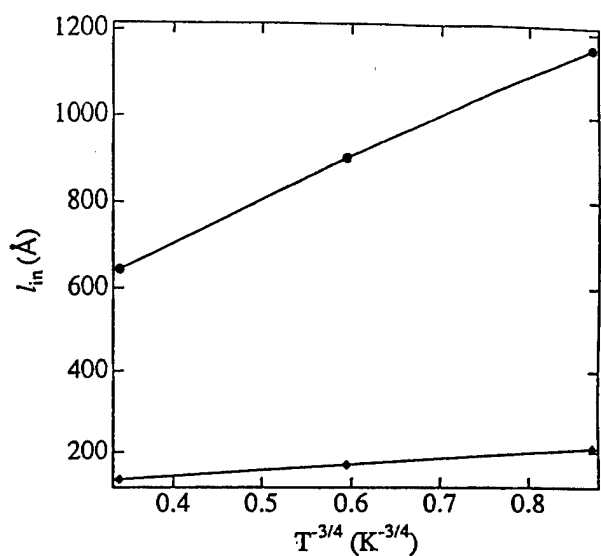


Fig. 2.26 The inelastic scattering length versus $T^{-3/4}$ for $\text{I}-(\text{CH})_x$ (●) parallel and (◆) perpendicular to the chain axis.

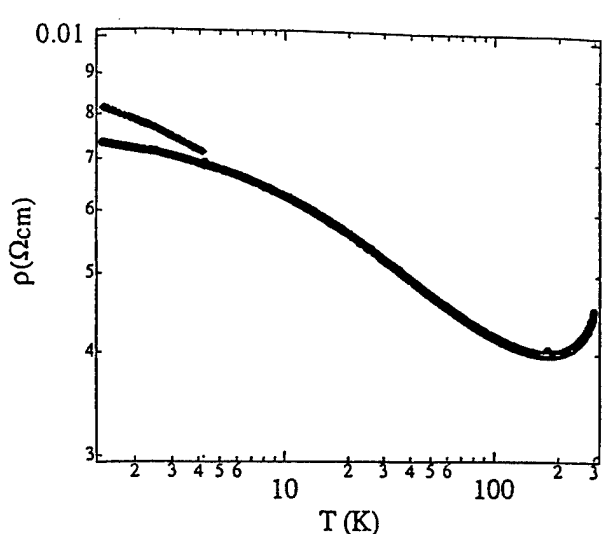


Fig. 2.27 Log-log plot of $\rho(T)$ vs. T for PANI-CSA in the metallic regime: $H = 0$ T (●) and $H = 8$ T (◆).

mann and Bernier, private communication; 146–148]. Thus more work is necessary to fully characterize the M-I transition and the metallic regime in alkali metal doped $(CH)_x$.

4. PANI-CSA

a. Temperature Dependence of the Conductivity

PANI-CSA is metallic when prepared by casting from solution in *m*-cresol [34,35]. The metallic regime is characterized by $\rho_r \approx 1.5$ –2 and by a positive temperature coefficient of W (below 40 K), as shown in Fig. 2.27a. Although $\rho(T)$ increases at low temperature, the temperature dependence is extremely weak; the system has crossed over from the power law dependence characteristic of the critical regime to “metallic” behavior. Application of an 8 T external magnetic field increases the low temperature resistivity as shown in Fig. 2.27a. In an external magnetic field of 8 T, the temperature dependence approaches the power law regime, implying that the external field moves the system toward the critical regime ($\delta \rightarrow 0$). Even for $H = 8$ T, however, log-log plots show residual curvature, indicating that the metallic regime of PANI-CSA is robust. Moreover, the recent observation of large negative dielectric constant in the microwave regime by Joo et al. [149,150], as shown in

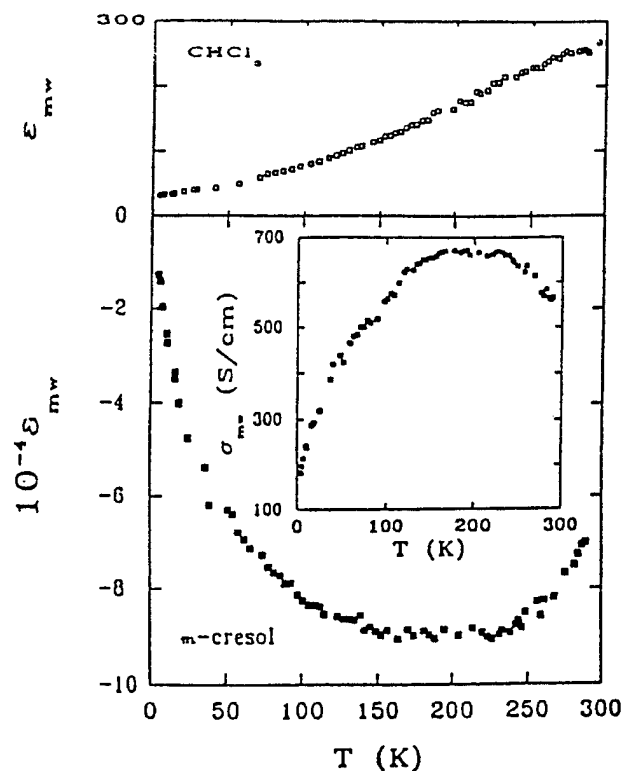


Fig. 2.28 Dielectric constant [$\epsilon(6.5 \times 10^9$ Hz)] vs. T for PANI-CSA (*m*-cresol). (From Ref. 149.)

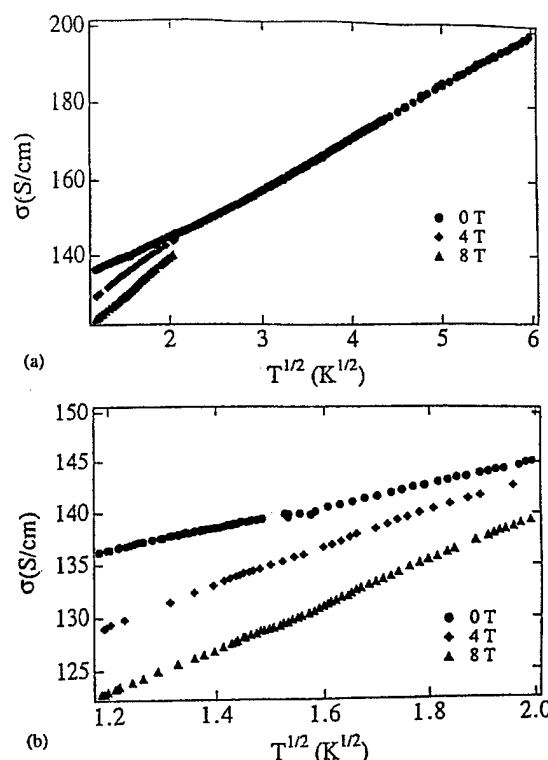


Fig. 2.29 (a) Plot of σ vs. $T^{1/2}$ for PANI-CSA in the metallic regime at $H = 0$, 4 T, and 8 T. (b) Data below 4.2 K are shown on an expanded scale.

Fig. 2.28, has confirmed the metallic nature of PANI-CSA.

The temperature dependence of the conductivity with $\rho_r = 1.6$ is plotted as $\sigma(T)$ vs. $T^{1/2}$ in Figs. 2.29a and 2.29b [34,35]. The $T^{1/2}$ dependence is in agreement with Eq. (8a) and consistent with metallic behavior near the M-I transition [the $T^{1/2}$ dependence implies that $p = 1$ in Eq. (7)]. The data yield $\sigma(T) = \sigma(0) + mT^{1/2}$ with $m(0) = 10.8$ S/(cm·K) $^{1/2}$. Figures 2.29a and 2.29b show $\sigma(T)$ vs. $T^{1/2}$ for $H = 0$, 4 T, and 8 T; the magnetic field decreases the low temperature conductivity (positive magnetoresistance). At low temperatures, shown in greater detail in Fig. 2.29b, the slope of σ vs. $T^{1/2}$ is field-dependent, as predicted by Eq. (9).

The temperature dependence of the resistivity of metallic PANI-CSA is shown for temperatures down to 75 mK in Fig. 2.30 [151]. The relatively large conductivity ($\sigma \approx 30$ S/cm) at ultralow temperatures confirms the metallic nature of PANI-CSA. The resistivity at $H = 0$, 2 T, and 8 T shows a minimum (vs. T) that could be due to the interplay of weak localization and electron-electron interaction contributions at millikelvin temperatures. The field dependence of the resistivity at these temperatures demonstrates the robust nature of the three-dimensional transport and the absence of one-dimensional localization.

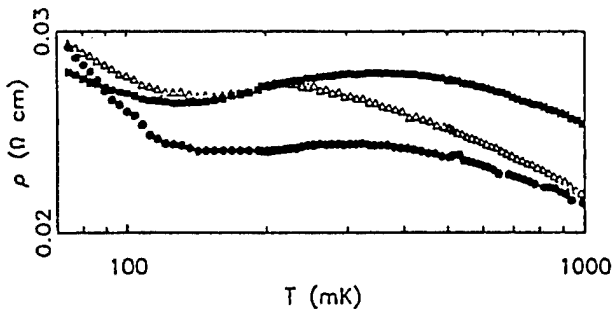


Fig. 2.30 Data of $\rho(T)$ vs. T for PANI-CSA in the metallic regime at 0 T (●), 2 T (Δ), and 8 T (■). (From Ref. 151.)

b. Magnetoconductance

In the metallic regime, the negative MC of PANI-CSA is relatively weak compared to that in the critical or insulating regimes [34,35]. The dependence of the MC

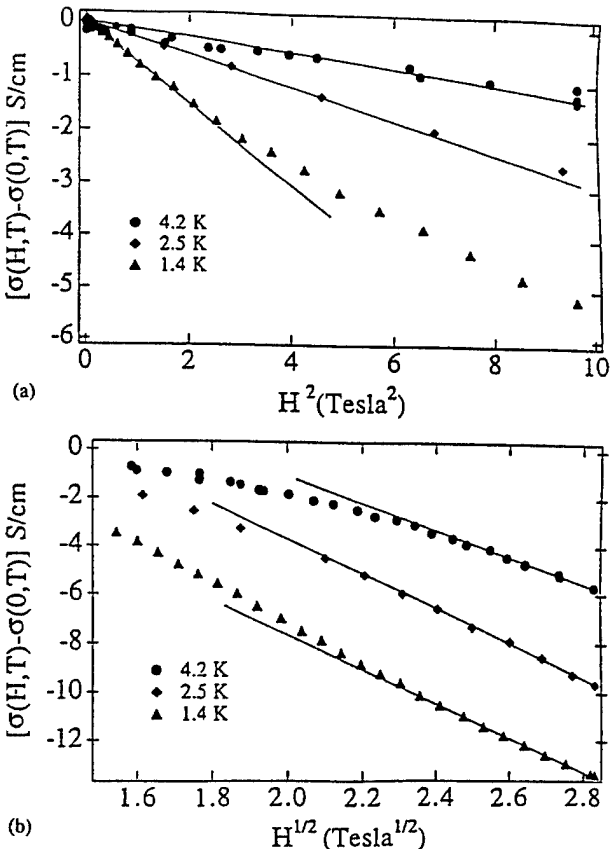


Fig. 2.31 Magnetoconductance (MC) for PANI-CSA in the metallic regime at 4.2 K, 2.5 K, and 1.4 K. (a) MC vs. H^2 ; the solid lines indicate H^2 dependence. (b) MC vs. $H^{1/2}$; the solid lines indicate $H^{1/2}$ dependence.

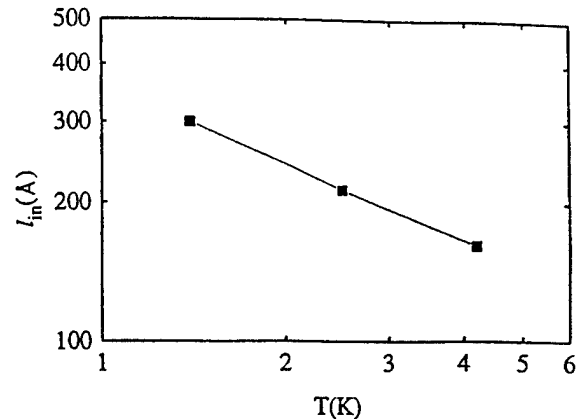


Fig. 2.32 Inelastic scattering length (l_{in}) vs. T for PANI-CSA in the metallic regime.

on H^2 and $H^{1/2}$ at low and high fields, respectively, is shown in Figs. 2.31a and 2.31b. The magnetic field decreases the zero-temperature conductivity (negative MC) and increases the slope of σ vs. $T^{1/2}$; both effects result directly from electron-electron interactions and arise predominantly from the Zeeman splitting of the spin-up and spin-down bands [44]. The values for α and γF_σ determined by using Eq. (8), (9), and (11) are $\alpha \approx 18.3$ and $\gamma F_\sigma \approx 0.5$. This relatively small value for γF_σ is comparable to that found in studies of doped semiconductors at doping levels near the M-I transition [134].

The inelastic scattering length estimated from $\tau_{in} = (l_{in})^2/D$ is shown in Fig. 2.32; $l_{in} \propto T^{-1/2}$, $\tau_{in} \propto T^{-1}$. Using the known value of $\alpha = 18.3$, D can be calculated from Eq. (8c); $D \approx 1.25 \times 10^{-2} \text{ cm}^2/\text{s}$. We conclude, therefore, that at 4.2 K, $\tau_{in} \sim 10^{-10} \text{ s}$, which is the same as that reported for potassium-doped polyacetylene [73,74] and various other amorphous metals [152]. The T^{-1} temperature dependence of τ_{in} is in agreement with the theoretical prediction of Belitz and Wysokinski [132] for systems very close to the M-I transition. The same T dependence has been observed in metallic Si:B near the M-I transition.

The MC measurements down to 20 mK at 16 T [151] are shown in Fig. 2.33. The data indicate the H^2 and $H^{1/2}$ dependence of negative MC at low and high fields, respectively. The absence of saturation of the negative MC at 20 mK and 16 T suggests the interesting possibility of an open Fermi surface for PANI-CSA.

c. Intrinsic Conductivity and Metallic Nature of PANI-CSA

The inelastic scattering length can be estimated from $\tau_{in} = (l_{in})^2/D$; $l_{in} \sim 150-300 \text{ \AA}$ [34,35]. This enables an estimate of the intrinsic conductivity parallel to the chain

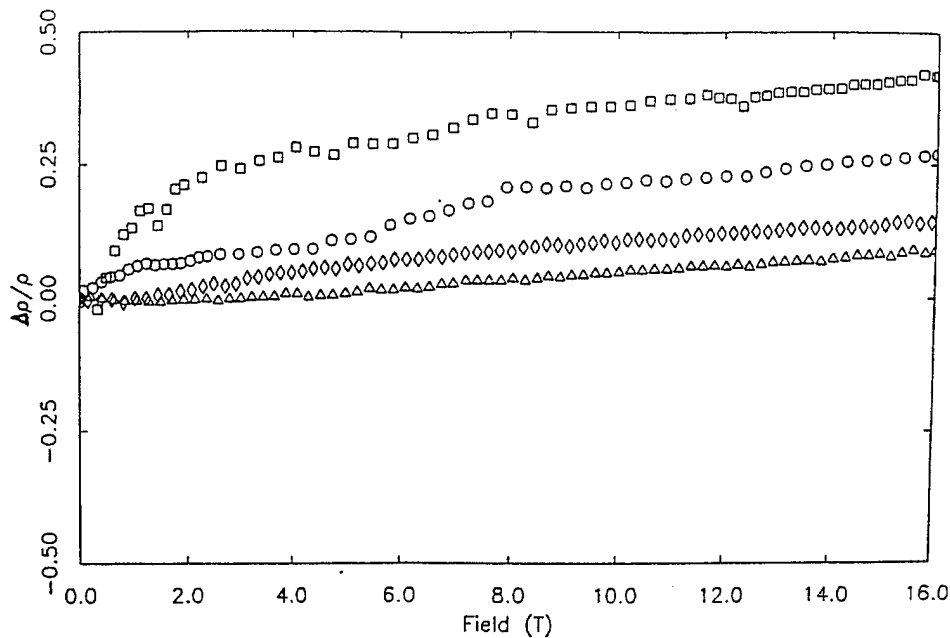


Fig. 2.33 Magnetoresistance for PANI-CSA in the metallic regime at 20 mK (□), 70 mK (○), 370 mK (◊), and 500 mK (△). (From Ref. 151.)

axis in an aligned sample:

$$\sigma_{\text{int}} = Ne^2\tau/m = (Ne^2/\hbar k_F)l_{\text{in}} \quad (14)$$

where N is the density of carriers and k_F is the Fermi wave number in the chain direction. Using $N \approx 2.5 \times 10^{21} \text{ cm}^{-3}$ and $k_F \approx \pi/2c$, where $c \approx 7 \text{ \AA}$ [153,154], one obtains $\sigma_{\text{int}} \approx 2.5 \times 10^4 \text{ S/cm}$. In an unoriented sample, the measured value would be reduced by the anisotropy. An alternative estimate can be obtained from the observed increase in resistivity in the region of the positive temperature coefficient; $\Delta\rho \sim 3 \times 10^{-4} \Omega\cdot\text{cm}$. This would imply $\sigma_{\text{int}} \sim 3 \times 10^3 \text{ S/cm}$ for a nonoriented sample; since the anisotropy would be expected to reduce the value in a nonoriented sample by about a factor of 10–100, the estimated value for $\sigma_{\parallel}(300 \text{ K})$ would be in excess of $3 \times 10^4 \text{ S/cm}$. We conclude that for chain-oriented and chain-aligned PANI, the intrinsic conductivity along the chain axis at room temperature should be significantly greater than 10^4 S/cm .

The metallic nature of PANI-CSA has been confirmed from the temperature-independent Pauli susceptibility [27–30,155], the observation of modified Korringa relation from $^{13}\text{C-NMR}$ [156], large negative dielectric constant at 8–12 GHz [149,150], and the observation of plasma edge in infrared reflectivity measurements [157–158]. The microscopic spin dynamics in previous generation PANI (PANI-HCl) indicated that the intra/interchain spin diffusion rates are highly anisotropic and suggested that doped PANI should be considered a highly one-dimensional system [161–166]. This is

in contrast to PANI-CSA, in which the electronic states are delocalized in three dimensions.

d. Summary

For metallic PANI-CSA, the conductivity at 20 mK is approximately 30 S/cm, the positive TCR extends from 300 to 150 K, and $\rho_r < 2$. In this metallic regime, the $T^{1/2}$ dependence at low temperatures points to the importance of e–e interactions. The magnitude of the inelastic scattering time, $\tau_{\text{in}} \approx 10^{-10} \text{ s}$, is typical of that of amorphous metals. The intrinsic conductivity of PANI-CSA along the chain axis is estimated to be significantly greater than 10^4 S/cm at room temperature. The magnetic and optical properties also indicate that PANI-CSA is a disordered metal.

5. PPy-PF₆

a. Temperature Dependence of the Conductivity

The room temperature conductivity for films grown by electropolymerization at -40°C is $\sigma_{\text{RT}} = 150–400 \text{ S/cm}$ [25,26,167]. Films prepared at room temperature are less conducting [$\sigma_{\text{RT}} = 10–100 \text{ S/cm}$], and the temperature dependence of the resistivity is rather strong, typical of that of an insulator. Thus, one can vary the disorder by changing the polymerization temperature. The temperature dependence of normalized resistivity for various PPy-PF₆ samples is shown in Fig. 2.34. For samples with higher conductivity, $\sigma_{\text{RT}} > 150 \text{ S/cm}$

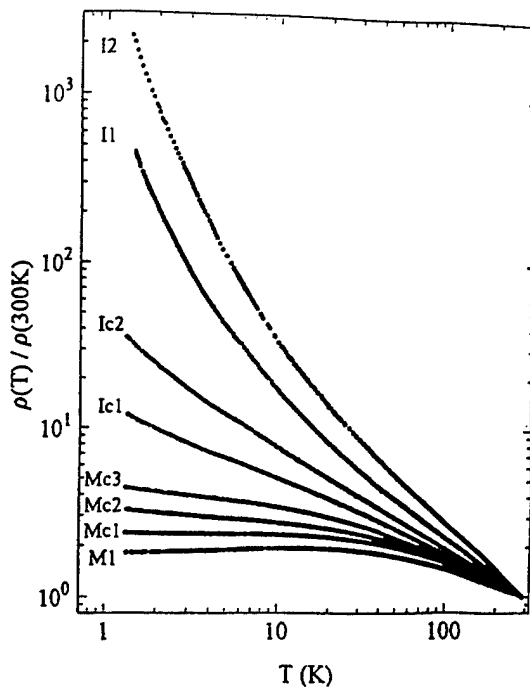


Fig. 2.34 Log-log plot of normalized $\rho(T)$ vs. T of PPy-PF₆ samples. (M = metallic regime, Mc = metallic side of critical regime, Ic = insulating side of critical regime, and I = insulating regime.) The values of $\sigma(300\text{ K})$ and resistivity ratios (ρ_r) are listed in Tables 2.3 and 2.4.

(samples denoted by M), the resistivity decreases at low temperatures; there is a resistivity maximum around $T = 7\text{--}20\text{ K}$.

Again, for PPy-PF₆ the disorder can be characterized by ρ_r [167]:

1. For samples on the metallic side of the critical regime ($2 < \rho_r < 10$), $\sigma(0)$ is finite but TCR remains negative at all temperatures (denoted as Mc samples).
2. For samples in the metallic regime ($\rho_r < 2$), the TCR is positive at low temperatures with a con-

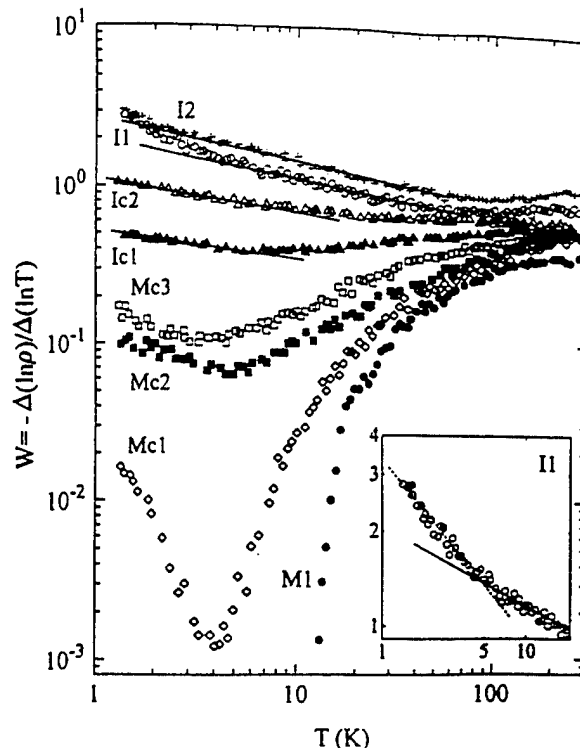


Fig. 2.35 W vs. T plot of the same samples as in Fig. 2.34. The inset shows data for sample I1 below 20 K.

ductivity minimum at $T = T_m$ (denoted as M samples).

Although the existence of finite $\sigma(0)$ defines the boundary of the metallic regime in PPy-PF₆ ($6 < \rho_r < 10$), the sign of the TCR changes at $\rho_r \approx 2$. The power law dependence, $\rho(T) = T^{-\beta}$, is observed at high temperatures ($T > 100\text{ K}$). The various parameters obtained from the data are listed in Tables 2.3 and 2.4 [167].

The $\rho(T)$ plots for various PPy-PF₆ samples demonstrate once again that such plots alone (Fig. 2.34) are not sufficient to identify the M-I transition. On the other

Table 2.3 Experimental Values and Parameters for PPy-PF₆ Samples in the Insulating Regime

Sample	$\sigma(300\text{ K})$ (S/cm)	ρ_r^a	$\Delta\rho/\rho^b$	x^c	T_{Mott} (K) ^d	L_c (Å)
Ic1	114	11.6	0.40	0.19 ± 0.03 ($T < 4\text{ K}$)	20	269
Ic2	103	35.8	0.51	0.24 ± 0.02 ($T < 5\text{ K}$)	290	177
I1	52	527	—	0.24 ± 0.02 ($T > 5\text{ K}$)	3,700	—
I2	34.4	2590	1.78	0.29 ± 0.03 ($T > 2\text{ K}$)	17,500	86

^a $\rho_r = \rho(1.4\text{ K})/\rho(300\text{ K})$.

^b Data at $H = 8\text{ T}$ and at $T = 1.4\text{ K}$.

^c Results from data using Eq. (4).

^d Values are obtained assuming $x = 0.25$.

Table 2.4 Experimental Values and Parameters for PPy-PF₆ Samples in the Metallic Regime

Sample	Pressure	$\sigma(300\text{ K})$ (S/cm)	ρ_r^a	$\Delta\rho/\rho^b$	m [S/(cm·K ^{1/2})]	m' [S/(cm·K ^{1/2})]	$\sigma(0)^c$ (S/cm)	L_c (Å) ^d	T_m (K)
M1	Ambient	338	1.75	0.12	-7.55	+7.80	201	12.1	12
M2	Ambient	298	1.97	0.13	-3.19	+8.34	155	15.7	7.5
M2	9 kbar	330	1.33	0.05	-8.83	+0.86	261	9.3	24
Mc1	Ambient	271	2.40	0.16	+1.75	+11.6	108	22.5	—
Mc2	Ambient	313	3.22	0.21	+12.9	+25.9	82	29.4	—
Mc2	4 kbar	358	1.81	0.12	-3.98	+10.2	191	12.7	12
Mc2	10 kbar	377	1.54	0.10	-9.13	+6.22	247	9.8	19
Mc3	Ambient	192	4.45	0.23	+8.00	+12.9	34	70.9	—
Ic1	4 kbar	133	2.64	0.18	+2.05	+6.83	46	52.6	—
Ic2	10 kbar	137	2.08	0.15	-0.20	+5.11	64	37.8	—

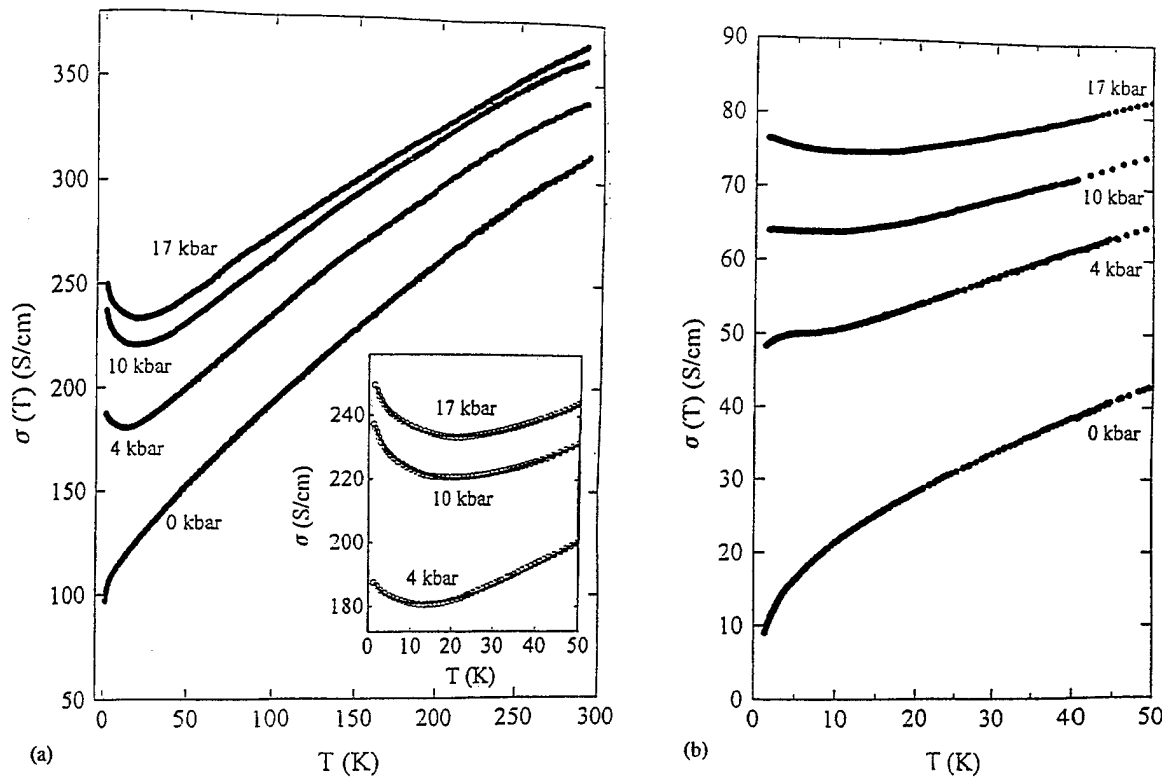
^a $\rho_r = \rho(1.4\text{ K})/\rho(300\text{ K})$.^b Data at $H = 8\text{ T}$ and at $T = 1.4\text{ K}$.^c Extrapolated values from $T^{1/2}$ dependence of the conductivity.^d Calculated from the relation $\sigma(0) = 0.1e^2/hL_c$.

Fig. 2.36 (a) $\sigma(T)$ for PPy-PF₆ sample Mc2 ($\rho_r = 3.2$) under pressure. The inset shows the same data below $T = 50\text{ K}$. Solid lines in the inset are fitted curves using $\sigma(T) = \sigma(0) + mT^{1/2} + BT^{p/2}$, where $p = 2.50 \pm 0.04$ and $B = 0.4 \pm 0.01$. Note that $\sigma(0)$ and m depend on pressure. (b) The temperature dependence of the conductivity ($T < 50\text{ K}$) of the sample Ic1 ($\rho_r = 12$) under pressure.

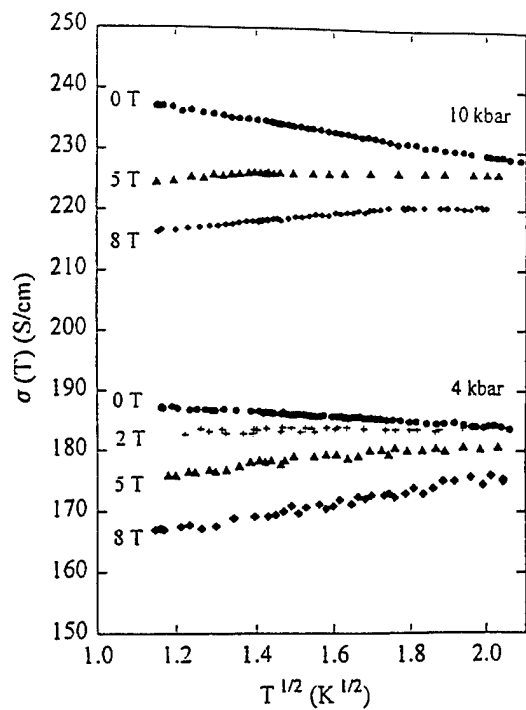


Fig. 2.37 $\sigma(T)$ at low temperature ($1.3 \text{ K} < T < 4 \text{ K}$) for PPy-PF₆ sample Mc2 under $P = 4 \text{ kbar}$ ($\rho_r = 1.81$) and 10 kbar ($\rho_r = 1.54$) in various magnetic fields ($H = 0, 2, 5$, and 8 T).

hand, the W vs. T plot in Fig. 2.35 (the same data as in Fig. 2.34) brings out the subtle variations in the temperature dependence of the resistivity with clarity and precisely defines the M-I transition. For samples on the metallic side of the M-I transition, the temperature coefficient of W is positive at high temperatures, whereas for samples on the insulating side, the temperature coefficient of W is negative.

Since the coefficient m in Eq. (8a) can have either sign depending on the competition between the Hartree and exchange contributions, the positive TCR for samples in the metallic regime (sample M; $\rho_r < 2$) and negative TCR close to the transition (sample Mc; $2 < \rho_r < 5$) are thought to be associated with a breakdown of the Thomas-Fermi screening near the M-I transition [137,138]. The tuning of the temperature dependence of conductivity by pressure on either side of the M-I transition is shown in Figs. 2.36a and 2.36b.

In the metallic regime, the $\sigma(T)$ follows Eq. (7) as shown in the inset of Fig. 2.36a. Since the conductivity of metallic PPy-PF₆ at 1.3 K is typically $100\text{--}300 \text{ S/cm}$, correlation effects are expected to play a major role in the low temperature transport. The $\sigma(T) \sim T^{1/2}$ dependence at low temperatures, shown in Fig. 2.37, indicates a significant contribution from e-e interactions. The temperature and field dependence of the conductivity of metallic PPy-PF₆ at millikelvin temperatures (75 mK to 1 K) are shown in Fig. 2.38 [151]. As in PANI-CSA, the high conductivity ($150\text{--}200 \text{ S/cm}$) at 20 mK and 14 T field indicates robust three-dimensional transport and the absence of one-dimensional localization.

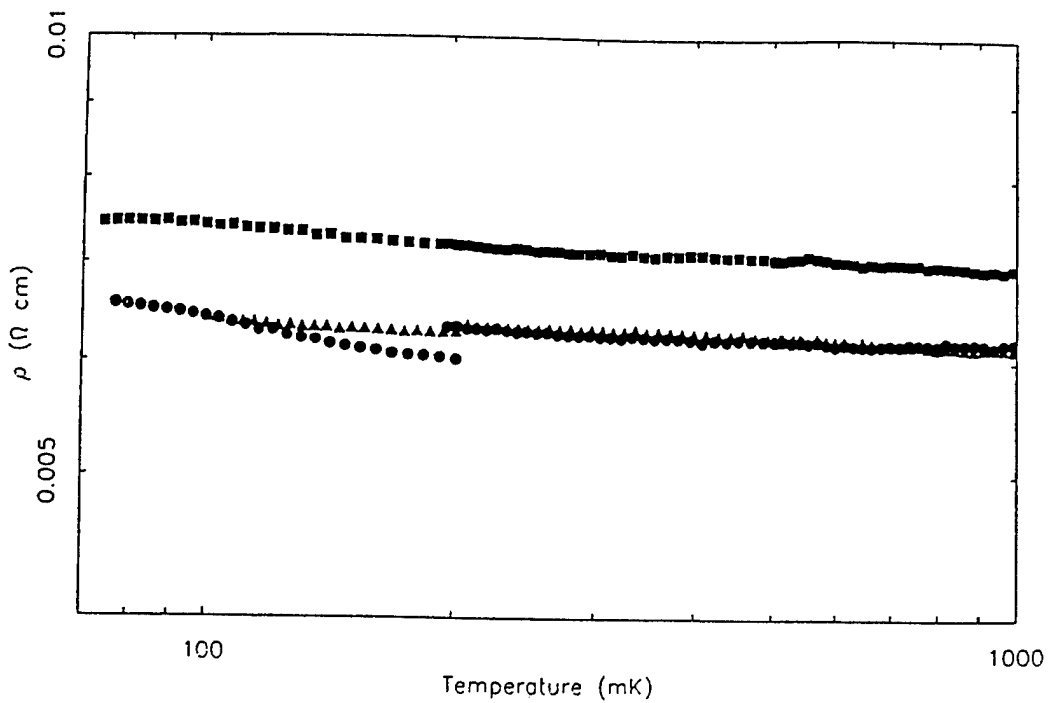


Fig. 2.38 $\rho(T)$ vs. T for PPy-PF₆ sample M1 at $H = 0$ (●), 2 T (▲), and 8 T (■) at millikelvin temperatures.

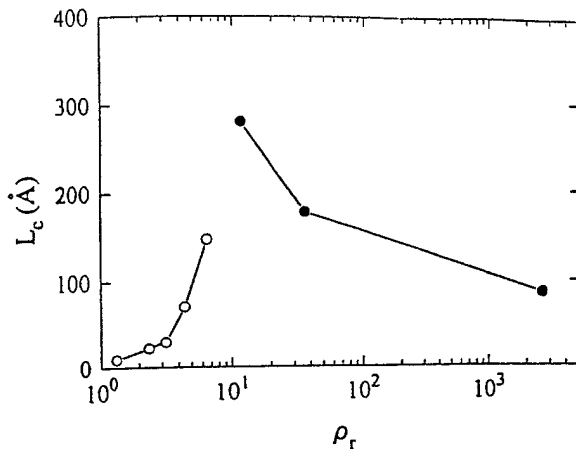


Fig. 2.39 The correlation length (L_c) obtained both from the insulating (●) and metallic (○) regimes plotted as a function of ρ_r for PPy-PF₆ samples. L_c is expected to diverge at the M-I transition near $\rho_r = 10$.

According to the scaling theory of localization, the correlation length L_c is expected to diverge at the M-I transition. The correlation length as a function of ρ_r is shown for PPy-PF₆ in Fig. 2.39. The L_c values from the metallic regime were obtained from $\sigma(0)$, using the relation $\sigma(0) = (0.1e^2/\hbar L_c)$; those from the insulating regime were obtained from analysis of the magnetoresistance (see following section). The maximum in L_c at $\rho_r \sim 10$ indicates the transition, consistent with the transport data, which show the power law (indicative of the critical regime) over the widest temperature range at $\rho_r \approx 10$.

b. Magnetoconductance

The low and high field MC for various PPy-PF₆ samples near the M-I transition, at $T = 1.4$ K, are shown in Figs. 2.40a and 2.40b. The H^2 and $H^{1/2}$ dependence at low and high fields, respectively, are in agreement with the localization-interaction model as expressed in Eqs. (11)–(13). The MC in Fig. 2.40b is normalized to $\alpha\gamma F_\sigma$. The dashed line in Fig. 2.40b is the field dependence expected from Eq. (11) at 1.4 K. As ρ_r increases, however, the slope deviates from the theoretical value. This can be interpreted as due to the localization contribution, but the origin of negative MC is not yet fully understood. According to the theory of weak localization, the quantum interference between time-reversed backscattering paths is destructive when the spin-orbit scattering is strong, leading to the negative MC [44,45]. This contribution has been experimentally observed in disordered metal films and *p*-type doped semiconductors. However, as noted above, one does not expect strong spin-orbit effects in conducting polymers that are made up of atoms of relatively low atomic number.

The temperature dependence of inelastic scattering

length (l_{in}) is shown in Fig. 2.41; the data indicate that $\tau_{in} \propto l_{in}^2 \propto T^{-p}$ with $p = 1.02 \pm 0.05$, consistent with inelastic scattering due to the Coulomb interaction close to the M-I transition [132,134]. For samples in the metallic regime ($\rho_r < 3$), we estimate that $l_{in} \sim 200$ –300 Å and that it is nearly temperature-independent. In this regime, D (diffusion coefficient) ≈ 0.02 –0.04 cm²/s, and the interaction length $L_T = (\hbar D/k_B T)^{1/2} \approx 30$ –40 Å ($T = 1.4$ K), i.e., much smaller than the inelastic scattering length. As the disorder increases, the system moves toward the critical regime, and the Coulomb interaction is less well screened, thereby decreasing the inelastic electron-electron scattering length. Hence the contribution due to the localization increases with ρ_r .

The MC at millikelvin temperatures is shown for metallic PPy-PF₆ in Fig. 2.42 [151]. The MC is positive below 300 mK. The crossover from negative to positive MC as the temperature is lowered below 1 K indicates

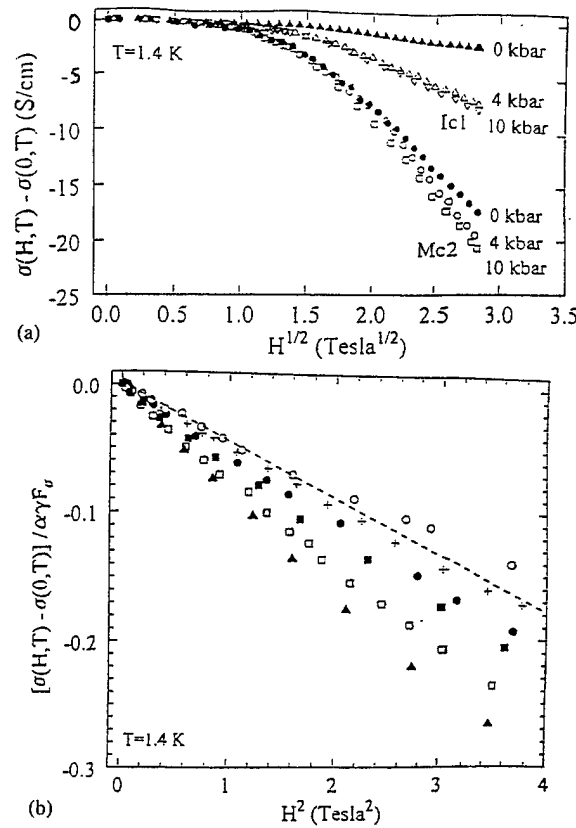


Fig. 2.40 (a) High field magnetoconductance of PPy-PF₆ samples plotted as a function of $H^{1/2}$ at $T = 1.4$ K and at $P = 4$ kbar and 10 kbar. (b) The low field magnetoconductance normalized by $\alpha\gamma F_\sigma$ plotted as a function of H^2 for sample M2 at $P = 9$ kbar (○), $\rho_r = 1.33$; Mc2 at $P = 10$ kbar (+), $\rho_r = 1.54$; M2 (●), $\rho_r = 1.97$; Mc2 (■), $\rho_r = 3.2$; Mc3 (■), $\rho_r = 4.5$ and Ic1 (▲), $\rho_r = 12$. The dashed line is the theoretical estimate [44,45].

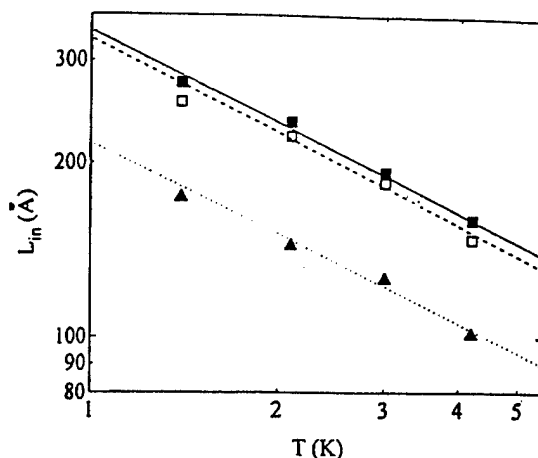


Fig. 2.41 Log-log plots of the inelastic scattering length (l_{in}) vs. T for PPy-PF₆ samples Mc2 (■), $\rho_r = 3.2$; Mc3 (□), $\rho_r = 4.5$; and Ic1 (▲), $\rho_r = 12$.

the competition between the weak localization and e-e interaction contributions to the MC. The enhanced negative contribution below 300 mK at fields above 8 T indicates the dominance of the e-e contribution at higher fields, as expected in the localization-interaction model. However, more work is necessary to quantify the scattering parameters below 1 K.

c. Summary

As for the other conducting polymers, ρ_r can be used to quantify the disorder; as the disorder decreases in PPy-PF₆, ρ_r decreases systematically, with the M-I transition at $\rho_r \approx 10$. The resistivity at high temperatures follows the power law temperature dependence with the power law exponent β decreasing from 1 to 0.3 as ρ_r decreases. As the system approaches the transition from the metallic regime ($\rho_r \sim 1-6$):

1. $\sigma(0)$ decreases continuously, and the correlation length increases.
2. The screening length increases (γF_σ decreases), and the effect of the electron-electron interaction increases.
3. The sign of TCR changes from positive to negative (at $\rho_r = 2$).
4. The temperature (T_m) of the conductivity minimum decreases with ρ_r (for $\rho_r < 2$).
5. The inelastic scattering at $T > T_m$ is due to the electron-phonon interaction ($p = 2.5$).
6. The inelastic diffusion length decreases, and the contribution due to localization increases near the M-I transition.

In metallic PPy-PF₆, the crossover from negative to positive MC below 300 mK, and the finite conductivity ($\sim 100-200$ S/cm) at 20 mK results from the interplay of the weak localization and e-e interaction contributions.

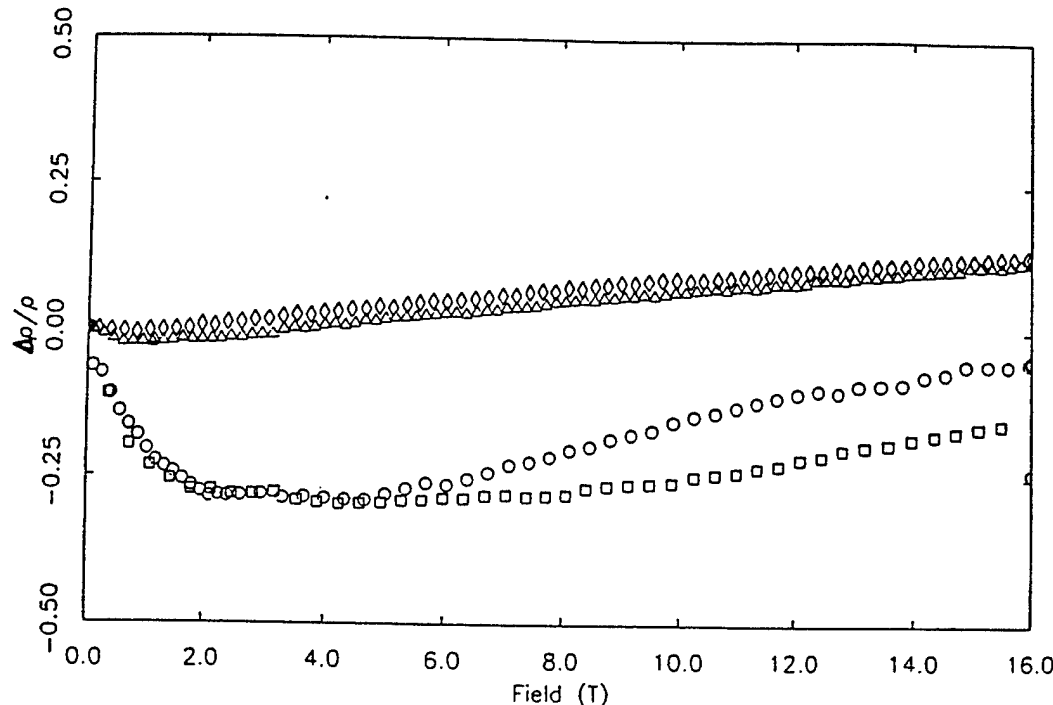


Fig. 2.42 Magnetoresistance ($\Delta\rho/\rho$) vs. H for PPy-PF₆ sample M1 at 20 mK (□), 70 mK (○), 370 mK (Δ), 500 mK (◊). (From Ref. 151.)

6. Far-Infrared Response of PANI-CSA and PPy-PF₆

The microwave and far-infrared dielectric response in metallic conducting polymers is typical of the usual metals [149]; the dielectric function is negative for frequencies below the plasma frequency. However, disorder and localization play an important role. Studies of the frequency response and the charge dynamics in metallic conducting polymers are in the preliminary stages of investigation. Lee et al. [157–160] observed that the infrared optical response of metallic PANI-CSA and PPy-PF₆ are consistent with the theory of disordered metals; the frequency-dependent optical conductivity and dielectric functions are in excellent agreement with the “localization-modified Drude model.” Moreover, the value of $k_F\lambda$ estimated from the localization-modified Drude model is consistent with that obtained from transport measurements. Disorder tends to decrease $\sigma(\omega)$ and drive $\epsilon(\omega) > 0$ as $\omega \rightarrow 0$; thus, on the insulating side of the M-I transition, $\epsilon(\omega) > 0$ even in the far-infrared.

Kohlman et al. [168] and Epstein et al. [65–69] proposed a “metallic islands” model with separate contributions from crystalline and amorphous phases. They observed $\epsilon(\omega) < 0$ in the microwave regime and analyzed their data in terms of having two different plasma frequencies for the localized and delocalized electrons, respectively. Their data analysis [65–69,168] yielded $\lambda \sim 1$ –100 μm and $k_F\lambda \sim 10^5$, neither of which is consistent with the dc transport properties. Thus, the “metallic islands” model is unable to provide a quantitative description of the data with acceptable parameters.

7. Polyparaphenylenevinylene (PPV)

Although PPV is well known as the most widely used conducting polymer for light-emitting diodes [169], transport measurements on heavily doped PPV are rather few. The room temperature conductivity along the chain axis of H₂SO₄-doped PPV (PPV-HSO₄) is nearly 10⁴ S/cm [24]. Preliminary transport measurements [170] indicate that highly doped PPV-HSO₄ samples are metallic ($k_F\lambda > 1$) with $\sigma(T)$ nearly temperature-independent ($\rho_r < 1.3$). Madsen et al. [99] reported $\sigma(T)$ for oriented PPV-AsF₅; anisotropies of 165 and 250 were found at 300 and 4 K, respectively. Park et al. [171] also observed the low temperature increase in anisotropy in doped PPV samples, unlike the temperature-independent anisotropy of doped oriented (CH)_x. For PPV-AsF₅ samples [99] having somewhat lower conductivity, $\sigma_{RT} \approx 2300$ S/cm, the temperature dependence is rather weak; $\rho_r \approx 1.28$, and the temperature dependences parallel and perpendicular to the chain axis are nearly identical, similar to those observed in doped oriented (CH)_x. Although a positive TCR [99] has been observed below 6 K for PPV-AsF₅ samples with a relatively weak temperature dependence ($\rho_r < 1.8$), this has not been rigor-

ously verified as in PPy-PF₆. The $T^{1/2}$ dependence of the conductivity due to contributions from e–e interactions at low temperatures has been reported for heavily doped and highly conducting samples [99]. Thus, it seems that high quality PPV-AsF₅ samples are in the metallic regime. Work is in progress to fully characterize the M-I transition in doped PPV [170].

E. Transport in the Insulating Regime Near the M-I Transition

1. Introduction

As in the critical and metallic regimes, the extent of disorder can be characterized in terms of the resistivity ratio [120]. The approximate ρ_r values for the insulating regime are the following [172]:

1. For unoriented I-(CH)_x with $\sigma(300 \text{ K}) < 500 \text{ S/cm}$, $\rho_r > 50$.
2. For oriented I-(CH)_x with $\sigma(300 \text{ K}) < 3000 \text{ S/cm}$, $\rho_r > 15$.
3. For oriented K-(CH)_x with $\sigma(300 \text{ K}) < 4000 \text{ S/cm}$, $\rho_r > 25$.
4. For nonoriented PPy-PF₆ with $\sigma(300 \text{ K}) < 100 \text{ S/cm}$, $\rho_r > 10$.
5. For nonoriented PANI-CSA with $\sigma(300 \text{ K}) \approx 150$ –250 S/cm, $\rho_r > 4$.
6. For nonoriented I-P3HT with $\sigma(300 \text{ K}) < 500 \text{ S/cm}$, $\rho_r > 45$.

Evidence of Mott VRH conduction [42,43] in three dimensions has been reported extensively in the literature on doped conducting polymers [75]. Deviations from the $\ln \rho \propto (T_0/T)^{1/4}$ law have also been reported; $\ln \rho \propto (T_0/T)^{1/3}$ was observed in doped polyhexylthiophene [173] and in polyacetylene doped to intermediate levels [174], where the effect of the nearest-neighbor hopping due to the finite conjugation length was suggested as the origin [106,107]. Recently, $\ln \rho \propto (T_0/T)^{1/2}$ behavior was reported for protonated polyaniline [65–69] and doped polypyrrole [117–119]. However, the strong temperature dependence ($\rho_r > 10^5$) and the nonlinear (with T) temperature dependence of the thermoelectric power indicate that such samples are deep in the insulating regime. In such samples, the extensive disorder and the formation of inhomogeneous “metallic islands” dominate the transport. The importance of homogeneity versus inhomogeneity has been demonstrated by the systematic increase in the VRH exponent from 1/4 to 1 with dilution toward the percolation threshold in PANI-CSA blends. The observation of $\ln \rho \propto (T_0/T)^{1/2}$ below the percolation threshold [175] demonstrates clearly the crossover from “homogeneous” to “granular” behavior and demonstrates that the transport can be strongly influenced by microstructure and morphology (see following section).

2. Theory

In the insulating regime, transport occurs through variable-range hopping among localized states as described by Mott [42,43] for noninteracting carriers and by Castner [78], Efros and Shklovskii [122] when the Coulomb interaction between the electron and the hole left behind is dominant. For Mott VRH conduction in three dimensions,

$$\ln \rho \propto (T_0/T)^{1/4} \quad (15a)$$

$$T_0 = 18/k_B L_c^3 N(E_F) \quad (15b)$$

where k_B is the Boltzmann constant, L_c is the localization length, and $N(E_F)$ is the density of states at Fermi level. In the Efros-Shklovskii (ES) limit,

$$\ln \rho \propto (T_0'/T)^{1/2} \quad (16a)$$

$$T_0' = \beta_1 e^2 / \epsilon k_B L_c \quad (16b)$$

where e is the electron charge, ϵ is the dielectric constant, and $\beta_1 = 2.8$ (a numerical constant).

Measurements of $\sigma(T)$ for PPy-PF₆, PANI-CSA, and the PATs [172] show that samples in the insulating regime, but near the critical regime, follow Mott's VRH conduction down to 1 K. Samples farther into the insulating regime, with $\rho_r = 10^2-10^3$, exhibit a crossover from Mott to ES hopping VRH conduction at $T_{\text{cross}} = 2-10$ K. The VRH parameters in Eqs. (15) and (16) have been determined from the temperature and magnetic field dependence of the resistivity. The results are consistent with strong localization theory and the expected effect of the Coulomb interaction near the disorder-induced M-I transition [78,122]. The experiments have also shown that Eq. (16) holds in a strong magnetic field ($H = 8$ T) where $T_0(H)/T_0(0) \propto H^p$ with $p = 1.0-1.2$.

The crossover from Eq. (15) to Eq. (16) occurs when the mean hopping energies (Δ_{hop}) in the Mott and ES limits are comparable [78,176-178]. The mean hopping energy from each theory is given by

$$\Delta_{\text{hop}} = (1/4) (k_B T) (T_0/T)^{1/4} \quad (\text{Mott, } x = 1/4) \quad (17a)$$

$$\Delta'_{\text{hop}} = (1/2) (k_B T) (T_0'/T)^{1/2} \quad (\text{ES, } x = 1/2) \quad (17b)$$

The Efros-Shklovskii VRH theory [78,122] predicts a power law energy dependence in the density of states near the Fermi level that occurs within the Coulomb gap, Δ_C :

$$\Delta_C = e^3 N(E_F)^{1/2} / \epsilon^{3/2} \quad (18)$$

where $N(E_F)$ is the unperturbed density of states at the Fermi level (i.e., in the absence of the Coulomb gap) and ϵ is the dielectric constant. Castner [78] pointed out that near the M-I transition the dielectric constant can be expressed as

$$\epsilon = \epsilon_\infty + 4\pi e^2 N(E_F) L_c^2 \quad (19)$$

where ϵ_∞ is the core dielectric constant and the second term results from the polarizability of the localized states. Note that L_c diverges as $\delta \rightarrow 0$. Thus, if the system is not too far from the M-I transition, then the second term is dominant, and $\epsilon \approx 4\pi e^2 N(E_F) L_c^2$. Assuming that the above approximation is valid, Castner [78] and Rosenbaum [176] have noted the following relations:

$$T_0/T_0' = 18(4\pi)/\beta_1 = 81 \quad (20)$$

$$\Delta_C \approx k_B T_0/18(4\pi)^{3/2} \approx k_B T_0/\beta_1(4\pi)^{1/2} \quad (21)$$

$$T_{\text{cross}} = 16(T_0')^2/T_0 \quad (\text{if } \Delta_{\text{hop}} \approx \Delta'_{\text{hop}}) \quad (22)$$

The localization length can be estimated from the expression for the weak magnetic field dependence of the VRH resistivity [122,179]:

$$\ln[\rho(H)/\rho(0)] = t(L_c/L_H)^4 (T_0/T)^{3x} \quad (23)$$

where $t = 0.0015$ for $x = 1/4$, $t = 0.0035$ for $x = 1/2$, and $L_H = (c\hbar/eH)^{1/2}$ is the magnetic length [122,179].

The following method was used for testing Castner's equations:

1. First, the values of T_0 and T_0' are obtained as accurately as possible by using Eqs. (4) and (5) and the W vs. T plots.
2. The value of L_c is determined from the slope of plots of $\ln[\rho(H)/\rho(0)]$ vs. H^2 by using Eq. (23) and the known value of T_0 or T_0' .
3. The values of $N(E_F)$ in the Mott regime can be determined by using Eq. (15b), and the values of ϵ in the ES regime can be obtained by using Eq. (16b) and the known values of T_0 (assuming that $\beta_1 = 2.8$).
4. The ratio of the experimental values of T_0 and T_0' can be used to check the validity of Eqs. (20)-(22).
5. By using the values of T_0 and T_0' , it is possible to compare the theoretical value of T_{cross} with that obtained from the W vs. T plot, as shown in Tables 2.5 and 2.6.
6. Finally, the deviation of $4\pi e^2 N(E_F) L_c^2 / \epsilon$ from unity is checked to identify the samples that satisfy Castner's approximation.

All the above parameters, as obtained from experiment and from theory, are listed in Tables 2.5 and 2.6 (including T_{cross} and ϵ).

The experimental ratio $T_0/T_0' = 85-115$ is close to the value predicted by Castner [78], and $\Delta_C = 0.3-0.6$ meV. The experimental values of T_{cross} are in good agreement with those estimated from the theory as shown in Tables 2.5 and 2.6. In the crossover regime ($\rho_r = 2 \times 10^2-2 \times 10^3$), $N(E_F) = (3-4 \times 10^{19} \text{ states}/(\text{eV} \cdot \text{cm}^3))$. We have tested the validity of the approximation $\epsilon \approx 4\pi e^2 N(E_F) L_c^2$; we find $4\pi e^2 N(E_F) L_c^2 / \epsilon = 0.70-0.95$, indicating that ϵ_∞ makes a relatively small contribution to ϵ . However, this approximation is not valid for the highly disordered sample (PPy-PF₆, $\rho_r = 2180$), which shows

Table 2.5 Experimental Values and Variable Range Hopping Parameters for PPy-PF₆ Samples

Symbol Fig. 2.43	$\sigma(300\text{ K})$ (S/cm)	ρ_r	T_0 (K)	T'_0 (K)	T_0/T'_0	$T_{\text{cross}}^{(\text{exp})}$ (K)	$T_{\text{cross}}^{(\text{th})}$ (K)	L_c (Å)	$N(E_F)$ [$\times 10^{19}$ states (eV \cdot cm 3)]	$4\pi^2 N(E_F) L_c^2 / \epsilon$
△	16.1	$>10^4$	1.30×10^5							
○	28.9	6190	3.06×10^4					88		
■	34.8	2180	1.05×10^4	5.63×10^1	187	4.8	4.8	108	1.6	0.43
◆	40.4	822	4.34×10^3	4.53×10^1	95	6.5	7.5	110	3.6	0.84
●	57.0	734	3.91×10^3	4.27×10^1	91	6.1	7.5	111	3.9	0.88
▲	83.4	576	3.34×10^3	2.91×10^1	115	5.4	4.1	123	3.3	0.7
+	92.8	107	1.01×10^3					118	22.4	

a relatively low crossover temperature in spite of its high T_0 and T'_0 .

For samples farther into the insulating regime ($\rho_r > 10^3$), two different kinds of materials are known, homogeneous and inhomogeneous [172]:

By "homogeneous," we mean materials in which the localization length is greater than the disorder length scale, e.g., greater than the structural coherence length (ξ) in a polymer that has both crystalline and amorphous regions ($L_c \geq \xi$). Mott VRH conduction is recovered at low temperatures for more disordered, but relatively homogeneous, samples. In such materials, the thermoelectric power is linear with temperature and the magnitude of thermoelectric power increases slightly with ρ_r .

By "inhomogeneous" we mean inhomogeneous doping, phase segregation of doped and undoped regions, partial dedoping, and large-scale morphological disorder, etc. ($L_c \leq \xi$). Such materials are like granular metals where $\ln \rho \propto (T'_0/T)^{1/2}$ is well established [175,180,181]. Although the factors leading to the fit for granular metals are not completely understood, recent theoretical work by Cuevas et al. [181] has shown that the low temperature transport properties can be dominated by the long-range Coulomb interaction rather than by

charging effects (as previously believed). In this inhomogeneous limit, hopping contributions to the temperature dependence of thermoelectric power are substantial, as shown below.

Ovchinnikov and Pronin [182,183] proposed a quasi-one-dimensional percolation model for explaining the conductivity of doped conducting polymers in the insulating regime. In this model an impurity (e.g., acceptor) captures an electron from one of the adjacent chains and forms a charged impurity center. Such a carrier can detrap by an activated process and diffuse along the chain. This polaron can recombine with another impurity center near the chain and then escape to an arbitrary chain adjacent to the second impurity center. Thus, conduction by percolation is possible in such a system if an infinite cluster of chains can be connected by impurity centers.

3. Polypyrrole

The resistivity ratio of electrochemically polymerized PPy-PF₆ varies over the relatively wide range from $\rho_r = 1.7$ to $\rho_r > 10^5$ depending on details of the polymerization conditions, as shown in Fig. 2.35 [167]. The M-I transition occurs at $\rho_r \sim 10$; the system becomes metallic for $\rho_r < 10$ (with finite zero temperature conductivity) and becomes an insulator for $\rho_r > 10$ [with $\rho(T)$ following

Table 2.6 Experimental Values and the Variable Range Hopping Parameters for Iodine-Doped PAT Samples

Symbol (Fig. 2.46)	$\sigma(300\text{ K})$ (S/cm)	ρ_r	T_0 (K)	T'_0 (K)	T_0/T'_0	$T_{\text{cross}}^{(\text{exp})}$ (K)	$T_{\text{cross}}^{(\text{th})}$ (K)	L_c (Å)	$N(E_F)$ [$\times 10^{19}$ states (eV \cdot cm 3)]	$4\pi^2 N(E_F) L_c^2 / \epsilon$
PBT	450	219	3.61×10^3	3.48×10^1	104	6.5	5.4	140	2.1	0.78
PHT-1	▲	1,170	45.1	7.60×10^2				129	12.7	
PHT-2	△	194	908	4.92×10^3	5.18×10^1	95	8.0	8.7	121	2.4
POT-1	●	502	244	3.29×10^3	2.88×10^1	114	5.5	4.0	149	1.9
POT-2	○	168	1,640	5.67×10^3	6.69×10^1	85	9.8	12.6	114	2.5
PDT	◊	710	47.3	7.97×10^2				132	11.3	
PDDT		489	250	3.38×10^3	3.82×10^1	112	6.8	6.9	147	1.9
PTDT	+	167	$>10^6$		4.33×10^2					0.71

Eq. (15) or (16) at low temperature]. For films grown at room temperature, the electrical conductivity at 300 K is typically $\sigma(300 \text{ K}) = 10\text{--}100 \text{ S/cm}$ with $10^2 < \rho_r < 10^5$.

The temperature dependence of the resistivity is shown in Figs. 2.43a and 2.43b as plots of $\ln \rho$ vs. $T^{-1/4}$ and $T^{-1/2}$, respectively. The sample with $\rho_r = 107$ (close to the critical regime) shows a linear dependence of $\ln \rho$ on $T^{-1/4}$ below $T = 15 \text{ K}$, characteristic of Mott's VRH conduction. Samples with $\rho_r \sim 2 \times 10^2\text{--}2 \times 10^3$ exhibit linear $\ln \rho$ vs. $T^{-1/4}$ for $10 \text{ K} < T < 40 \text{ K}$ but show a clear deviation from linearity for $T < 10 \text{ K}$. Below 10 K, the $\ln \rho(T)$ data follow a $T^{-1/2}$ dependence as shown in Fig. 2.43b. Thus, the data indicate a crossover from Mott to ES VRH conduction. This crossover is confirmed by the W vs. T plots shown in Fig. 2.44, from which the crossover temperature (T_{cross}) is accurately determined. The VRH parameters, T_0 in Eq. (15) and T'_0 in Eq. (16), are determined from the slopes in Fig. 2.44. Samples with $\rho_r > 5 \times 10^3$ again show Mott's $T^{-1/4}$ behavior below 100 K down to the lowest measured temperature. The various parameters obtained from analysis of the data in terms of Eqs. (15) and (16) are listed in Table 2.5. The ratio $T_0/T'_0 = 85\text{--}115$, as determined from the data, is close to that predicted using Castner's approximation.

The plot of $\ln [\rho(H)/\rho(0)]$ vs. H^2 at $T = 1.4 \text{ K}$ is shown in Fig. 2.45. The magnetoresistance is positive as expected for VRH conduction; the data are linear in H^2 up to $H = 1\text{--}2 \text{ T}$, showing a slight deviation from quadratic dependence at higher fields. Using Eq. (23), we obtain $L_c = 110\text{--}150 \text{ \AA}$ from the slopes of the straight

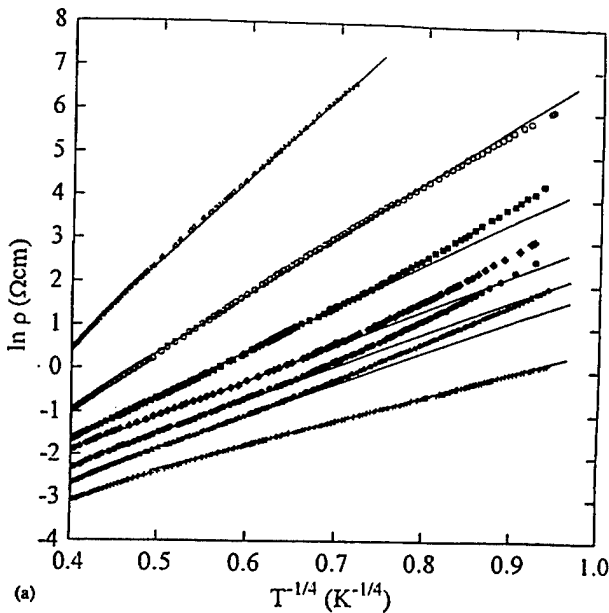


Fig. 2.43 (a) Plot of $\ln \rho$ vs. $T^{-1/4}$ for PPy-PF₆ samples in the insulating regime. Solid lines represent linear fit regions; (b) $\ln \rho$ vs. $T^{-1/2}$ for the same data. Solid lines represent linear fit regions. Symbols are as described in Table 2.5.

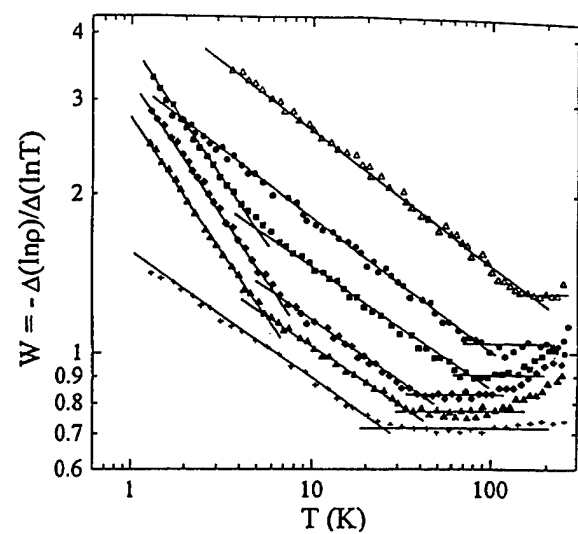
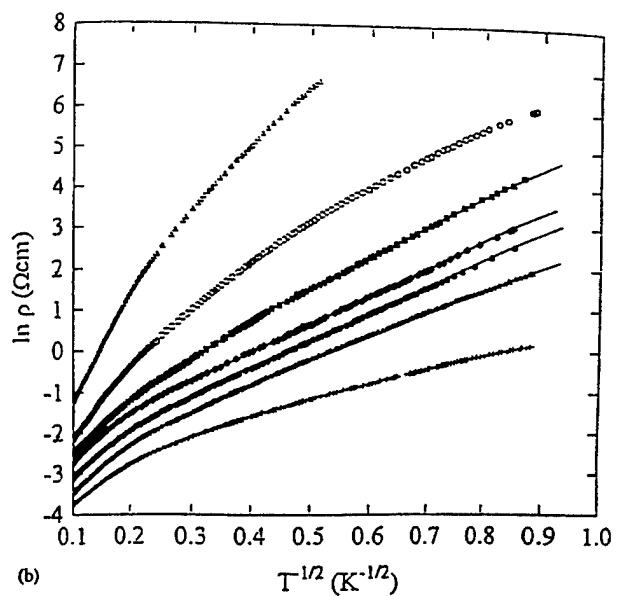


Fig. 2.44 Log-log plot of W vs. T for PPy-PF₆ samples in insulating regime. Solid lines represent different temperature regimes in which $x = 1/2$ (higher slopes) or $x = 1/4$ (lower slopes); the power law (zero slope) dependence can also be seen.

lines in Fig. 2.45 (see Table 2.5). The parameters $x = 1/2$ and T'_0 are used in Eq. (23) except for the PPy-PF₆ sample following Mott's law at this temperature. The localization length increases slightly as ρ_r decreases, as expected. The relatively small difference in the values of L_c for the PPy-PF₆ sample with $\rho_r = 107$ and $\rho_r = 2018$ could be due to the uncertainty in numerical constant t



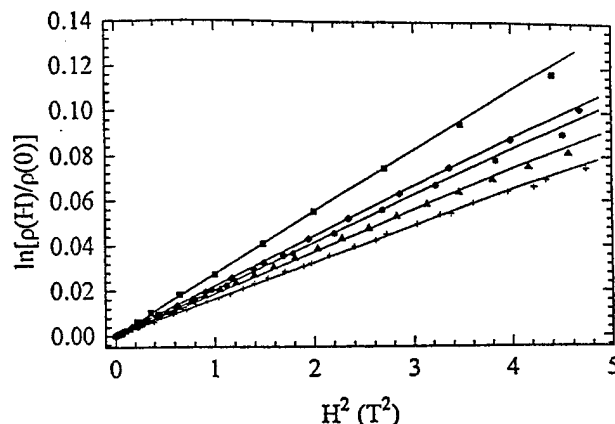


Fig. 2.45 The magnetic field dependence of the resistivity, $\ln [\rho(H)/\rho(0)]$ vs. H^2 for PPy-PF₆ samples in the insulating regime. The localization length was calculated from the slope (solid line) using Eq. (23).

in Eq. (23) calculated from two different theoretical models [122,179] applied for $\ln \rho \propto (T_0/T)^{1/4}$ and $\ln \rho \propto (T_0/T)^{1/2}$ dependences in the same temperature interval ($1.4 \text{ K} < T < 4.2 \text{ K}$).

Samples farther into the insulating regime ($\rho_r > 5 \times 10^3$) follow Mott VRH temperature dependence of the resistivity without showing crossover behavior. This implies that the Mott to ES crossover is restricted to the two limits, very close to the M-I transition (where the Coulomb gap may appear at millikelvin temperatures) and well on the insulating side [due to the decrease of $N(E_F)$ and L_c].

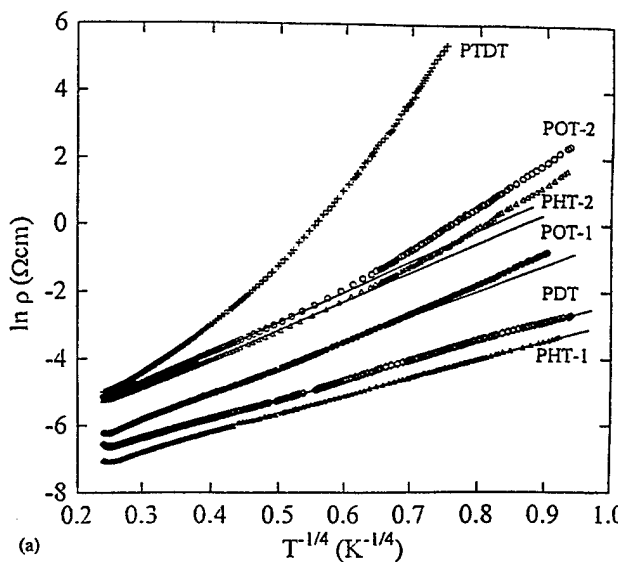


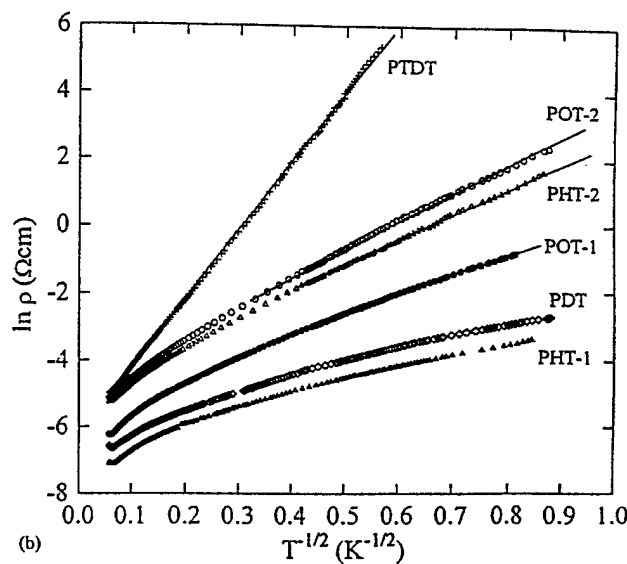
Fig. 2.46 (a) $\ln \rho$ vs. $T^{-1/4}$ for iodine-doped PAT samples. Solid lines represent linear fit regions. (b) $\ln \rho$ vs. $T^{-1/2}$ for the same data. Solid lines represent linear fit regions. Symbols are described in Table 2.6.

4. Polyalkylthiophenes

Advances in the synthesis of regioregular PATs have significantly improved the electronic properties by increasing the conjugation length [31,32]; the regular head-to-tail arrangement of the alkyl side chains in regioregular PATs has improved the crystalline coherence length over that in the regiorandom PATs. Moreover, side-chain-induced crystallization in regioregular PATs favors the self-assembly of well-ordered films when cast from solution.

In situ conductivity measurements were carried out during doping on several PAT samples [172]. Although the maximum conductivity obtained in regioregular PATs increases upon increasing the length of the side chain from butyl to decyl, the disorder that limits the conductivity is apparently determined by the solution casting process [31,32]. The maximum conductivities obtained for various regioregular PATs are summarized in Table 2.6. The highest room temperature conductivity, $\sigma_{RT} \sim 1200 \text{ S/cm}$, was from P3HT.

Typical examples of the temperature dependence of the resistivity of iodine-doped regioregular PATs are shown in Figs. 2.46a and 2.46b [172]. Although the room temperature conductivity of some of the PATs is considerably higher than those of PPy-PF₆ and PANI-CSA, the temperature dependence of the resistivity is rather strong compared to the best samples of PPy-PF₆ and PANI-CSA. For example, PHT-1 with room temperature conductivity $\sigma_{RT} \sim 1200 \text{ S/cm}$ has $\rho_r \approx 50$. In general, as is the case for all other conducting polymers as well, the higher the value of σ_{RT} , the lower the value of



ρ_r , as shown in Table 2.6. The temperature dependence of the resistivity for PBT and PDDT is not shown in Fig. 2.46 since it is identical to that of POT-1.

The temperature dependence of conductivity of the PATs can be classified into three categories [172]:

1. For $\sigma_{RT} = 700-1200$ S/cm and $\rho_r < 100$, the power law dependence was observed in the temperature range 50–250 K with $\ln \rho \propto (T_0/T)^{1/4}$ behavior below 50 K.
2. For $\sigma_{RT} = 200-600$ S/cm and $2 \times 10^2 < \rho_r < 2 \times 10^3$, the crossover from $T^{1/4}$ to $T^{1/2}$ occurs (Mott to ES) at temperatures below 10 K.
3. For $\sigma_{RT} < 200$ S/cm and $\rho_r = 10^4-10^6$, $\ln \rho \propto (T_0/T)^{1/2}$ behavior was observed.

The existence of these three distinct regimes in iodine-doped PATs was confirmed from the W vs. T plots shown in Fig. 2.47. The data in regimes (1) and (2) are very similar to those obtained from PPy-PF₆. The power law dependence observed for PHT-1 and PDT samples above 50 K indicates that the samples are near the critical regime. The crossover from Mott to ES VRH for PBT, POT-1, and PDDT indicates that correlation effects in the insulating regime near the M-I transition are important. The VRH parameters summarized in Table 6 are consistent with results from the previous analysis of the PPy-PF₆ data.

The field dependence of $\rho(T, H)$ for magnetic fields up to $H = 8$ T for PPy-PF₆ and iodine-doped POT samples exhibiting the highest crossover temperature from Mott to ES VRH conduction is shown in Fig. 2.48 [172]. Although strong magnetic fields significantly alter the lo-

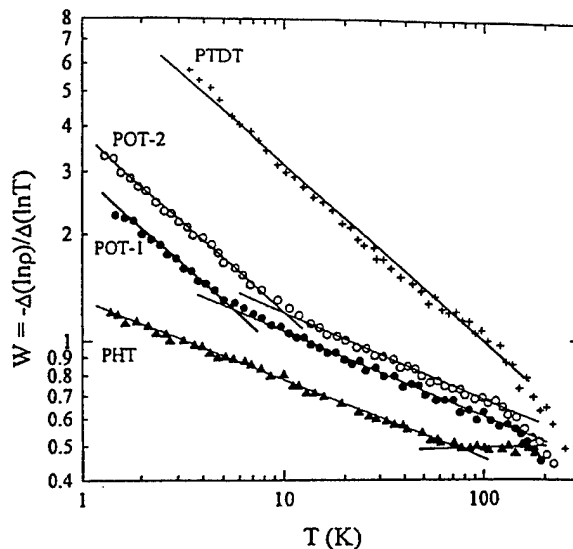


Fig. 2.47 Log-log plot of W vs. T for iodine-doped PAT samples. Solid lines represent different temperature regimes in which $x = 1/2$ (higher slopes) or $x = 1/4$ (lower slopes).

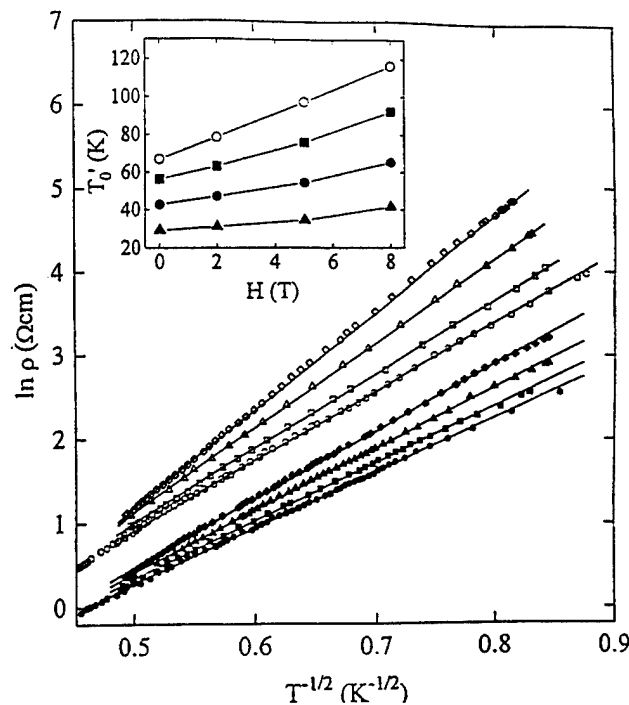


Fig. 2.48 The temperature dependence of the resistivity of PPy-PF₆ ($\rho_r = 734$, solid symbols) and iodine-doped POT ($\rho_r = 1640$, open symbols) in various magnetic fields plotted as $\ln \rho$ vs. $T^{-1/2}$: (\bullet , \circ) $H = 0$, (\blacksquare , \square) $H = 2$ T, (\blacktriangle , \triangle) $H = 5$ T, and (\blacklozenge , \lozenge) $H = 8$ T. The T_0' values obtained from the slopes (solid lines) for various samples are plotted as a function of the magnetic field in the inset.

calized electronic wave functions, decreasing the overlap and increasing the hopping length, the $\ln \rho \propto (T_0/T)^{1/2}$ law remains valid but with increased T_0' . Various VRH exponents ($x = 3/5, 1/2$, and $1/3$) have been suggested as appropriate in a strong magnetic field in the presence of the Coulomb gap [184–187]; however, the data in Fig. 2.48 clearly indicate $x = 1/2$. The magnetic field dependences of $T_0'(H)$ obtained from the slopes in Fig. 2.48 are plotted in the inset of Fig. 2.48; the data indicate $T_0'(H)/T_0' \propto H^p$ with $p = 1.0-1.2$, consistent with Shklovskii's theory [185, 186].

The $\ln \rho \propto (T_0/T)^{1/2}$ dependence for samples in regime (3), which have relatively large resistivity ratios ($\rho_r > 10^4$), is typical of granular metals. Similar behavior has been reported for polyaniline doped with conventional protonic acids [65–69] and for doped polypyrrole [117–119]. In such samples, the strong disorder and the formation of inhomogeneous “metallic islands” dominate over the $\ln \rho \propto (T_0/T)^{1/4}$ behavior expected for homogeneously disordered materials, as previously described. The $\ln \rho \propto (T_0/T)^{1/2}$ dependence observed over a wide temperature range has a different origin from the ES VRH conduction in the homogeneous limit. Phase segregation of the doped and undoped regions (i.e., the

inhomogeneous doping) result in the formation of granular metals. Similar behavior was observed in microscopically disconnected networks of polyaniline in blends at concentrations below the percolation threshold (see following section for details) [175].

5. Polyaniline

Progress in the solution processing of high quality conducting PANI films showed that the electrical transport properties of PANI can be greatly improved by reduction of disorder [34,35]. In this section, we address the differences in transport properties between PANI-CSA processed from solution in *m*-cresol [27–30] and PANI doped by conventional protonic acids [65–69] such as HCl and H₂SO₄.

The temperature dependence of the resistivity of PANI-CSA is sensitive to the sample preparation conditions. This is clearly shown in the W vs. T plots, e.g., as in Fig. 2.49. The resistivity ratio for PANI-CSA is typically less than 50; in the metallic regime ($\rho_r < 3$), $\rho(T)$ approaches a finite value as $T \rightarrow 0$ [151]; in the critical regime ($\rho_r \sim 3$), $\rho(T)$ follows power law dependence; and in the insulating regime ($\rho_r > 4$), $\rho(T)$ follows Eq. (15) (Mott VRH conduction) with VRH exponent $x = 0.25 \pm 0.3$ and $T_0 = 10^1\text{--}10^3$. The Mott to ES VRH crossover noted for PPy-PF₆ and PATs has not yet been clearly observed in PANI-CSA. The systematic variation from the critical regime to the VRH regime as the value of ρ_r increases from 2.94 to 4.4 is shown beautifully in the W vs. T plot of Fig. 2.49. This is a classical demonstration of the role of disorder-induced localization in doped conducting polymers.

Plots of $\ln \rho$ vs. $T^{-1/x}$ for various PANI samples, doped with CSA and doped with conventional protonic acids (HCl and H₂SO₄), are shown in Figs. 2.50a and 2.50b. When PANI-CSA samples are treated (“washed”) with acetone after casting, the behavior of $\rho(T)$ changes to $\ln \rho \propto T^{1/2}$ due to the partial deprotonation. PANI-HCl samples (“exchanged” samples) were prepared by the exchange of counterions in HCl solution after complete dedoping of PANI-CSA. For a stretch-“oriented” PANI-HCl sample with a draw ratio of 3, the resistivity data (parallel to the draw direction) are shown in Fig. 2.50b [188]. The resistivity ratio for these samples is typically $\rho_r > 10^3$, and the typical values of T_0 increase from $T_0 = 160$ K for exchanged PANI-HCl to $T_0 = 5400$ K for PANI-H₂SO₄ (see Table 2.7).

6. Summary

The transport properties of PPy-PF₆, iodine-doped PAT, and doped PANI in the insulating regime have common features; the hopping transport can be categorized as follows:

1. Very close to the M-I transition ($\rho_r < 10^2$), the low temperature resistivity follows Mott’s VRH above 1 K.
2. Samples with intermediate $\rho_r (10^2 < \rho_r < 10^3)$ show crossover from Mott to Efros–Shklovskii hopping (from $\ln \rho \propto T^{-1/4}$ to $\ln \rho \propto T^{-1/2}$) below 10 K, with a Coulomb gap of $\Delta_C = 0.3\text{--}0.6$ meV. The data yield $T_0/T_0' = 85\text{--}115$, $4\pi e^2 N(E_F) L_c^2 / \epsilon = 0.70\text{--}0.95$, and values of T_{cross} that are nearly identical to those estimated from $T_{\text{cross}} = 16$

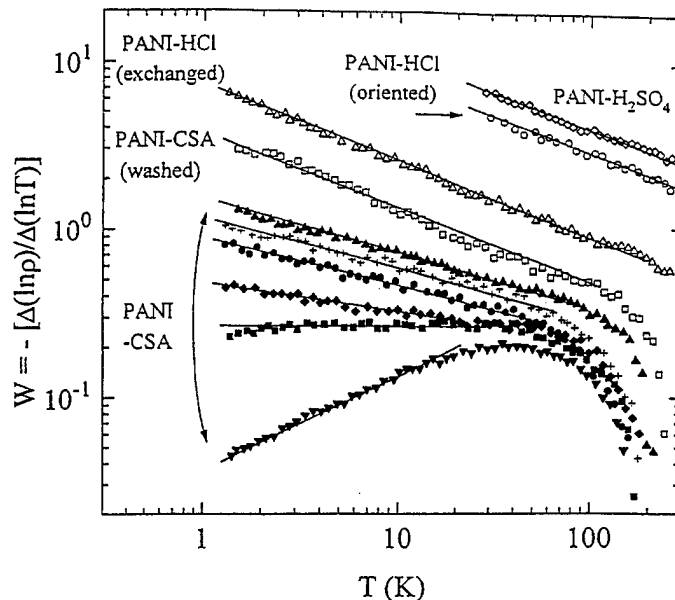


Fig. 2.49 Log-log plot of W vs. T for various types of doped PANI samples.

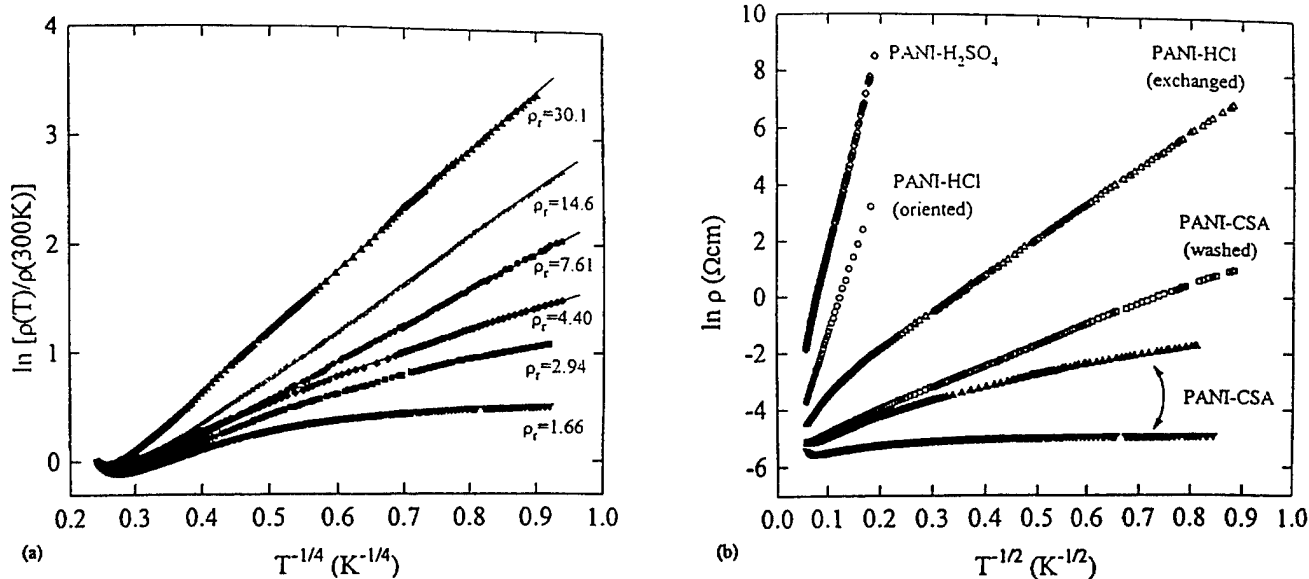


Fig. 2.50 (a) $\ln \rho$ vs. $T^{-1/4}$ for PANI-CSA samples. Solid lines represent linear fit regions. (b) $\ln \rho$ vs. $T^{-1/2}$ for various doped PANI samples.

$(T'_0)^2/T_0$; all are close to the values predicted by Castner [78]. The resistivity at low temperature in a strong magnetic field follows the $\ln \rho \propto (T'_0/T)^{1/2}$ law, where $T'_0(H)/T'_0(0) \propto H^p$ with $p = 1.0-1.2$, in agreement with the theory of Shklovskii.

3. For samples farther into the insulating regime ($\rho_r > 10^3$), $\rho(T)$ shows two distinct types of behavior. In homogeneous material ($L_c \geq$ structural coherence length), Mott VRH conduction is recovered. In inhomogeneous samples ($L_c \leq$ structural coherence length), where "metallic islands" are formed after partial dedoping or by strong morphological disorder, $\ln \rho \propto (T'_0/T)^{1/2}$, characteristic of a granular system. In this granular metal limit, there is a substantial nonlinear hopping

contribution to the intrinsic diffusion thermoelectric power of doped conducting polymers.

F. Thermopower Near the M-I Transition in Doped Conducting Polymers

1. Introduction

Although the thermopower, $S(T)$, of doped conducting polymers has been studied for many years, the evolution of $S(T)$ as a function of the extent of disorder is not yet fully understood. Usually, thermopower is not as sensitive to disorder as electrical conductivity, since the latter is strongly dependent on the scattering and hopping processes involved in charge transport in the disorder-induced localized regime. Kaiser [19] analyzed the

Table 2.7 Experimental Values and Variable Range Hopping Parameters for PANI Samples

Sample	Symbol (Fig. 2.49)	$\sigma(300 K)$ (S/cm)	ρ_r	T_0 (K)	T'_0 (K)
PANI-CSA	▼	225	1.66	18.8	
	■	322	2.94		
	◆	112	4.40		
	●	226	7.61		129
	+	268	14.6		390
	▲	171	30.1		1337
PANI-CSA (washed)	□	165	486	70.6	
PANI-HCl (exchanged)	△	88.4	8.8×10^4		164
PANI-HCl (oriented)	○	40.8			3060
PANI-H ₂ SO ₄	◊	6.31			5400

thermopower in terms of the heterogeneous model in which the thermal current carried by phonons is less impeded by thin insulating barriers than the electric current carried by electrons or holes. Wang et al. [69] considered the interplay of dimensionality of coupled metallic chains. Li et al. [70] suggested that the U-shaped $S(T)$ could result from the temperature-dependent tunneling between granular metallic islands. More recently, however, Yoon et al. [172] observed that the gradual change of $S(T)$ from the positive linear temperature dependence to the negative U-shaped behavior was correlated with microstructure and indicative of negative hopping contributions in addition to the metallic diffusion thermoelectric power.

2. Theory

The diffusion thermoelectric power for a metallic system can be expressed as [189]

$$S_d(T) = \frac{\pi^2}{3} \left(\frac{k_B}{e} \right) k_B T \left[\frac{d \ln \sigma(E)}{dE} \right]_{E_F} \quad (24a)$$

or alternatively,

$$S_d(T) = + \frac{\pi^2}{3} \left(\frac{k_B}{|e|} \right) \left(k_B T \frac{z}{E_F} \right) \quad (24b)$$

where the energy dependence of $\sigma(E)$ arises from a combination of the band structure and details of the scattering mechanism, and z is a constant (of order unity), again determined from the band structure and the energy dependence of the mean scattering time. The linear temperature dependence of $S(T)$ corresponds to the characteristic diffusion thermopower of a metal. Although phonon drag often contributes to the thermopower of metals, this contribution is expected to be suppressed by disorder [190,191].

The VRH hopping contribution to the thermoelectric power depends on the details of the hopping mechanism [42,43],

$$S_{\text{hop}}(T) = \frac{1}{2} \left(\frac{k_B}{e} \right) \left(\frac{\Delta_{\text{hop}}^2}{k_B T} \right) \left[\frac{d \ln N(E)}{dE} \right]_{E_F} \quad (25)$$

where Δ_{hop} is the mean hopping energy. From Eqs. (17a) and (17b), we have $S_{\text{hop}} \propto T^{1/2}$ for $x = 1/4$ and $S_{\text{hop}} = \text{constant}$ for $x = 1/2$ [172]. Thus, in a Fermi glass with a finite density of states at E_F , $S(T)$ should have contributions from both $S_d(T)$. One finds that the hopping contribution to the total thermoelectric power of PANI-CSA samples fits well to the empirical formula

$$S(T) - A T = B T^{1/2} + C \quad (26)$$

where A is the linear slope of $S(T)$ and B and C are fitting parameters (see Section III.F.4 for details). The magnitude of hopping thermoelectric power increases

with ρ_r . The origin of the positive or negative sign for hopping contributions is not understood (generally the sign depends on asymmetry corrections to the density of states with respect to the Fermi level [190]).

Assuming energy-independent scattering for $S_d(T)$, the magnitude of hopping contribution can be estimated by using Eqs. (24) and (25),

$$S_{\text{hop}}/S_d \approx (3/2\pi^2) (\Delta_{\text{hop}}/k_B T)^2 = (3/2\pi^2) W^2 \quad (27)$$

where $W = \Delta_{\text{hop}}/k_B T = x(T_0/T)^\alpha$ is the reduced activation energy. For $W < 1$, $S_{\text{hop}}/S_d \ll 1$, and the hopping contribution to the thermoelectric power is insignificant. For $x = 1/4$, Eq. (27) becomes $S_{\text{hop}}/S_d \approx (\lambda T_0/T)^{1/2}$, where $\lambda \sim 10^{-3}$; and for $x = 1/2$, $S_{\text{hop}}/S_d \approx (\lambda' T_0/T)$, where $\lambda' \sim 10^{-1}$ [172]. The condition for the hopping thermoelectric power to be comparable to the diffusion thermoelectric power is, for example, $T_0 \geq 10^5$ K or $T_0' \geq 10^3$ K at 100 K. In the homogeneous limit ($\rho_r < 10^2$, $x = 1/4$), T_0 less than 10^3 K implies that the hopping contribution to $S(T)$ is negligible. In the inhomogeneous limit ($\rho_r > 10^3$, $x = 1/2$), the hopping thermoelectric power contributions from both the large values of $T_0 > 10^4$ and $T_0' > 10^2$ become important, and the temperature dependence of the resistivity is $\ln \rho \propto T^{-1/2}$.

3. Polyacetylene

The thermopower of doped $(\text{CH})_x$ has been extensively studied by Kaiser [19] and by Park et al. [89–92]. The quasilinear temperature dependence is consistent with metallic contribution, while the “knee” around 50 K has been attributed to a contribution from the electron–phonon interaction. Park et al. [89–92] and Yoon [188] carried out extensive thermopower measurements on $(\text{CH})_x$ samples doped with iodine and various transition metal halides. Park et al. [192] have also shown that the thermopower is positive for both I- $(\text{CH})_x$ (*p*-type) and K- $(\text{CH})_x$ (*n*-type), indicating that the sign of thermopower is not determined by the sign of the charge carrier, a surprising and unexpected result. As noted above, the sign and magnitude of thermopower in doped $(\text{CH})_x$ are determined by the details of band structure and the dominant contributions from diffusion and hopping transport [172].

4. PANI-CSA

The thermopower data for various types of doped PANI are shown in Figs. 2.51a and 2.51b [172,193]. The room temperature value is approximately $10 \mu\text{V/K}$ with small variations ($\pm 2 \mu\text{V/K}$) depending on the details of the process for casting the film. The magnitude and positive sign of $S(T)$ are similar to those obtained from a number of partially doped *p*-type conducting polymers [89–92]. The positive sign of the thermopower is consistent with the calculated band structure of the metallic emeraldine salt, a three-quarter-filled π band with one hole per

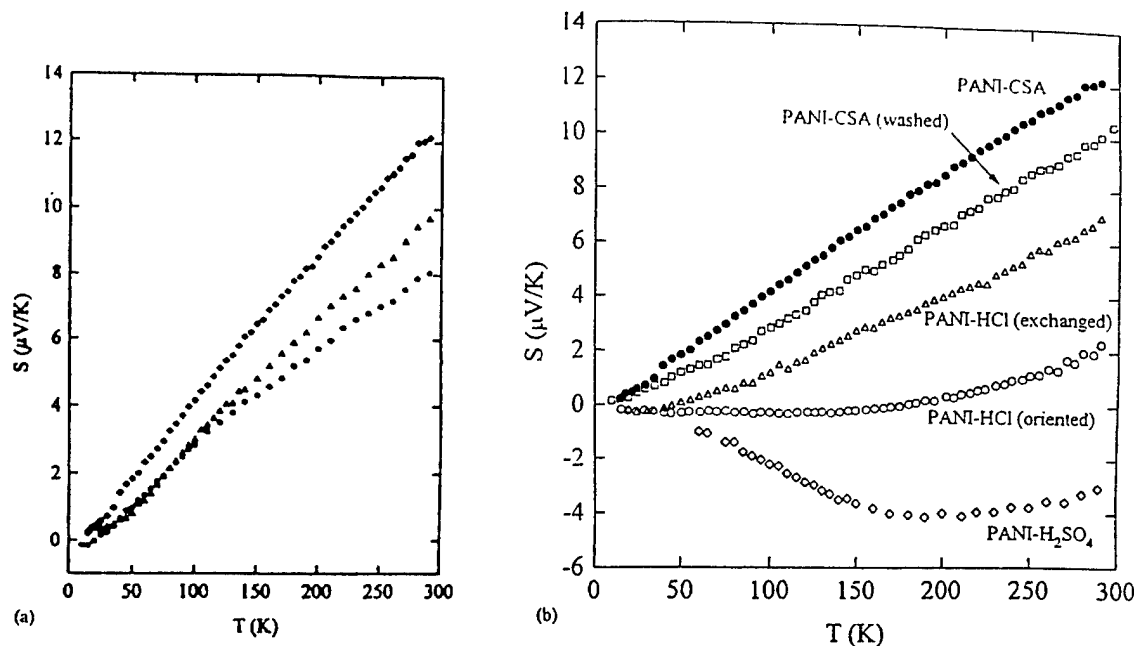


Fig. 2.51 (a) $S(T)$ vs. T of PANI-CSA samples in the (●) metallic, (▲) critical, and (■) insulating regimes. (b) $S(T)$ for various protonated PANI samples including the ones in deep insulating regime.

(—B—NH—B—NH—) repeat unit [193]. Although ρ_r for PANI-CSA samples varies by three orders of magnitude near the M-I transition, the quasilinear thermopower is relatively insensitive to ρ_r . The linear temperature dependence of $S(T)$ corresponds to the diffusion thermoelectric power, Eq. (24). The relatively large magnitude, $S(300 \text{ K}) = 8\text{--}12 \mu\text{V}/\text{K}$, indicates the diffusion of charge carriers in electronic states with relatively narrow bandwidth. Using $z = 1$, $E_F \approx 1 \text{ eV}$ [194,195] and $T = 300 \text{ K}$, Eq. (24) yields $S(300 \text{ K}) \approx 7.5 \mu\text{V}/\text{K}$, close to the measured value. The density of states estimated from the magnitude of $S(T)$ [193] is 1.1–1.6 states per electronvolt per two rings (assuming energy-independent scattering), consistent with the value of 1 state/eV per two rings obtained from magnetic susceptibility measurements [27–30,155].

Table 2.8 Experimental Values of Thermoelectric Power and Fitting Parameters for PANI Samples

Sample	Symbol (Fig. 2.51b)	$S(300 \text{ K})$ ($\mu\text{V}/\text{K}$)	B ($\mu\text{V}/\text{K}^{3/2}$)	C ($\mu\text{V}/\text{K}$)
PANI-CSA	●	+12.8		
PANI-CSA (washed)	□	+10.5	-0.13	-0.09
PANI-HCl (exchanged)	△	+7.0	-0.35	+0.37
PANI-HCl (oriented)	○	+2.3	-0.79	+3.01
PANI-H ₂ SO ₄	◊	-3.0	-1.35	+6.89

The U-shaped temperature dependence $S(T)$ appears only when the hopping contribution (usually in the inhomogeneous limit) becomes significant, as shown in Fig. 2.51b. The least squares fitting parameters for B and C [Eq. (26)] are listed in Table 2.8. Neither the phonon drag effect [190], which is usually suppressed by disorder, nor the positive contribution due to the electron–phonon

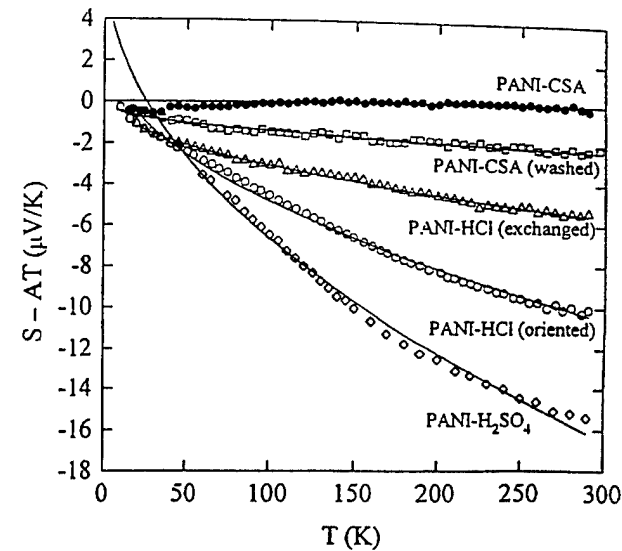


Fig. 2.52 Hopping contributions to the diffusion thermoelectric power of various doped PANI samples. Solid lines are fits to Eq. (24).

interaction [19] was observed. The data showing the hopping contribution to the thermopower for various doped PANI samples are shown in Fig. 2.52.

5. PPy-PF₆

The temperature dependences of $S(T)$ for various PPy-PF₆ samples near the M-I transition are shown in Fig. 2.53 [167]. The room temperature value is positive, with $S(300\text{ K}) = + (9-12)\text{ } \mu\text{V/K}$; the magnitude decreases as ρ_r decreases. The relatively large magnitude of $S(T)$ again implies that the partially filled π band is relatively narrow, in this case less than 1 eV. The density of states at the Fermi level, estimated from Eq. (24), is $N(E_F) \sim 1.0-1.6\text{ states/eV}$ per four pyrrole units, assuming the ideal doping level of one dopant per four rings. As for PANI-CSA, $S(T)$ for PPy-PF₆ is rather insensitive to ρ_r near the disorder-induced M-I transition.

6. Summary

The thermopower of doped conducting polymers near the disorder-induced M-I transition is not as sensitive to disorder as the conductivity. Because of the continuous density of states in a Fermi glass, $S(T)$ is nearly identical in the metallic and insulating regimes. Deep in the insulating regime, however, contributions from the "metallic" diffusion thermopower (positive with $S \propto T$) and the insulating hopping thermopower become comparable; the latter can be positive or negative depending on the asymmetric corrections to the density of states with $S_{\text{hop}} \propto T^{1/2}$ for $x = 1/4$ and $S_{\text{hop}} = \text{constant}$ for $x = 1/2$ depending on whether the material is homogeneous or granular.

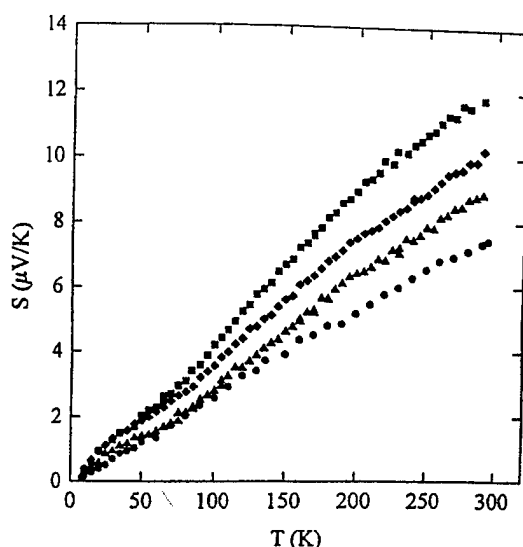


Fig. 2.53 Plots of $S(T)$ vs. T of PPy-PF₆ samples in various regimes: I2 (■), Ic1 (◆), Mc1 (▲), and M1 (●).

IV. TRANSPORT IN POLYANILINE NETWORKS

A. Introduction

The metal-insulator transition in doped conducting polymers can be investigated from a different perspective by blending a metallic conducting polymer into an insulating polymer as host matrix. The counterion-induced solution processing of PANI-CSA [27-30] has made possible the fabrication of conducting polymer blends in the form of films and fibers and thereby provided the opportunity to study transport in such blends [153,154,196,197].

Although classical percolating systems (where $f_c \approx 16\%$ by volume for globular conducting objects dispersed in an insulating medium in three dimensions) have been studied in detail for many years [198], the transport properties of conducting polymer blends, consisting of a network of fibrillar conducting objects, are in the early stage of investigation [199-206]. From previous experimental and theoretical studies of polymer composites filled with metal [207,208] or carbon fibers [209], it is known that the percolation threshold decreases when the aspect ratio (A) of the conducting object increases, where A is the ratio of the length to the diameter [210].

The formation of self-assembled networks in conducting polymer blends containing polyaniline provides a new class of percolating systems [153,154,175,196,197]. Because the multiply connected, phase-separated morphology is the lowest energy configuration, the critical volume fraction of conducting material required to reach the percolation threshold can be quite low. Near the critical concentration for percolation, the conducting networks in the blends are fractal [196,197]. Transport on such fractal networks is of fundamental interest but poorly understood.

The PANI-CSA networks in PANI-CSA/PMMA blends exhibit an extremely low percolation threshold and a continuous increase of conductivity, $\sigma(f)$, while retaining the mechanical properties of the matrix polymer [153,154,175,196,197]. Homogeneous films of any size and shape can be easily fabricated either by dissolving the conducting PANI-CSA and a suitable matrix polymer in a common solvent and casting onto a substrate or by melt processing the blend. The networks in such blends have been directly imaged by transmission electron microscopy (TEM) [153,154,175,196,197]. The intrinsic metallic nature of PANI-CSA (as inferred from the positive temperature coefficient of resistivity) is retained upon dilution to low volume fractions (as low as $f \approx 0.003$), a feature that is not observed in other conducting polymer blends. Moreover, the positive and linear temperature dependence of thermopower remains unchanged upon dilution to 0.6% volume fraction of PANI-CSA [193,196,197]. Thus, the transport data imply the formation of a self-assembled interpenetrating

fibrillar network made up of high quality PANI-CSA; the network forms spontaneously during the course of liquid-liquid phase separation.

Since the homogeneity and processibility of conducting polymer blends are superior to those of filled polymer composites, these all-polymer materials are of technological interest. The potential of such conducting polymer blends for use in a variety of applications has stimulated a more detailed study of these materials with a goal of achieving a deeper understanding of the effect of processing on the morphology and thus on the transport properties of the materials. For example, PANI-CSA networks have been demonstrated to be useful as carrier injection electrodes in conjugated polymer light-emitting diodes and as the grid in polymer grid triodes, a new architecture for "plastic" transistors [211-213].

The systematic change in the VRH exponent (x) as a function of the volume fraction of PANI-CSA suggests superlocalization of the electronic wave functions on the fractal network for concentrations near the percolation

threshold [175,196,197]; x increases from 0.25 (at $f \approx 0.8$) to $x \sim 1$ upon decreasing the volume fraction of PANI-CSA to the percolation threshold. Because of the relatively high conductivity of the phase-separated PANI-CSA in PMMA, it was possible to extend the measurements well below f_c . Below the percolation threshold, $x \approx 0.5$, typical of that observed in granular metals and consistent with the disconnected granular morphology seen in the TEM micrographs [153,154,175].

B. Sample Preparation

PANI-CSA solutions are prepared by dissolving the emeraldine base form of PANI and CSA at 0.5 molar ratio of CSA to phenyl-N repeat unit in *m*-cresol [27-30]. This solution is then mixed in the appropriate ratio with a solution of PMMA in *m*-cresol. Films of thickness 20-60 μm were obtained by casting the blend solution onto a glass plate. After drying at 50°C in air for 24 h, the poly-

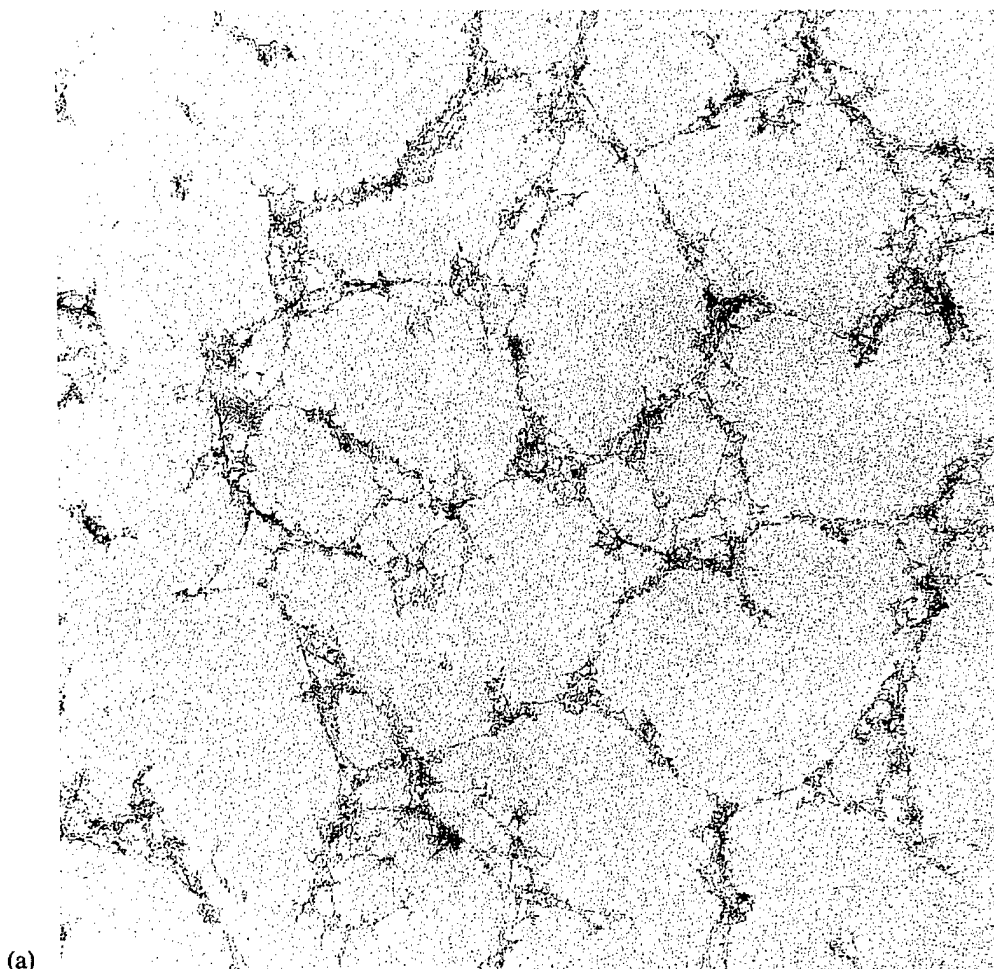


Fig. 2.54 Transmission electron micrographs of extracted PANI-CSA/PMMA polyblend films containing (a) $f = 0.005$ and (b) $f = 0.0025$ of PANI-CSA.

blend film was peeled off the glass substrate to form a free-standing film for transport measurements.

The features of the network are dependent on the molecular weight of PMMA [27–30,153,154]. The use of lower molecular weight PMMA enables greater mobility of the macromolecules during the process of liquid–liquid phase separation (carried out slowly at 50°C), thereby enhancing the diffusion of PANI-CSA in PMMA. As a result, the lower molecular weight blends more closely approach the morphology associated with the minimum energy of the PANI-CSA self-assembled network.

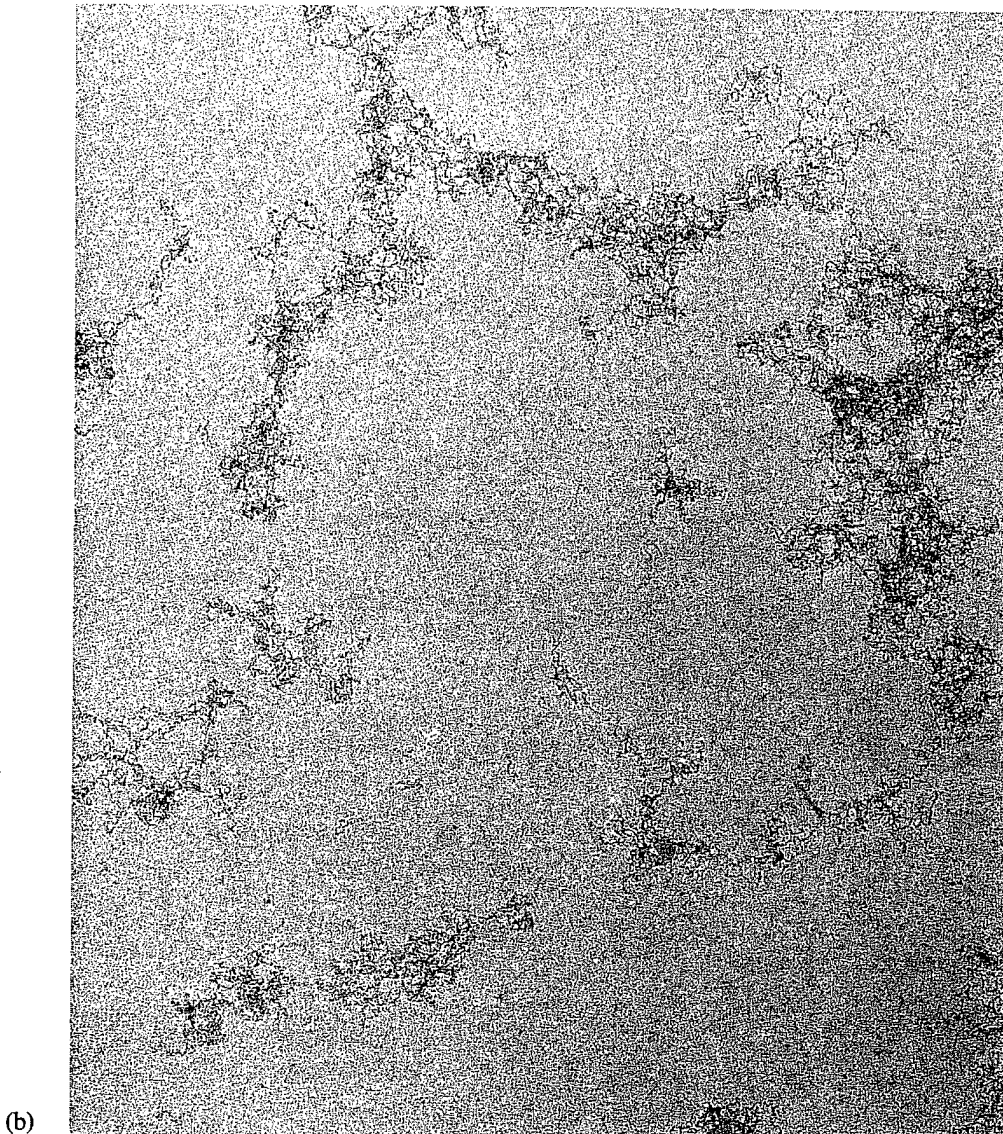
C. Results and Discussion

The electrical properties of PANI-CSA/PMMA blends are novel compared to those observed in more tradi-

tional systems [153,154,175,196,197]. Theoretical models of superlocalization [214–217], multifractal localization [218,219], multiple percolation [206], and high field magnetotransport [220,221] near the percolation threshold have provided additional stimulus to carefully study the transport properties of the PANI-CSA network, especially at low volume fractions near and below the percolation threshold. Improvements in material quality have enabled the temperature dependence of conductivity measurements and magnetoresistance measurements in samples containing volume fractions of PANI-CSA as low as 0.02% ($f = 0.0002$) [175].

1. Electron Microscopy and Conductivity Near the Percolation Threshold

As shown in Figs. 2.54a and 2.54b, the PANI-CSA network can be seen clearly in TEM micrographs of blends



made from 0.5% and 0.25% PANI-CSA in PMMA (see Refs. 153 and 154 for details on the preparation of samples for imaging by TEM). Figures 2.54a and 2.54b resemble the typical scenario imagined for a percolating medium [198] with "links" (PANI-CSA fibrils), "nodes" (crossing points of the links), and "blobs" (dense, multiply connected regions). The distance between the nodes and the typical diameter of the blobs is assumed to be on the order of the percolation correlation length (ξ_p). The TEM photograph of the sample containing 0.5% PANI-CSA indicates that $\xi_p \sim 400$ –800 Å [153,154,175], numerous links, with diameters of about 100–500 Å, are clearly visible. The 0.25% sample is just below the percolation threshold; there are rather few links between the nodes and blobs. Thus, at these very dilute concentrations, the network becomes unstable and tends to break up; the critical concentration is approximately 0.3% PANI-CSA in PMMA.

The TEM micrographs suggest the existence of a minimum diameter for the connecting links on the order of a few hundred angstroms. Although the origin of this minimum dimension is not understood in detail, it appears that when the surface-to-volume ratio of the PANI-CSA segregated regions becomes too large, the connected network structure cannot be maintained.

The conductivity versus volume fraction of PANI-CSA is shown in Table 2.9 and in Fig. 2.55a. The σ vs. f data are dependent upon the mass distribution among the links, nodes, and blobs in the sample, which in turn are determined by various parameters involved in the

Table 2.9 The Room Temperature Conductivity and Resistivity Ratio of PANI-CSA/PMMA Blends at Various Volume Fractions (f) of PANI-CSA

f	$\sigma(300 \text{ K}) (\text{S}/\text{cm})$	$\rho(4.2 \text{ K}) \rho(300 \text{ K})$
1	200–400	1.3–10
0.8	140	11
0.67	110	13
0.5	66	18
0.33	21	19
0.12	9	30
0.08	4	60
0.04	1.8	210
0.02	0.7	710
0.015	0.4	1830
0.012	0.22	2200
0.010	0.17	2600
0.008	0.12	—
0.006	0.074	3780
0.004	0.014	5250
0.003	0.003	—
0.002	0.0012	—
0.001	10^{-4}	—
0.0005	10^{-5}	—

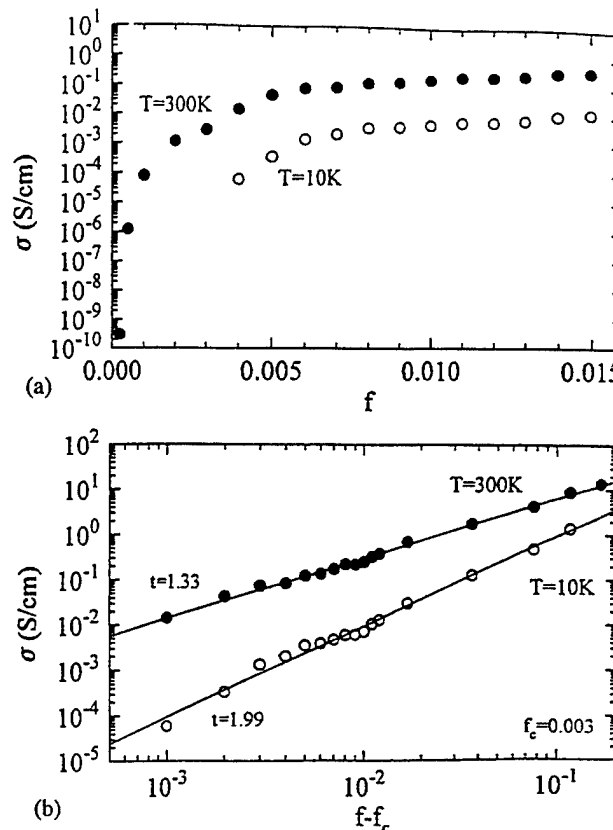


Fig. 2.55 (a) Conductivity (\log_{10} scale) versus volume fraction (f) of PANI-CSA at 300 and 10 K. (b) \log_{10} - \log_{10} plot of σ vs. $(f-f_c)$ at 300 K (●) and 10 K (○), where $f_c = 0.003$. The solid line through the points corresponds to a slope (t) of 1.99 at 10 K and 1.33 at 300 K, respectively.

sample preparation—the molecular weight of PANI and PMMA, the viscosity of the polyblend solution, the solvent, the drying temperature, etc. The data in Fig. 2.55a were obtained from samples prepared by optimizing some of the above parameters with the intent of allowing the system to approach equilibrium during the liquid–liquid phase separation.

The conductivity of the sample containing 0.05% PANI-CSA is approximately 10^{-5} S/cm, several orders of magnitude higher than the typical values of conductivity obtained in filled polymer composites containing similar volume fractions of carbon black [222–224; H. B. Brom, personal communication, 1994.] or graphite particles [225, 226]. Although percolation thresholds as low as 0.1 vol % [222, 223; H. B. Brom, personal communication] and 0.4 wt % [224] have been reported for carbon black/polymer composites, the conductivity near the percolation threshold for those samples is less than 10^{-7} S/cm.

Even though the TEM photographs [153,154,175] show that the macroscopic connectivity in PANI-CSA/PMMA blends is rather low for samples containing less

than 0.5% PANI-CSA, a small number of residual nanoscopic connections in the phase-segregated structure persist down to volume fractions of PANI-CSA as low as 0.01%. As shown in Table 2.9, room temperature conductivities on the order of 10^{-4} – 10^{-5} S/cm are observed in samples containing such extremely low volume fractions of PANI-CSA. The conductivity increases approximately four orders of magnitude (from 10^{-10} to 10^{-6} S/cm) when the PANI-CSA content is increased from $0.01 \pm 0.005\%$ to $0.025 \pm 0.005\%$, as shown in Fig. 2.55a. This suggests that nanoscopic connectivity probably does occur at these extremely low volume fractions of PANI-CSA, although such links are not clearly observable within the resolution limits of the TEM micrographs.

In order to identify the percolation threshold more precisely, the data were fit to the scaling law of percolation theory [198],

$$\sigma(f) \approx \sigma_T |f - f_c|^t \quad (28)$$

where $\sigma_T \approx (r_h)^{\zeta_R} \sum(r_h)$, which is interpreted as the conductance for each basic unit; t is the critical exponent ($t = 1$ in two dimensions and $t = 2$ in three dimensions); ζ_R is the resistivity scaling exponent ($\zeta_R = 0.975$ in two dimensions and 1.3 in three dimensions); r_h is the hopping length; $(r_h)^{\zeta_R} \sim (T_0/T)^{\zeta_R \gamma / \zeta}$, which contains the information about the fractal network (where x and ζ are the VRH conductivity and the superlocalization exponent, described in detail below).

The fit to Eq. (28) is shown in Fig. 2.55b; at 10 K, we find $f_c = 0.3 \pm 0.05\%$ and $t = 1.99 \pm 0.04$, in agreement with the predicted universal value of $t = 2$ for percolation in three dimensions [198]. At room temperature, however, $t = 1.33 \pm 0.02$ (and $f_c = 0.3$). The smaller value of the exponent at room temperature arises from thermally induced hopping transport between disconnected (or weakly connected) parts of the network. Similar values for both the percolation threshold (0.4 wt %) and the critical exponent ($t \approx 1.3$, at room temperature) have been obtained from carbon black/polyethylene/polystyrene blends and attributed to the two-dimensionality of the system [224]. An important difference between conducting polymer blends and filled polymer systems containing metallic particles or carbon black is that the conductivity of the conducting objects in the latter are nearly temperature-independent or exhibit a metallic temperature dependence, whereas for conducting polymers the moderate temperature dependence associated with variable range hopping within the conducting polymer plays an important role.

At 10 K and at room temperature, the values of the electrical conductivity of PANI-CSA/PMMA samples with $f \approx f_c$ are on the order of 10^{-5} S/cm and 10^{-3} S/cm, respectively, values that are quite high compared to those obtained with other PANI blends. For example, polyaniline blends made by dispersing intractable polyaniline in host polymers [204,205] show percolation only

at much higher levels, $f_c \approx 8.4\%$. In such dispersions, the room temperature conductivity at f_c is five orders of magnitude lower, on the order of 10^{-8} S/cm.

2. Temperature Dependence of the Network Resistivity

The temperature dependence of the resistivity for PANI-CSA/PMMA blends is shown in Fig. 2.56 for $0.002 \leq f \leq 1$ [175]. As a metallic system near the boundary of the metal–insulator transition, $\rho(T)$ in PANI-CSA is characterized by a positive temperature coefficient [34,35]. Although the positive temperature coefficient is restricted to higher temperatures upon dilution of PANI-CSA in PMMA, it is remarkable that this distinctly metallic feature is observed even in samples containing volume fractions of PANI-CSA as low as 0.3%, indicating that even at such dilution the PANI-CSA within the phase-separated network is comparable in quality to that of pure PANI-CSA.

The temperature dependence of the resistivity is relatively weak above the percolation threshold, as shown in Fig. 2.56. The data above 4.2 K show a qualitative change for samples with f below and above the percolation threshold (the resistivity measurements could not

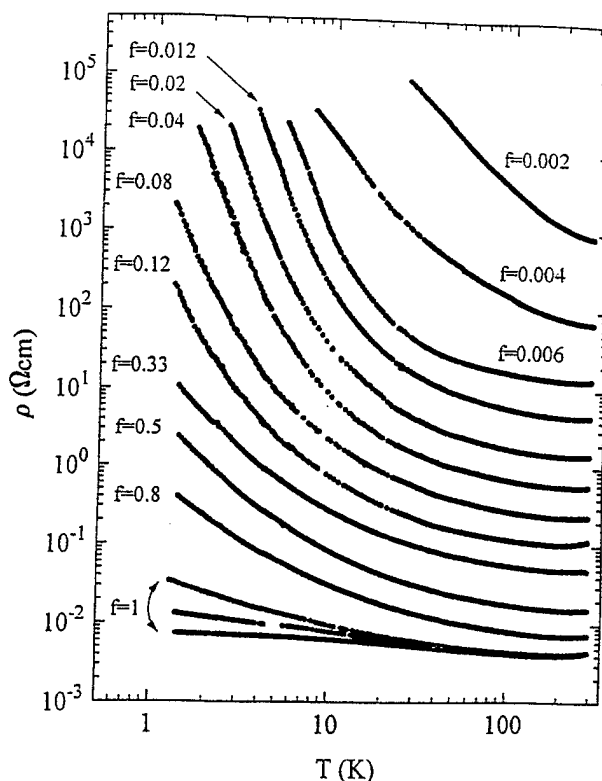


Fig. 2.56 Log₁₀-log₁₀ plot of $\rho(T)$ vs. T of PANI-CSA/PMMA blends at various concentrations (f) of PANI-CSA ($0.002 < f < 1$).

be extended below 4.2 K for $f < 0.4\%$ due to the large contact resistance (above $20 \text{ M}\Omega$) at very low temperatures.

Again, the subtle variations in the temperature dependence can be most clearly observed from W vs. T plots, as shown in Fig. 2.57. The temperature dependence of the resistivity of PANI-CSA/PMMA blends can be classified into three categories:

1. $0.01 \leq f \leq 1$: the VRH exponent x increases systematically from 0.25 to 1.
2. $0.006 \leq f \leq 0.01$: the VRH exponent $x \approx 1$.
3. $0.002 \leq f \leq 0.006$: $x \approx 1/2$.

a. Temperature Dependence of the Conductivity Above the Percolation Threshold

Pure PANI-CSA ($f = 1$) is at the boundary of the disorder-induced M-I transition; in the VRH regime near the transition, $x \approx 1/4$. Upon dilution of PANI-CSA with PMMA, x increases systematically from 0.25 to 1 until the PANI network breaks up at concentrations below the percolation threshold.

The $\ln \rho \propto T^{-x}$ dependence for samples containing volume fractions of PANI-CSA below 12% is shown in Figs. 2.58a–2.58c. The results are consistent with the conclusions drawn from the W vs. T plots. The systematic variation of T_0 and x as functions of the volume

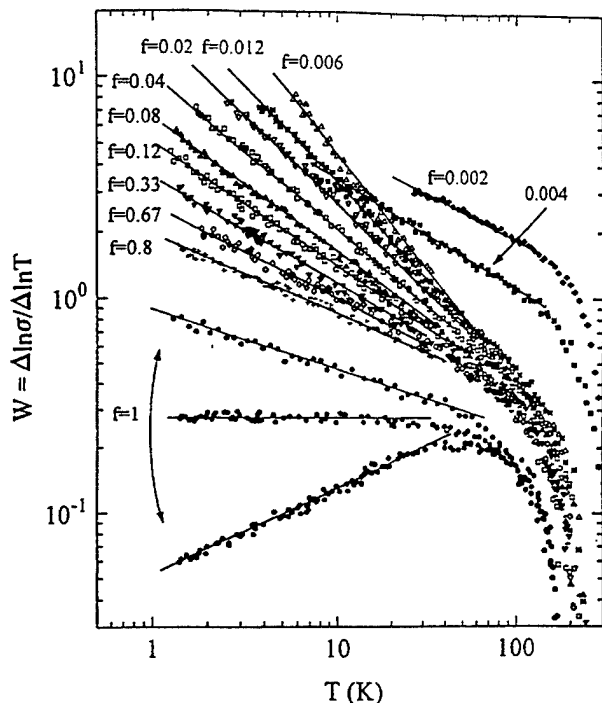


Fig. 2.57 Log₁₀-log₁₀ plot of $W = (\Delta \ln \sigma / \Delta \ln T)$ vs T for $0.002 < f < 1$. The values of T_0 and x in Eq. (15) were determined from the straight lines using Eq. (4,5).

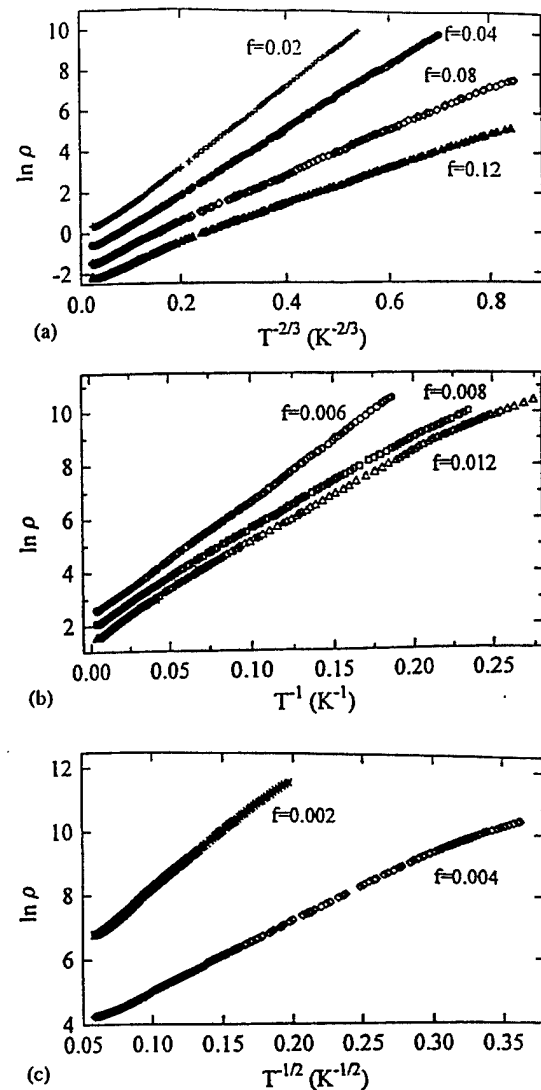


Fig. 2.58 Natural log of resistivity versus $T^{-\gamma}$ (a) $\gamma \approx 2/3$ for $f = 0.12, 0.08, 0.04$, and 0.02 ; (b) $\gamma \approx 1$ for $f = 0.012, 0.008$, and 0.006 ; (c) $\gamma = 1/2$ for $f = 0.004$ and 0.002 .

fraction of PANI-CSA is shown in Fig. 2.59. Although T_0 is practically constant and x increases systematically over the wide range of volume fractions above the percolation threshold, both T_0 and x change rather abruptly when the network becomes disconnected.

The systematic increase of x from 0.25 to 1 upon dilution of PANI-CSA ($0.012 \leq f \leq 1$) is not expected in the standard VRH model. This increase in x is observed at volume fractions of PANI-CSA well above the percolation threshold ($f_c = 0.3 \pm 0.05\%$) where the system behaves as an effective medium [175, 196, 197]. Superlocalization is expected to play a significant role only very near the percolation threshold where the connected structure is fractal. Moreover, the theoretical models of

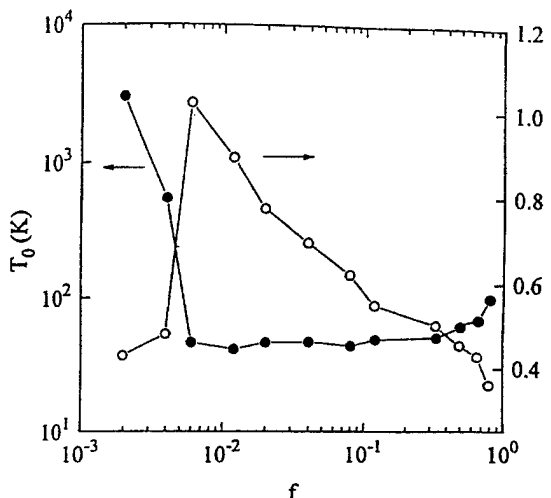


Fig. 2.59 T_0 (●) and exponent x (○) plotted as functions of the volume fraction (f) of PANI-CSA in PMMA.

superlocalization [214–217] do not predict a systematic variation of the exponent for hopping transport.

Levy and Souillard [214] have shown that in a fractal structure the wave functions for states near the Fermi level are superlocalized and decay as $\psi(r) \propto \exp[-(r/L_c)^\zeta]$, where L_c is the localization length and ζ is the superlocalization exponent, which is greater than unity (in Anderson localization $\zeta \approx 1$). Deutscher et al. [215] predicted that the temperature dependence of the electrical conductivity that results from VRH between superlocalized states would be of the form $\sigma(T) \propto \exp[-(T_0/T)^\gamma]$, where $\gamma = \zeta/(\zeta + D) \approx 3/7$. Harris and Aharony [227] predicted that γ is approximately 0.38 and 0.35 for two and three dimensions, respectively, for hopping transport in the superlocalized regime. The theory of VRH among superlocalized states was generalized by van der Putten et al. [223] to include the Coulomb interaction; van der Putten et al. obtained $\gamma \approx 0.66$ and $\zeta \approx 1.94$ consistent with the experimental results in carbon black/polymer composites. However, Aharony et al. [228,229] argued that $\zeta = 1.36$ for three dimensions and suggested that the generalized VRH equation should be used in the superlocalized regime:

$$\sigma(T) = \sigma_0 (T_0/T)^s \exp[-(T_0/T)^\gamma] \quad (29)$$

where s is the unknown exponent of the prefactor. Due to the large uncertainty [228,229] in the value of s , it is not possible to determine the values of T_0 and γ unambiguously from Eq. (29).

The fractal structure near and above the percolation threshold in PANI-CSA/PMMA blends has been demonstrated [182,183]. Aharony et al. [228,229] pointed out that the a priori requisite for applying the fractal geometry near the percolation threshold is that the length scales satisfy the condition $a \ll L_c \ll r_h \ll \xi_p$. The locali-

zation length (L_c) at 4.2 K for a 0.4% PANI-CSA sample, from the magnetic field dependence of resistivity as described below, is nearly 25 Å. The hopping length for the same 0.4% PANI-CSA sample can be estimated from the expression [175,196,197]

$$r_h(T) = (1/4) L_c (T_0/T)^{1/2} \quad (30)$$

Substituting the appropriate values for L_c and T_0 at 4.2 K gives $r_h \approx 85$ Å. The TEM micrograph for 0.5% PANI-CSA in PMMA indicates that the lower estimate for ξ_p is approximately 400 Å. The value of the smallest unit (a) is the length of the unit cell along the PANI chain direction, $a \approx 10$ Å. Hence, the criterion for applying the fractal geometry for a 0.4% PANI-CSA sample, which is near the percolation threshold, is [228,229]

$$a \ll L_c \ll r_h \ll \xi_p \rightarrow 10 \text{ \AA} < 25 \text{ \AA} < 85 \text{ \AA} < 400 \text{ \AA} \quad (31)$$

Thus, the length scales appear to satisfy the conditions presented by Aharony et al. [228,229] required for superlocalization of the electronic wave functions in a material with fractal network near the percolation threshold.

The $T^{-0.66}$ dependence of $\ln \sigma$ is valid for samples containing volume fractions $0.02 \leq f \leq 0.1$ [196,197]. Detailed studies of a wider range of samples indicate, however, that the $T^{-0.66}$ dependence of conductivity is not unique for superlocalization near the percolation threshold. The experimental results show that the exponent of the temperature dependence of conductivity in the superlocalized regime in a fractal network is sensitive to D , which in turn is determined by the morphology and the volume fraction of PANI-CSA in the system.

An alternative interpretation for the observed systematic increase in x is based on the concept of fractal character of the localized wave functions near the mobility edge [230–234]. In the standard VRH theory, the total number of states involved in the hopping conduction is assumed to be x^d times the density of states per unit volume in a region of linear dimension x , and the temperature dependence of conductivity is expressed by Eqs. (15) and (16). Aoki [230,231] and Schreiber [233] have shown that near the mobility edge the localized wave functions are fractal and that because of the fractal nature of wave functions, the number of states involved in the hopping conduction behaves like x^D where D is the fractal dimensionality (rather than x^d). The conductivity resulting from variable range hopping among such spatially fractal localized wave functions is expressed by

$$\sigma(T) \propto \exp[-(T_0/T)^{1/(D+1)}] \quad (32)$$

Since $D < d$, x would be larger than the usual values (1/4 for 3d, etc). Moreover, calculations by Schreiber and Grussbach [234] have shown that D decreases significantly with increasing disorder, yielding a further increase in the exponent of $1/T$ for increasing localization. The extent of disorder increases upon dilution of PANI-

CSA by PMMA since the localization length decreases for concentrations that approach the percolation threshold. However, the persistence of the positive temperature coefficient of resistivity near room temperature, even for samples near the percolation threshold, indicates that increased disorder does not drastically affect the metallic properties of PANI-CSA upon dilution.

Although the fractal wave function model offers a qualitative description for the systematic increase in γ for samples containing volume fractions of PANI-CSA above 1%, the $\ln \rho \propto 1/T$ dependence for samples near the percolation threshold (volume fractions of PANI-CSA between 0.6% and 1%) must result from other factors, since D is known to be greater than zero.

Activated conductivity ($\ln \rho \propto 1/T$ dependence) is usually observed when the dominant contribution to charge transport takes place by nearest-neighbor hopping [122,123]. Since the fibrillar links are the most resistive units in the network near the percolation threshold, charge transport through the links dominates when the fibrillar diameter becomes comparable to the hopping length. As shown above, the hopping length is nearly 100 Å, comparable to the diameter of the fibrillar links observed in the TEM photographs. The intrafibrillar transport in the highly resistive links dominates over the less resistive intrablob transport. As a result, the activated $1/T$ dependence for samples containing volume fractions of PANI-CSA between 1 and 0.5% is probably due to the dominant contribution from the nearest-neighbor hopping in the fibrillar links.

b. Temperature Dependence of the Conductivity Below the Percolation Threshold

The exponent $x(f)$ goes through a maximum at the percolation threshold; for samples containing volume fractions of PANI-CSA below 0.5%, the exponent decreases rapidly from 1 to 0.45 ± 0.05 as shown in Fig. 2.59. The $\ln \sigma \propto T^{-1/2}$ fits for samples containing 0.4% and 0.2% of PANI-CSA are shown in Fig. 2.58c.

The dramatic change in the transport properties near the percolation threshold, where the connectivity of the PANI-CSA network breaks up, is consistent with the TEM results. When the volume fraction of PANI-CSA decreases below 0.5%, the fibrillar diameter of the links between multiply connected regions decreases until the connected network cannot be sustained. Precisely at the point where the morphology changes, the charge transport undergoes a transition to that typical of granular metallic systems. The $\ln \sigma \propto T^{-1/2}$ dependence for samples containing volume fractions of PANI-CSA below the percolation threshold is typical of granular metals [175].

3. Magnetoresistance of the Network Near the Percolation Threshold

Theoretical work has shown that experimental studies of high field magnetotransport in a percolating medium

can provide insight into the interrelationship between microstructure and charge transport [220,221]. The magnetoresistance data, at 4.2 K, for samples containing volume fractions of PANI-CSA from 1.5 to 0.4% are shown in Fig. 2.60. The H^2 dependence of the positive MR at low fields, typical of that observed in VRH transport, is due to the shrinkage in the overlap of the wave functions of the localized states in the presence of the magnetic field [122]. The temperature dependence of the MR for samples containing 12% and 4% PANI-CSA, as typical examples of the large difference in the MR behavior at higher and lower volume fractions of PANI-CSA, is shown in Figs. 2.61a and 2.61b. Finally, the variations of MR at 4.2 and 1.4 K as a function of the volume fraction of PANI-CSA from 100% to 0.4% are shown in Fig. 2.62.

The inset of Fig. 2.60 shows the field dependence of the resistivity for a 0.4% PANI-CSA sample at 4.2 K. The localization length (L_c) for the 0.4% PANI-CSA sample can be calculated from the slope of the straight line in the inset of Fig. 2.61 (using $T_0 \sim 800$ K obtained from the temperature dependence of the resistivity). Thus, near the percolation threshold, $L_c \approx 25$ Å at 4.2

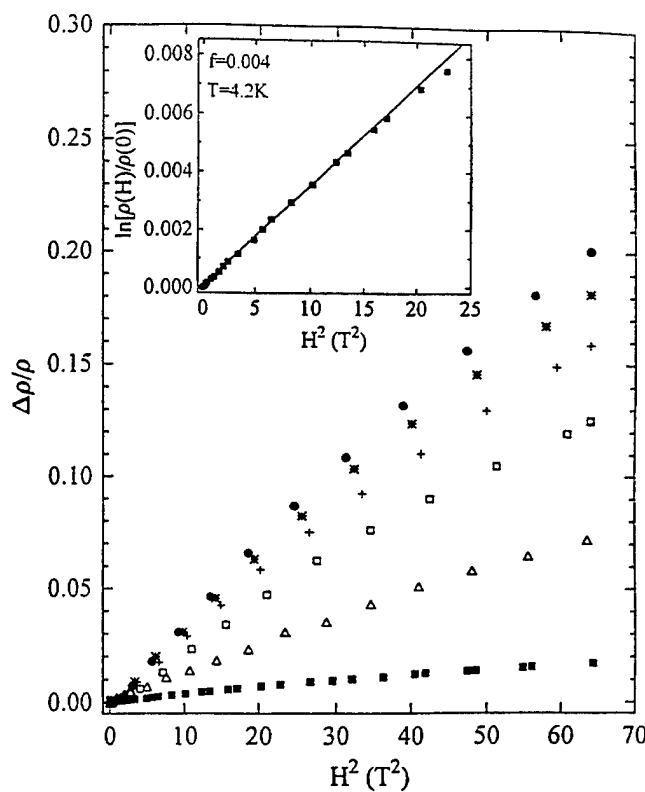


Fig. 2.60 Magnetic field dependence of conductivity for $0.015 < f < 0.004$ at $T = 4.2$ K. Magnetoresistance $[\Delta \rho/\rho(0) = \{\rho(H) - \rho(0)\}/\rho(0)]$ vs. H^2 for $f = 0.015$ (●), 0.012 (*), 0.01 (+), 0.008 (□), 0.006 (Δ), and 0.004 (■). The inset shows $\ln[\rho(H)/\rho(0)]$ vs. H^2 for $f = 0.004$ at $T = 4.2$ K. The solid line is the linear fit according to Eq. (23).

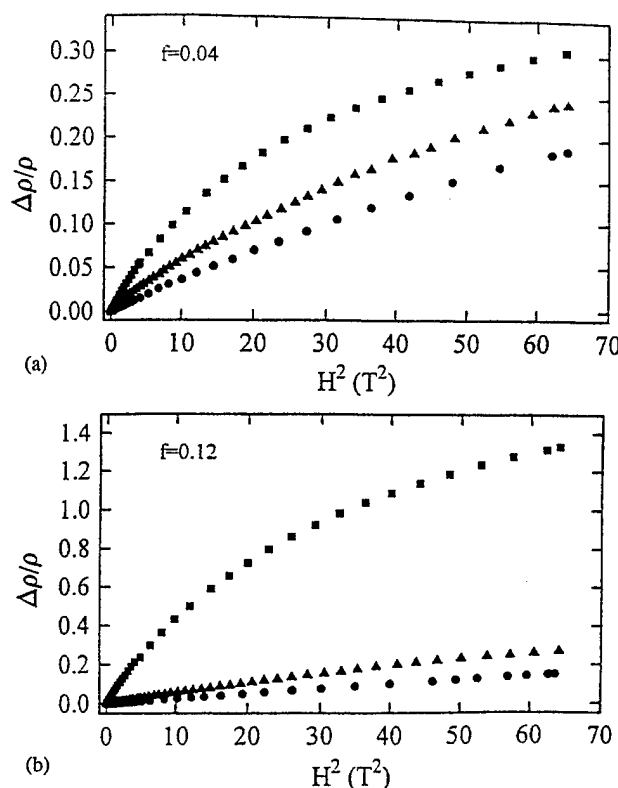


Fig. 2.61 Magnetoresistance [$\Delta\rho/\rho(0) = \{\rho(H) - \rho(0)\}/\rho(0)$] vs. H^2 at 4.2 K (●), 2.5 K (▲), and 1.4 K (■) for (a) $f = 0.04$ and (b) $f = 0.12$.

K. Since this is below the characteristic sizes seen in the TEM micrographs, the system is expected to be in the inhomogeneous limit; and it is!

The magnitude of positive MR shows a temperature-dependent maximum upon decreasing the volume fraction of PANI-CSA. Above 4.2 K the MR is rather low for both 100% PANI-CSA and blends. At 4.2 K, the MR is maximum at 1.5% PANI-CSA; at 1.4 K, the MR is maximum at 8% PANI-CSA.

A discrete model for magnetotransport in percolating systems has been proposed [220,221]. This model, which assumes that the conducting component has a closed Fermi surface and that the MR saturates at high fields, predicts a large MR in the vicinity of the percolation threshold. This is contrary to the predictions of effective medium theory in which there is no MR near the percolation threshold [235,236]. For insulating PANI-CSA (100%), the MR tends to saturate at 8 T, but it is not known whether the Fermi surface of PANI-CSA is open or closed. In order to address this question, we have carried out MR measurements in many PANI-CSA/PMMA samples (0.4–1.5 vol %) near the percolation threshold in which the volume fraction of PANI-CSA varied by 0.1% from sample to sample. At 4.2 K, the MR increases systematically upon dilution from 100% to 1.5% PANI-CSA, whereas below 1.5% the MR de-

creases rapidly as f approaches the percolation threshold. However, the MR is much higher at 1.4 K than at 4.2 K and the maximum in MR shifts to nearly 8% PANI-CSA.

The increase in MR upon dilution is consistent with the VRH model since the wave function overlap of the localized states decreases due to superlocalization of the wave functions on the fractal network upon decreasing the volume fraction of PANI-CSA. As noted earlier, when the volume fraction of PANI-CSA decreases toward f_c , the diameter of links decreases and the interblob distance increases; consequently the hopping length and the diameter of links become rather similar. At temperatures below 4.2 K, the hopping length continues to increase, and the maximum in MR shifts to higher volume fractions of PANI-CSA (larger diameter of the fibrillar links), both of which are consistent with the observations at 1.4 K. This is also consistent with the $\ln \rho \sim 1/T$ dependence for samples containing volume fractions of PANI-CSA of 1–0.5%. The rapid decrease in MR on approaching the percolation threshold is in agreement with effective medium theory [235,236]; the data do not support the discrete model [220,221].

4. Thermopower in PANI-CSA Networks

Although the temperature dependence of electrical conductivity and that of magnetoresistance in PANI-CSA/PPMA blends are sensitive to dilution, the temperature dependence of the thermopower remains linear at high temperatures as shown in Fig. 2.63 [193,196,197]. The deviation from linearity below 100 K is obvious in Fig. 2.63, and the magnitude of this deviation increases as f decreases. For the most dilute samples studied (e.g., f

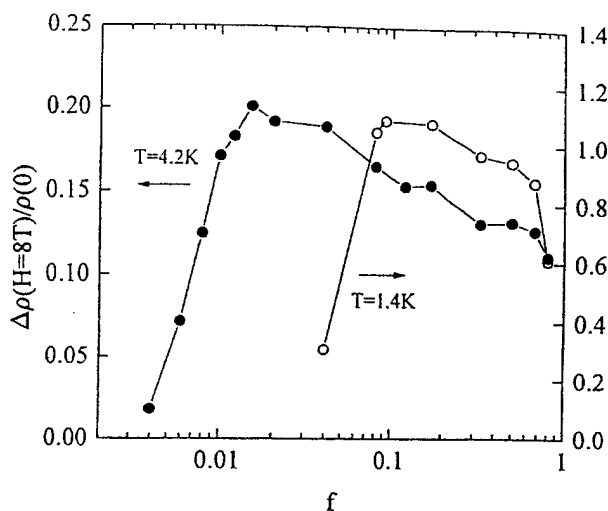


Fig. 2.62 Magnetoresistance [$\Delta\rho(H = 8\text{T})/\rho(0) = \{\rho(H = 8\text{T}) - \rho(0)\}/\rho(0)$] is plotted as a function of the volume fraction (f) of PANI-CSA in PMMA at 4.2 K and 1.4 K for $1 < f < 0.004$.

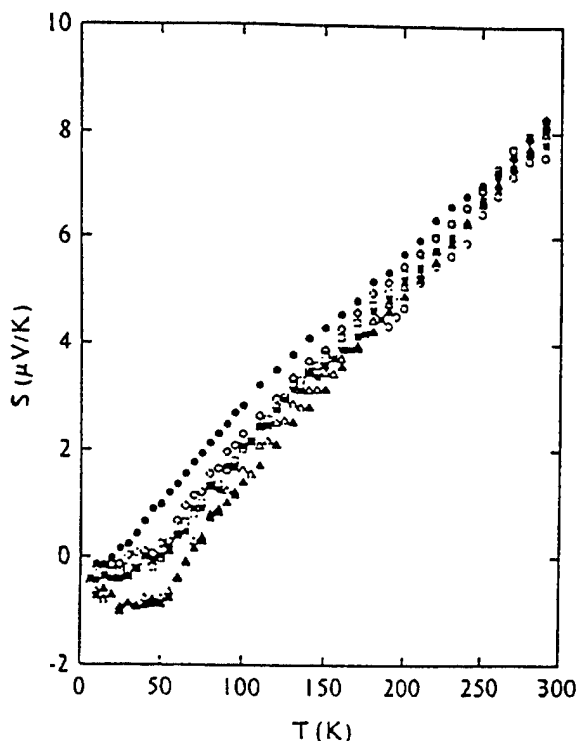


Fig. 2.63 $S(T)$ vs. T of PANI-CSA/PMMA blends at various concentrations of PANI-CSA in PMMA: $y = 100\%$ (●), 66.6% (◊), 33.3% (□), 9.09% (*), 4.76% (+), 2.43% (Δ), 1.24% (○).

= 0.024 PANI-CSA), the low temperature behavior is reminiscent of the characteristic U-shaped dependence well known for PANI-HCl [46,172]. Note, however, that the magnitude of the U-shaped deviation from linearity in Fig. 2.63 is much smaller than that reported for PANI-HCl samples (as shown in Fig. 2.52). The percolation threshold represents the contribution below which the conducting network breaks up into disconnected regions. In this sense, the observation of the weak U-shaped contribution to $S(T)$ at low volume fractions of PANI-CSA is consistent with the existence of large-scale inhomogeneity ("metallic islands") in PANI-HCl, and the U shape results from activated transport through the insulating regions.

The metallic temperature dependence of $S(T)$ observed at surprisingly low concentrations of PANI-CSA indicates that the microscopic conduction mechanism is not changed as PANI-CSA is diluted in PMMA. Although $\sigma(T)$ is strongly dependent on the mean free path and the number of connected pathways, $S(T)$ is rather insensitive to the change in the number of pathways once the connected paths are formed above the percolation threshold.

5. Summary

Transmission electron microscopic studies and conductivity measurements of PANI-CSA/PMMA blends indi-

cate that the volume fraction of PANI-CSA at the percolation threshold is approximately 0.3 wt %. The formation of a self-assembled interpenetrating network of PANI-CSA results in a low percolation threshold with rather high conductivity at threshold in comparison with other percolating systems; the conductivity near percolation threshold is 0.003 S/cm at room temperature. The positive temperature coefficient of the resistivity typical of PANI-CSA remains even at volume fractions near the percolation threshold. The value of x in the $\ln \sigma \propto T^{-x}$ dependence increases systematically, from 0.25 to 1, upon dilution. This suggests that the exponent depends on the complex morphology of the network, perhaps due to superlocalization on the fractal network near the percolation threshold. For 0.4% PANI-CSA in PMMA, the length scales [$a \ll L_c \ll r_h \ll \xi_p \rightarrow (10 \text{ \AA} < 25 \text{ \AA} < 85 \text{ \AA} < 400 \text{ \AA})$] satisfy the criteria for applying the concept of fractal geometry. For samples below 1% PANI-CSA, $x \approx 1$ until the fibrillar network breaks up at the percolation threshold. In this regime where the hopping length and the diameter of fibrillar links become similar, the $\ln \sigma \propto 1/T$ dependence is typical of nearest-neighbor hopping. In the disconnected regime below the percolation threshold, the $\ln \sigma \propto T^{-1/2}$ dependence is typical of granular metals. The positive MR increases upon decreasing the volume fraction of PANI-CSA, and when the fibrillar diameter and the hopping length become comparable the MR decreases rapidly. The small MR is in agreement with the effective medium theory but contrary to the large MR predicted near the percolation threshold by the discrete model. Although the thermopower remains linear at temperatures above 100 K upon dilution, the U-shaped feature that is observed at lower temperatures for concentrations near the percolation threshold indicates the importance of the contribution from hopping thermopower.

V. SUMMARY AND CONCLUSIONS

The developments in synthesis, doping, and processing of doped conducting polymers that have occurred in the last five years have dramatically improved the structural and electronic properties of these materials [237]. These advancements have reduced the extent of disorder and inhomogeneities in dopant distribution, and consequently the conjugation length and charge delocalization have been substantially increased. Thus the intrinsic metallic nature of doped conducting polymers, previously camouflaged by disorder, is now beginning to be revealed in transport property measurements.

Detailed transport measurements and data analyses of the present generation of doped conducting polymers have enabled precise identification and detailed investigation of the metallic, critical, and insulating regimes. Highest quality doped samples of $(\text{CH})_x$, PPy- PF_6 , PANI-CSA, and PPV show typical features of metallic systems ($k_F \lambda > 1$).

The following are highlights of the current status of the M-I transition in doped conducting polymers.

1. The disorder-induced critical regime has been observed in K-(CH)_x, I-(CH)_x, PPy-PF₆, PANI-CSA, and PPV-HSO₄. The critical regime can be precisely identified from log-log plots of W vs. T . In the critical regime, the $\sigma(T)$ follows a power law, $\sigma(T) = cT^\beta$, and $W(T)$ is temperature-independent, $W = \beta$. The power law exponent β decreases from 1 to 0.3 as ρ_r decreases, and the system moves from the insulating to the metallic regime. At high pressures, the positive temperature coefficient of $W(T)$ observed over a wide range of temperatures indicates the crossover to the metallic regime. For K-(CH)_x, PPy-PF₆, and PANI-CSA, at 8 T, the negative temperature coefficient of $W(T)$ indicates a magnetic field induced crossover from the critical regime into the insulating regime. Thus the transport can be fine-tuned from the critical regime into the metallic or insulating regimes by pressure and magnetic field, respectively.

2. Metallic properties of doped conjugated polymers are observed in the temperature dependence of conductivity, magnetoresistance, thermopower, magnetic susceptibility, and infrared reflectivity. However, the materials of this class are not yet "really metallic" with long mean free paths; they remain just on the metallic side of disorder-induced M-I transition. This implies that significantly higher electrical conductivities will be obtained with continued improvement of the materials.

The resistivity ratio (ρ_r) for high quality samples of I-(CH)_x, K-(CH)_x, FeCl₃-(CH)_x, PPy-PF₆, PANI-CSA, PPV-AsF₅, and PPV-HSO₄ is less than 2. For some samples [e.g., PANI-CSA, FeCl₃-(CH)_x], the positive TCR of real metals has been observed at temperatures above 160 K; and in the case of PPy-PF₆ and PPV-AsF₅, a positive TCR appears below 10 K.

The $T^{-3/4}$ dependence of inelastic scattering length is consistent with the $T^{3/4}$ dependence of the conductivity at low temperatures (60 K to 3 K) for I-(CH)_x, indicating that the inelastic electron-electron scattering in disordered metals is the dominant scattering mechanism. The anisotropic MC in I-(CH)_x is mainly due to the anisotropic diffusion coefficient. The positive MC [e.g., I-(CH)_x] is typical of that observed in disordered metals where the dominant contribution is from weak localization. Thus, in the metallic regime at low temperatures, both conductivity and MC are typical of systems near the M-I transition; the localization-interaction model is appropriate. The inelastic scattering lengths, at 1.2 K for I-(CH)_x, parallel and perpendicular to the chain axis are 1160 Å and 210 Å, respectively.

The $\sigma \propto T^{1/2}$ dependence observed for I-(CH)_x, PPy-PF₆, PANI-CSA, and PPV-AsF₅ indicates that the e-e interaction contribution is important at low temperatures. The linear temperature dependence of thermopower is typical of that of metals. The T^{-1} dependence of inelastic scattering time (τ_{in}) for PPy-PF₆ and PANI-CSA is in agreement with the prediction for systems very near the M-I transition. An inelastic scat-

tering time (τ_{in}) on the order of 10^{-10} s is typical of amorphous metals. The finite conductivity for metallic PANI-CSA at 75 mK is nearly 30 S/cm. The intrinsic conductivity of PANI-CSA along the chain axis is nearly 10^4 S/cm.

For PPy-PF₆, ρ_r decreases systematically upon a reduction in the disorder; the M-I transition occurs at $\rho_r \approx 10$. The correlation length from the metallic side and the localization from the insulating side increase in accordance to the predictions of scaling theory. The conductivity for unoriented PPy-PF₆ at 75 mK is nearly 100–150 S/cm. The crossover from negative to positive MC below 300 mK arises from the interplay of weak localization and e-e interaction contributions in metallic PPy-PF₆.

3. In the insulating regime, the transport properties of PPy-PF₆, iodine-doped PAT, and doped PANI samples can be divided into three categories:

- (a) Close to the critical regime on the insulating side ($\rho_r < 10^2$), the low temperature resistivity follows Mott's VRH conduction ($T^{-1/4}$) to very low temperatures ($T > 1$ K).
- (b) In the intermediate regime ($10^2 < \rho_r < 10^3$), crossover is observed from Mott to Efros-Shklovskii VRH conduction (from $T^{-1/4}$ to $T^{-1/2}$) below 10 K. The size of the Coulomb gap (Δ_C) is about 0.3–0.6 meV. The data yield $T_0/T_0' = 85–115$, $4\pi e^2 N(E_F) L_c^2 / \epsilon = 0.70–0.95$, and values of T_{cross} that are nearly identical to those estimated from $T_{cross} = 16(T_0)^2/T_0$; all are close to the approximate values estimated by Castner [78]. The resistivity at low temperature in a strong magnetic field follows the $\ln \rho \propto (T_0/T)^{1/2}$ law, where $T_0(H)/T_0(0) \propto H^p$ with $p = 1.0–1.2$, in agreement with the theory of Shklovskii.
- (c) For samples farther into the insulating regime ($\rho_r > 10^3$), $\rho(T)$ shows two distinct types of behavior. In the homogeneous limit ($L_c \geq$ structural coherence length), Mott VRH conduction is recovered at low temperature. In the inhomogeneous limit ($L_c \leq$ structural coherence length), the formation of "metallic islands" due to inhomogeneous distribution of dopants or strong morphological disorder lead to the $\ln \rho \propto (T_0/T)^{1/2}$ behavior characteristic of granular systems.

4. The thermopower in doped conducting polymers near the disorder-induced M-I transition is not as sensitive as the conductivity; $S(T)$ is nearly identical in both the metallic and insulating regimes near the M-I transition. Deep in the insulating regime, however, $S(T)$ exhibits contributions from both the diffusion thermopower (positive and $S \propto T$) and the hopping thermopower (positive or negative and $S \propto T^{1/x}$, where $x = 4$ and 2 in the homogeneous and inhomogeneous limits, respectively).

5. Transmission electron microscopic studies and

conductivity measurements of PANI-CSA/PMMA blends indicate that the volume fraction of PANI-CSA at the percolation threshold is approximately 0.3%. The conductivity near the percolation threshold is 0.003 S/cm at room temperature. The value of x in the $\ln \sigma \propto T^{-x}$ dependence of the conductivity increases systematically, from 0.25 to 1, upon dilution, indicating that x is sensitive to the morphology of the interpenetrating network, perhaps due to superlocalization of electronic wave functions on the network near the percolation threshold where the network becomes fractal. In the disconnected regime below the percolation threshold, the $\ln \sigma \propto T^{-1/2}$ dependence is typical of granular metals. The thermopower remains linear at high temperatures upon dilution. The positive MR increases upon decreasing the volume fraction of PANI-CSA. When the fibrillar diameter and the hopping length become comparable, the MR decreases rapidly.

In conclusion, doped conducting polymers are intrinsically metallic. Disorder-induced localization changes the electronic states in the partially filled band of these systems from extended and delocalized (metallic) to localized (insulating). The recent advances in the materials science of doped conducting polymers have resulted in highly conducting polymers that are processible and environmentally stable [237]. The electronic and optical properties of these systems, on either side of the M-I transition, can be varied for use in a wide range of potential applications. Based on our current understanding, further improvement of these materials is expected to yield conducting polymers with electrical conductivities comparable to or higher than those of even the best metals.

ACKNOWLEDGMENTS

We thank Dr. Yong Cao and Professor Paul Smith for their many contributions to the materials science that enabled the transport measurements at UCSB. We thank Dr. N. S. Sariciftci and Dr. Kwanghee Lee for important discussions on the properties of conducting polymers near the metal-insulator transition. Support for the transport studies at UCSB and for the preparation of this review was obtained from the MRL Program of the National Science Foundation (NSF-DMR-9123048) and from the Office of Naval Research (Dr. Kenneth Wynne), N00014-91-J-1235.

REFERENCES

1. H. Shirakawa, E. J. Louis, A. G. MacDiarmid, C. K. Chiang, and A. J. Heeger, *J. Chem. Soc. Chem. Commun.* 1977:578.
2. C. K. Chiang, C. R. Fincher, Y. W. Park, A. J. Heeger, H. Shirakawa, E. J. Louis, S. C. Gua, and A. G. MacDiarmid, *Phys. Rev. Lett.* 39:1098 (1977).
3. C. K. Chiang, M. A. Druy, S. C. Gua, A. J. Heeger, H. Shirakawa, E. J. Louis, A. G. MacDiarmid, and Y. W. Park, *J. Am. Chem. Soc.* 100:1013 (1978).
4. A. J. Heeger in *Handbook of Conducting Polymers*, Vol. 2 (T. A. Skotheim, ed.), Marcel Dekker, New York, 1986, p. 729.
5. W. P. Su, *Handbook of Conducting Polymers*, p. 757.
6. R. R. Chance, D. S. Boudreaux, J. L. Brédas, and R. Silbey, *Handbook of Conducting Polymers*, p. 825.
7. D. K. Campbell, A. R. Bishop, and M. J. Rice, *Handbook of Conducting Polymers*, p. 937.
8. S. A. Brazovskii and N. N. Kirova, *Sov. Sci. Rev. A Phys.* 5: 99 (1984) and references therein.
9. S. Roth and H. Bleier, *Adv. Phys.* 36:385 (1987) and references therein.
10. A. J. Heeger, S. Kivelson, J. R. Schrieffer, and W. P. Su, *Rev. Mod. Phys.* 60:781 (1988) and references therein.
11. Y. Lu (ed.), *Solitons and Polarons in Conducting Polymers*, World Scientific, Singapore, 1988.
12. Kiess (ed.) *Conjugated Conducting Polymers* (Springer Ser. Solid State Sci., Vol. 102), Springer New York, 1992.
13. W. R. Salaneck, I. Lundstrom, and B. Ranby (eds.), *Conjugated Polymers and Related Compounds*, Oxford Univ. Press, London, 1993.
14. H. Naarmann and N. Theophilou, *Synth. Met.* 22:1 (1987).
15. N. Basescu, Z.-N. X. Liu, D. Moses, A. J. Heeger, H. Naarmann, and Theophilou, *Nature* 327:403 (1987).
16. Th. Schimmel, D. Glaser, M. Schwoerer, and H. Naarmann in *Conjugated Polymers* (J. L. Bredas and R. Silbey, Eds.), Kluwer Academic, Dordrecht, 1991, p. 49.
17. J. Tsukamoto, *Adv. Phys.* 41:509 (1992) and references therein.
18. Bernier in *Handbook of Conducting Polymers*, Vol. 2 (T. A. Skotheim, ed.), Marcel Dekker, New York, 1986, p. 1099 and references therein.
19. A. B. Kaiser, *Phys. Rev. B* 40:2806 (1989) and references therein.
20. D. Moses, A. Denenstein, A. Pron, A. J. Heeger, and A. G. MacDiarmid, *Solid State Commun.* 36:219 (1980).
21. J. Tsukamoto, A. Takahashi, and K. Kawasaki, *Jpn. J. Appl. Phys.* 29:125 (1990).
22. I. Murase, T. Ohnishi, T. Noguchi, and M. Hirooka, *Synth. Met.* 17:639 (1984).
23. F. E. Karaz, J. D. Capistran, D. R. Gagnon, and R. W. Lenz, *Mol. Cryst. Liq. Cryst.* 118:327 (1985).
24. T. Ohnishi, T. Noguchi, T. Nakano, M. Hirooka, and I. Murase, *Synth. Met.* 41-43:309 (1991).
25. T. Hagiwara, M. Hirasaka, K. Sato, and M. Yamaura, *Synth. Met.* 36:241 (1990).
26. K. Sato, M. Yamaura, T. Hagiwara, K. Murata, and M. Tokumoto, *Synth. Met.* 40:35 (1991).

27. Y. Cao, P. Smith, and A. J. Heeger, *Synth. Met.* 48: 91 (1992).

28. Y. Cao and A. J. Heeger, *Synth. Met.* 52: 193 (1992).

29. Y. Cao, J. J. Qiu, and P. Smith, *Synth. Met.* 69:187, 191 (1995).

30. Y. Cao, P. Smith, and A. J. Heeger, in *Conjugated Polymeric Materials: Opportunities in Electronics, Optoelectronics and Molecular Electronics*, (NATO Adv. Study Inst., Ser. E: Appl. Sci. Vol. 82) (J. L. Bredas and R. R. Chance, eds.), Kluwer Academic, Dordrecht, 1990.

31. R. D. McCullough and R. D. Lowe, *J. Org. Chem.* 70:904 (1993).

32. T.-A. Chen and R. D. Rieke, *J. Am. Chem. Soc.* 114: 10087 (1992).

33. Y. W. Park, C. Park, Y. S. Lee, C. O. Yoon, H. Shirakawa, Y. Suezaki, and K. Akagi, *Solid State Commun.* 65:147 (1988).

34. M. Reghu, Y. Cao, D. Moses, and A. J. Heeger, *Phys. Rev. B* 47:1758 (1993).

35. M. Reghu, C. O. Yoon, D. Moses, A. J. Heeger, and Y. Cao, *Phys. Rev. B* 48:17685 (1993).

36. G. B. Street, in *Handbook of Conducting Polymers*, Vol. 1 (T. A. Skotheim, ed.), Marcel Dekker, New York, 1986, p. 265.

37. P. Pfluger, G. Weiser, J. Campbell Scott, and G. B. Street, in *Handbook of Conducting Polymers*, Vol. 2 (T. A. Skotheim, ed.), Marcel Dekker, 1986, p. 1369.

38. G. Tourillon, in *Handbook of Conducting Polymers*, Vol. 1 (T. A. Skotheim ed.), Marcel Dekker, New York, 1986, p. 293.

39. A. O. Patil, A. J. Heeger, and F. Wudl, *Chem. Rev.* 88:183 (1988).

40. J. Roncali, *Chem. Rev.* 92:711 (1992).

41. C. M. Gould, D. M. Bates, H. M. Bozler, A. J. Heeger, M. A. Dury, and A. G. MacDiarmid, *Phys. Rev. B* 23:6820 (1980).

42. N. F. Mott and E. A. David, *Electronic Process in Noncrystalline Materials*, Oxford Univ. Press, Oxford, 1979.

43. N. F. Mott, *Metal-Insulator Transition*, 2nd ed., Taylor & Francis, London, 1990.

44. P. A. Lee and T. V. Ramakrishnan, *Rev. Mod. Phys.* 57: 287 (1985) and references therein.

45. A. L. Efros and M. Pollak (eds.), *Electron-Electron Interactions in Disordered Systems*, North-Holland, Amsterdam, 1985.

46. S. Kivelson and A. J. Heeger, *Synth. Met.* 22:371 (1989).

47. H. Fujiwara, H. Kadomatsu, and K. Tohma, *Rev. Sci. Instrum.* 51:1345 (1980).

48. Y. W. Park, *Synth. Met.* 45:173 (1991).

49. R. B. Roberts, *Phil. Mag.* 36:91 (1977).

50. P. W. Anderson, *Phys. Rev.* 109:1492 (1958).

51. P. W. Anderson, *Comments Solid State Phys.* 2:193 (1970).

52. A. F. Ioffe and A. R. Regel, *Prog. Semicond.* 4:237 (1960).

53. E. Abrahams, P. W. Anderson, D. C. Licciardello, and T. V. Ramakrishnan, *Phys. Rev. Lett.* 42:695 (1979).

54. A. Möbius, *J. Phys. C: Solid State Phys.* 18:4639 (1985); *Phys. Rev. B* 40:4194 (1989).

55. A. J. Heeger and P. Smith, in *Conjugated Polymers* (J. L. Bredas and R. Silbey, eds.), Kluwer Academic, Dordrecht, 1991, p. 141.

56. R. H. Baughman, N. S. Murthy, and H. Eckhardt, *Phys. Rev. B* 46:10515 (1992).

57. N. S. Murthy, R. H. Baughman, and L. W. Shackette, *Phys. Rev. B* 41:3708 (1990).

58. Y. Wada, in *Physics and Chemistry of Materials with Low-Dimensional Structures* (H. Aoki, M. Tsukada, M. Schluter, and F. Levy, eds.), Kluwer Academic, Dordrecht, 1992.

59. D. Chen, M. J. Winokur, Y. Cao, A. J. Heeger, and F. E. Karasz, *Phys. Rev. B* 45:2035 (1992).

60. M. J. Winokur, J. Maron, Y. Cao, and A. J. Heeger, *Phys. Rev. B* 45:9656 (1992).

61. T. J. Prosa, M. J. Winokur, J. Moulton, P. Smith, and A. J. Heeger, *Phys. Rev. B* 51:159 (1995).

62. P. Papanek, J. E. Fisher, J. L. Sauvajol, A. J. Dianoux, G. Mao, M. J. Winokur, and F. E. Karasz, *Phys. Rev. B* 50:15668 (1994).

63. J. P. Pouget, Z. Oblakowski, Y. Nogami, P. A. Alibouy, M. Laridjani, E. J. Oh, Y. Min, A. G. MacDiarmid, J. Tsukamoto, T. Ishiguro, and A. J. Epstein, *Synth. Met.* 65:131 (1994).

64. Nogami, J. P. Pouget, and T. Ishiguro, *Synth. Met.* 62:257 (1994).

65. A. J. Epstein, J. M. Ginder, F. Zuo, H. S. Woo, D. B. Tanner, A. F. Richter, M. Angelopoulos, W. S. Huang, and A. G. MacDiarmid, *Synth. Met.* 21:63 (1987).

66. A. J. Epstein, J. Joo, R. S. Kohlman, G. Du, A. G. MacDiarmid, E. J. Oh, Y. Min, J. Tsukamoto, H. Kaneko and J. P. Pouget, *Synth. Met.* 65:149 (1994).

67. A. G. MacDiarmid and A. J. Epstein, *Synth. Met.* 65:103 (1994).

68. A. J. Epstein, J. Joo, C. Y. Wu, A. Benatar, C. F. Faisst, Jr., J. Zegarski, and A. G. MacDiarmid, in *Intrinsically Conducting Polymers: An Emerging Technology* (M. Aldissi, ed.), Kluwer, Dordrecht, 1993, p. 165 and references therein.

69. Z. Wang, A. Ray, A. G. MacDiarmid, and A. J. Epstein, *Phys. Rev. B* 43:4373 (1991).

70. Q. Li, L. Cruz, and P. Phillips, *Phys. Rev. B* 47:1840 (1993).

71. A. G. Zabrodskii and K. N. Zeninova, *Zh. Eksp. Teor. Fiz.* 86:727 (1984) [Sov. Phys. JETP 59:425 (1984)].

72. A. G. Zabrodskii, *Fiz. Tekh. Poluprovodn.* 11:595 (1977) [Sov. Phys. Semicond. 11:345 (1977)].

73. G. Thummes, U. Zimmer, F. Korner, and J. Kotzler, *Jpn. J. Appl. Phys. Suppl.* 26(3):713 (1987).

74. G. Thummes, E. Korner, and J. Kotzler, *Solid State Commun.* 67:215 (1988).

75. S. Roth, in *Hopping Transport in Solids* (M. Pollak and B. Shklovskii, eds.), North-Holland, Amsterdam, 1991, p. 377 and references therein.

76. W. L. McMillan, *Phys. Rev. B* **24**:2739 (1981).
77. A. I. Larkin and D. E. Khmelnitskii, *Zh. Eksp. Teor. Fiz.* **83**: 1140 (1982) [*Sov. Phys. JETP* **56**:647 (1982)].
78. T. G. Castner, in *Hopping Transport in Solids* (M. Pollak and B. I. Shklovskii, eds.), North-Holland, Amsterdam, 1990, p. 1 and references therein.
79. L. Pietronero, *Synth. Met.* **8**:225 (1983).
80. R. E. Peierls, *Quantum Theory of Solids*, Oxford Univ. Press, London, 1955.
81. S. Kivelson and A. J. Heeger, *Phys. Rev. Lett.* **55**: 308 (1985).
82. K. Harigaya, A. Terai, and Y. Wada, *Phys. Rev. B* **43**:4141 (1991).
83. K. Harigaya, and A. Terai, *Phys. Rev. B* **44**:7835 (1991).
84. E. M. Conwell and H. A. Mizes, *Synth. Met.* **65**:203 (1994).
85. S. Stafstrom, *Phys. Rev. B* **47**:12437 (1993).
86. P. Phillips and L. Cruz, *Synth. Met.* **65**:225 (1994).
87. E. Jeckelmann and D. Baeriswyl, *Synth. Met.* **65**:211 (1994) and references therein.
88. M. I. Salkola and S. A. Kivelson, *Phys. Rev. B* **50**: 13962 (1994).
89. Y. W. Park, C. O. Yoon, C. H. Lee, and H. Shirakawa, *Makromol. Chem. Macromol. Chem. Macromol. Symp.* **33**:341 (1990).
90. Y. W. Park, C. O. Yoon, B. C. Na, H. Shirakawa, and K. Akagi, *Synth. Met.* **41**–**43**:27 (1991).
91. Y. W. Park, C. O. Yoon, C. H. Lee, H. Shirakawa, Y. Suezaki, and K. Akagi, *Synth. Met.* **28**:D27 (1989).
92. Y. W. Park, A. J. Heeger, M. A. Dury, and A. G. MacDiarmid, *J. Chem. Phys.* **73**:946 (1980).
93. V. N. Prigodin and K. B. Efetov, *Phys. Rev. Lett.* **70**:2931 (1993).
94. V. N. Prigodin and K. B. Efetov, *Synth. Met.* **65**: 195 (1994).
95. S. Stafstrom, *Synth. Met.* **65**:185 (1994).
96. S. Stafstrom, *Synth. Met.* **69**:667 (1995).
97. S. Stafstrom, *Phys. Rev. B* **51**:4137 (1995).
98. M. Buttiker, Y. Imry, R. Landauer, and S. Pinhas, *Phys. Rev. B* **31**:6207 (1985).
99. J. M. Madsen, B. R. Johnson, X. L. Hua, R. B. Hallock, M. A. Masse, and F. E. Karasz, *Phys. Rev. B* **40**:11751 (1989).
100. P. Sheng, *Phys. Rev. B* **21**:2180.
101. P. Sheng and J. Klasfster, *Phys. Rev. B* **27**:2583 (1983).
102. J. Voit and H. Buttner, *Solid State Commun.* **67**: 1233 (1988).
103. A. B. Kaiser and S. C. Graham, *Synth. Met.* **36**:367 (1990).
104. G. Paasch, *Synth. Met.* **51**:7 (1992).
105. E. M. Conwell and H. A. Mizes, *Synth. Met.* **38**:319 (1990).
106. R. H. Baughman and L. W. Shacklette, *Phys. Rev. B* **39**:5872 (1989).
107. R. H. Baughman and L. W. Shacklette, *J. Chem. Phys.* **90**:7492 (1989).
108. B. Movaghari and S. Roth, *Synth. Met.* **63**:163 (1994).
109. J. S. Andrade, Jr., Y. Shibusa, Y. Arai, and A. F. Siqueira, *Synth. Met.* **68**:167 (1995).
110. T. Ishiguro, H. Kaneko, Y. Nogami, H. Ishimoto, H. Nishiyama, M. Yamaura, T. Hagiwara, and K. Sato, *Phys. Rev. Lett.* **62**:660 (1992).
111. A. Raghunathan, T. S. Natarajan, G. Rangarajan, S. K. Dhawan and D. C. Trivedi, *Phys. Rev. B* **47**:13189 (1993).
112. A. K. Meikap, A. Das, S. Chatterjee, H. Digar, and S. N. Bhattacharya, *Phys. Rev. B* **47**:1340 (1993).
113. P. K. Kahol, V. Pendse, N. J. Pinto, M. Traore, W. T. K. Stevenson, B. J. McCormick, and J. N. Gundersen, *Phys. Rev. B* **50**:2809 (1994).
114. B. Abele, P. Sheng, M. D. Coutts, and Y. Arie, *Adv. Phys.* **24**:407 (1975).
115. P. Phillips and H.-L. Wu, *Science* **252**:1805 (1991).
116. D. H. Dunlap, H.-L. Wu, and P. Phillips, *Phys. Rev. Lett.* **65**:88 (1990).
117. L. Zuppiroli, M. N. Bussac, S. Paschen, O. Chauvet, and L. Forro, *Phys. Rev. B* **50**:5196 (1994).
118. M. N. Bussac and L. Zuppiroli, *Phys. Rev. B* **49**: 5876 (1994); **47**:5493 (1993).
119. O. Chauvet, S. Paschen, L. Forro, L. Zuppiroli, P. Bujard, K. Kai, and W. Wernet, *Synth. Met.* **63**:115 (1994).
120. M. Reghu, K. Vakiparta, C. O. Yoon, Y. Cao, D. Moses, and A. J. Heeger, *Synth. Met.* **65**:167 (1994).
121. D. E. Khmelnitskii and A. I. Larkin, *Solid State Commun.* **39**:1069 (1981).
122. B. I. Shklovskii and A. L. Efros, *Electronic Properties of Doped Semiconductors*, Springer, Heidelberg, 1984.
123. H. Bottger and V. V. Bryksin, *Hopping Conduction in Solids*, Deerfield Beach, FL, 1985.
124. K. Vakiparta, M. Reghu, M. R. Anderson, Y. Cao, D. Moses, and A. J. Heeger, *Phys. Rev. B* **47**:9977 (1993).
125. M. Reghu, K. Vakiparta, Y. Cao, and D. Moses, *Phys. Rev. B* **49**:16162 (1994).
126. C. O. Yoon, M. Reghu, A. J. Heeger, E. B. Park, Y. W. Park, K. Akagi, and H. Shirakawa, *Synth. Met.* **69**:79 (1995).
127. Y. Nogami, H. Kaneko, H. Ito, T. Ishiguro, T. Sasaki, N. Toyota, A. Takahashi, and J. Tsukamoto, *Phys. Rev. B* **43**:11829 (1991).
128. Y. Nogami, H. Kaneko, T. Ishiguro, A. Takahashi, J. Tsukamoto, and N. Hosoi, *Solid State Commun.* **76**:583 (1990).
129. M. Reghu, C. O. Yoon, D. Moses, and A. J. Heeger, *Synth. Met.* **64**:53 (1994).
130. H. Kaneko and T. Ishiguro, *Synth. Met.* **65**:141 (1994).
131. H. Shirakawa, Y. X. Zhang, T. Okuda, K. Sakamaki, and K. Akagi, *Synth. Met.* **65**:93 (1994).
132. D. Belitz and K. I. Wysokinski, *Phys. Rev. B* **36**: 9333 (1987).
133. A. Kawabata, *Solid State Commun.* **34**:431 (1980).
134. P. Dai, Y. Zhang, and M. P. Sarachik, *Phys. Rev. B* **45**: 3984 (1992); **46**:6724 (1992).
135. M. Kaveh and N. F. Mott, *Phil. Mag. B* **55**:1 (1987).

136. R. N. Bhatt and P. A. Lee, *Solid State Commun.* **48**: 755 (1983).

137. T. F. Rosenbaum, R. M. F. Milligan, G. A. Thomas, P. A. Lee, T. V. Ramakrishnan, and R. N. Bhatt, *Phys. Rev. Lett.* **47**:1758 (1981).

138. T. F. Rosenbaum, R. F. Milligan, M. A. Paalanen, G. A. Thomas, R. N. Bhatt, and W. Lin, *Phys. Rev. B* **27**:7509 (1983).

139. K. Mizoguchi, H. Sakurai, F. Shimizu, S. Masubuchi, and K. Kume, *Synth. Met.* **68**:239 (1995).

140. K. Mizoguchi, S. Masubuchi, K. Kume, K. Akagi, and H. Shirakawa, *Phys. Rev. B* **51**:8864 (1995).

141. V. N. Prigodin and S. Roth, *Synth. Met.* **53**:237 (1993).

142. A. B. Kaiser, *Synth. Met.* **45**:183 (1991).

143. Y. Nogami, M. Yamashita, H. Kaneko, T. Ishiguro, A. Takahashi, and J. Tsukamoto, *J. Phys. Soc. Jpn.* **62**:664 (1993).

144. H. H. S. Javadi, A. Chakraborty, C. Li, N. Theophilou, D. B. Swanson, A. G. MacDiarmid, and A. J. Epstein, *Phys. Rev. B* **43**:2183 (1991).

145. P. Hernandez and M. Sanquer, *Phys. Rev. Lett.* **68**: 1402 (1992).

146. N. Foxonet, P. Bernier, and J. Voit, *J. Chim. Phys. Phys.-Chim. Biol.* **89**:977 (1992).

147. N. Coustel, P. Bernier, and J. E. Fisher, *Phys. Rev. B* **43**:3147 (1991).

148. M. R. Andersson, K. Vakiparta, M. Reghu, Y. Cao, and D. Moses, *Phys. Rev. B* **47**:9238 (1993).

149. J. Joo, Z. Oblakowski, G. Du, J. P. Pouget, E. J. Oh, J. M. Wiesinger, Y. Min, A. G. MacDiarmid, and A. J. Epstein, *Phys. Rev. B* **49**:2977 (1994).

150. J. Joo and A. J. Epstein, *Rev. Sci. Instrum.* **65**:2653 (1994).

151. J. C. Clark, G. G. Ihas, A. J. Rafanello, M. W. Meisel, M. Reghu, C. O. Yoon, Y. Cao, and A. J. Heeger, *Synth. Met.* **69**:215 (1995).

152. B. Beri, A. Fert, G. Creuzet, and A. Schul, *J. Phys. F* **16**:2099 (1986).

153. C. S. Yang, Y. Cao, P. Smith, and A. J. Heeger, *Synth. Met.* **53**:293 (1993).

154. C. S. Yang, Y. Cao, and P. Smith (to be published).

155. N. S. Sariciftci, A. J. Heeger, and Y. Cao, *Phys. Rev. B* **49**:5988 (1994).

156. A. C. Kolbert, S. Caldarelli, K. F. Thier, N. S. Sariciftci, Y. Cao, and A. J. Heeger, *Phys. Rev. B* **51**: 1541 (1995).

157. K. Lee, A. J. Heeger, and Y. Cao, *Phys. Rev. B* **48**: 14884 (1993).

158. K. Lee, A. J. Heeger, and Y. Cao, *Synth. Met.* **72**: 25 (1995).

159. K. Lee, M. Reghu, E. L. Yuh, N. S. Sariciftci, and A. J. Heeger, *Synth. Met.* **68**:287 (1995).

160. K. Lee, M. Reghu, C. O. Yoon, and A. J. Heeger, *Phys. Rev. B* **52**:4779 (1995).

161. K. Mizoguchi and K. Kume, *Solid State Commun.* **89**:971 (1994).

162. K. Mizoguchi, M. Nechtschein, J. P. Travers, and C. Menardo, *Synth. Met.* **29**:E417 (1989).

163. J. P. Travers, P. Le Guyadec, P. N. Adams, P. J. Laughlin, and A. P. Monkman, *Synth. Met.* **65**:159 (1994).

164. P. N. Adams, P. J. Laughlin, A. P. Monkman, and N. Bernhoeft, *Solid State Commun.* **91**:875 (1994).

165. D. S. Galvao, D. A. dos Santos, B. Laks, C. P. de Melo, and M. J. Caldas, *Phys. Rev. Lett.* **63**:786 (1989); **65**:527 (1990).

166. P. A. Schulz, D. S. Galvao, and M. J. Caldas, *Phys. Rev. B* **44**:6073 (1991).

167. C. O. Yoon, M. Reghu, D. Moses, and A. J. Heeger, *Phys. Rev. B* **49**:10851 (1994).

168. R. S. Kohlman, J. Joo, Y. Z. Wang, J. P. Pouget, H. Kaneko, T. Ishiguro, and A. J. Epstein, *Phys. Rev. Lett.* **74**:773 (1995).

169. D. Braun, A. Brown, E. Staring, E. W. Meijer, *Synth. Met.* **65**:85 (1994).

170. M. Ahlskog, M. Reghu, et al. *Phys. Rev. B* **53**: 15529 (1996).

171. Y. W. Park, E. B. Park, K. H. Kim, C. K. Park, and J.-I. Jin, *Synth. Met.* **41-43**:315 (1991).

172. C. O. Yoon, M. Reghu, D. Moses, A. J. Heeger, Y. Cao, T.-A. Chen, X. Wu, and R. D. Rieke, *Synth. Met.* **75**:229 (1995).

173. K. Vakiparta, M. Reghu, M. R. Andersson, J. Moulton, and T. Taka, *Solid State Commun.* **87**:619 (1993).

174. K. Ehinger and S. Roth, *Phil. Mag.* **53**:301 (1986).

175. M. Reghu, C. O. Yoon, C. Y. Yang, D. Moses, P. Smith, A. J. Heeger, and Y. Cao, *Phys. Rev. B* **50**: 13931 (1994).

176. R. Rosenbaum, *Phys. Rev. B* **44**:3599 (1991).

177. Y. Zhang, P. Dai, M. Levy, and M. P. Sarachik, *Phys. Rev. Lett.* **64**:2687 (1990).

178. A. Aharony, Y. Zhang, and M. P. Sarachik, *Phys. Rev. Lett.* **68**:3900 (1992).

179. A. N. Ionov and I. S. Shlimak, in *Hopping Transport in Solids* (M. Pollak and B. I. Shklovskii, eds.) North-Holland, Amsterdam, 1990, p. 397 and references therein.

180. M. Pollak and C. J. Adkins, *Phil. Mag. B* **65**:855 (1992).

181. E. Cuevas, M. Ortuno, and J. Ruiz, *Phys. Rev. Lett.* **71**:1871 (1993).

182. A. A. Ovchinnikov and K. A. Pronin, *Synth. Met.* **41-43**:3373 (1991).

183. A. A. Ovchinnikov and K. A. Pronin, *Sov. Phys. Solid State* **28**:1666 (1986) [*Fiz. Tverd. Tela* **28**:2964 (1986)].

184. H. Tokumoto, R. Mansfield, and M. J. Lea, *Philos. Mag. B* **46**:93 (1982).

185. B. I. Shklovskii, *Zh. Eksp. Teor. Fiz. Pis. Red.* **36**: 43 (1982) [*Sov. Phys. JETP Lett.* **36**:51 (1982)].

186. B. I. Shklovskii, *Fiz. Tekh. Polouprov.* **17**:2055 (1983) [*Sov. Phys. Semicond.* **17**:1311 (1983)].

187. I. Shlimak, M. Kaveh, M. Yosefin, M. Lea, and P. Fozooni, *Phys. Rev. Lett.* **68**:3076 (1992).

188. C. O. Yoon, Ph.D. Thesis, Seoul Natl. University, 1992.

189. D. K. C. MacDonald, *Thermoelectricity: An Introduction to the Principles*, Wiley, New York, 1962.

190. I. P. Zvyagin, in *Hopping Transport in Solids* (M. Pollak and B. I. Shklovskii, eds.), Elsevier/North-Holland, Amsterdam, 1990, p. 143.

191. M. J. Burns and P. M. Chaikin, *J. Phys. C* 18:L743 (1985).

192. E. B. Park, Y. S. Yoo, J. Y. Park, Y. W. Park, et al., *Synth. Met.* 69:61 (1995).

193. C. O. Yoon, M. Reghu, D. Moses, A. J. Heeger, and Y. Cao, *Phys. Rev. B* 48:14080 (1993).

194. S. Stafstrom, J. L. Bredas, A. J. Epstein, H. S. Woo, D. B. Tanner, W. S. Huang, and A. G. MacDiarmid, *Phys. Rev. Lett.* 59:1464 (1987).

195. D. S. Boudreaux, R. R. Chance, J. F. Wolf, L. W. Shacklette, J. L. Bredas, B. Themans, J. M. Andre, and R. Silbey, *J. Chem. Phys.* 85:4584 (1986).

196. M. Reghu, C. O. Yoon, C. Y. Yang, D. Moses, A. J. Heeger, and Y. Cao, *Macromolecules* 26:7245 (1993).

197. C. O. Yoon, M. Reghu, D. Moses, A. J. Heeger, and Y. Cao, *Synth. Met.* 63:47 (1994).

198. A. Aharony and D. Stauffer, *Introduction to Percolation Theory*, 2nd ed., Taylor & Francis, London, 1993 and references therein.

199. A. Fizazi, J. Moulton, K. Pakbaz, S. D. D. Rughoothup, P. Smith, and A. J. Heeger, *Phys. Rev. Lett.* 64:2180 (1990).

200. Y. Y. Suzuki, A. J. Heeger and P. Pincus, *Macromolecules* 23:4730 (1990).

201. A. Andreatta, A. J. Heeger, and P. Smith, *Polymer Commun.* 31:275 (1990).

202. Y. Wang and M. F. Rubner, *Macromolecules* 25: 3284 (1992).

203. M. Makhlouki, M. Morsli, A. Bonnet, A. Conan, A. Pron, and S. Lefrant, *J. App. Polym. Sci.* 44:443 (1992).

204. C. K. Subramaniam, A. B. Kaiser, P. W. Gilberd, and B. Wessling, *J. Polym. Sci. B* 31:1425 (1993).

205. R. Pelster, G. Nimtz, and B. Wessling, *Phys. Rev. B* 49:12718 (1994).

206. K. Levon, A. Margolina, and A. Z. Patashinsky, *Macromolecules* 26:4061 (1993).

207. B. Bridge and H. Tee, *Int. J. Electron.* 6:785 (1990) and references therein.

208. S. De Bondt, L. Froyen, and A. Deruyttere, *J. Mater. Sci.* 27:1983 (1992).

209. F. Carmona, *Physica A* 157:461 (1989) and references therein.

210. H. Munson-McGee, *Phys. Rev. B* 43:3331 (1991).

211. Y. Yang, E. Westerweele, C. Zhang, P. Smith, and A. J. Heeger, *J. Appl. Phys.* 77:694 (1995).

212. Y. Yang and A. J. Heeger, *Nature* 372:344 (1994).

213. A. J. Heeger, *Trends Polym. Sci.* 3:39 (1995).

214. Y. E. Levy and B. Souillard, *Europhys. Lett.* 4:233 (1987).

215. G. Deutscher, Y. E. Levy, and B. Souillard, *Europhys. Lett.* 4:577 (1987).

216. A. Aharony and A. B. Harris, *Physica A* 163:38 (1990).

217. A. Aharony and A. B. Harris, *Physica A* 205:335 (1994).

218. A. Aharony and A. B. Harris, *Physica A* 191:365 (1992).

219. H. Grussbach and M. Schreiber, *Physica A* 191:394 (1992).

220. A. K. Sarychev, D. J. Bergman, and Y. M. Strelniker, *Phys. Rev. B* 48:3145 (1993).

221. D. J. Bergman and A. K. Sarychev, *Physica A* 200: 231 (1993).

222. M. A. Michels, J. C. M. Brokken-Zijp, W. M. Groenewoud, and A. Knoester, *Physica A* 157:529 (1989).

223. D. van der Putten, J. T. Moonen, H. B. Brom, J. C. M. Brokken-Zijp, and M. A. J. Michels, *Phys. Rev. Lett.* 69: 494 (1992); 70:4161 (1993).

224. F. Gubbels, R. Jerome, P. Teyssie, E. Vanlathem, R. Deltour, A. Calderone, V. Parente, and J. L. Bredas, *Macromolecules* 27:1972 (1994).

225. A. Quivy, R. Deltour, A. G. M. Jansen, and P. Wyder, *Phys. Rev. B* 39:1026 (1989).

226. M. Mehbod, P. Wyder, R. Deltour, C. Pierre, and G. Geuskens, *Phys. Rev. B* 36:7627 (1987).

227. A. B. Harris and A. Aharony, *Europhys. Lett.* 4:1355 (1987).

228. A. Aharony, O. Entin-Wohlman, and A. B. Harris, *Physica A* 200:171 (1993).

229. A. Aharony, O. Entin-Wohlman, and A. B. Harris, *Phys. Rev. Lett.* 70:4160 (1993).

230. H. Aoki, *J. Phys. C: Solid State Phys.* 16:L205 (1983).

231. H. Aoki, *Phys. Rev. B* 33:7310 (1986).

232. C. M. Soukoulis and E. N. Economou, *Phys. Rev. Lett.* 52:565 (1984).

233. M. Schreiber, *Phys. Rev. B* 31:6146 (1985).

234. M. Schreiber and H. Grussbach, *Phil. Mag. B* 65: 707 (1992).

235. B. Ya. Balagurov, *Fiz. Tverd. Tela* 28:3012 (1986) [*Sov. Phys. Solid State* 28:1694 (1986)].

236. D. Stroud and F. P. Pan, *Phys. Rev. B* 13:1434 (1976).

237. Y. W. Park and H. Lee, (eds.), *Synth. Met.*, Vol. 69, 1995 [Proc. Int. Conf. Sci. Technol. Synthetic Metals (ICSM '94), Seoul, Korea].